DISSERTATION

ROLE OF HOMOTROPIC ASSOCIATION OF LUTEINIZING HORMONE RECEPTORS IN HORMONE MEDIATED SIGNALING

Submitted by

Shirley Ann Crenshaw

Department of Chemistry

In partial fulfillment of the requirements

For the Degree of Doctor of Philosophy

Colorado State University

Fort Collins, Colorado

Spring 2012

Doctoral Committee:

Advisor: B. George Barisas

Alan van Orden
Dawn Rickey
Nancy Levinger
Deborah Roess

ABSTRACT

ROLE OF HOMOTROPIC ASSOCIATION OF LUTEININZING HORMONE RECEPTORS IN HORMONE MEDIATED SIGNAL TRANSDUCTION

G protein-coupled receptors (GPCR) are plasma membrane receptors involved in signal transduction and are an important target for drug discovery. Luteinizing hormone receptors (LHR) are GPCRs found on the reproductive organs of both males and females and promote spermatogenesis and ovulation. Understanding how these protein receptors function on the plasma membrane will lead to better understanding of the mammalian reproduction system and other GPCR systems. Studies in the past suggested that these receptors oligomerize after hormone binding, but recent studies performed with LHRs suggest that these receptors maybe constitutively oligomerized in the endoplasmic reticulum and on the plasma membrane. However, these experiments were performed on receptors expressed by transient transfection and using bioluminescence resonance energy transfer (BRET). These methods have potential weaknesses. Transient transfections typically yield a fraction of cells with very high receptor expression and BRET measurements are strongly weighted towards those cells. Hence, this overall approach may have yielded misleading results. Fluorescence energy transfer (FRET) is a similar technique to BRET but has advantages such as allowing imaging examination of single cells. Using FRET, LHR oligomerization was evaluated on cells treated with

human chorionic gonadotropin (hCG) or deglycosylated-hCG, hormones which activate and inhibit the receptor function, respectively. FRET measurements demonstrated that, on the surfaces of transiently transfected cells, LHRs exhibit substantial intermolecular FRET which is very slightly increased by hCG treatment and very slightly reduced by exposure to DG-hCG. Closer examination of these data showed that all observed FRET depended linearly on receptor expression and approach zero at low expression levels. This suggests that FRET between LHR on these transiently-transfected cells may arise from inter-molecular proximity induced non-specifically by high receptor surface concentrations. To evaluate the receptor density on cells flow cytometry was used. Flow cytometry revealed that transiently-transfected LHRs are expressed over a broad range of surface densities, including very high expression levels. Using a mathematical model, the FRET efficiencies expected for various receptor surface densities were calculated. These calculations suggest that expression levels observed cytometrically could cause substantial amounts of FRET from molecular crowding and, particularly if the receptors are additionally concentrated in lipid rafts, most of the observed FRET signal could be attributed to non-specific concentration effects.

THIS DISSERTATION IS DEDICATED TO MY MENTORS

Mrs. Linda Henderson (high school guidance counselor)

Dr. Daniel L. Morris (Undergraduate mentor)

ACKNOWLEDGMENTS

I would like to thank Dr. Jamie Sutherland, Michelle Sanchez, Natalie Olsen, Bryce Gode, Ted Holleran, Amy Holleran, Matt Ellis, Dr. Jennifer Finefield, Dr. Darrin Good, Dr. Christopher Whitt, Dr. Nancy Levinger, Dr. Deborah Roess and Dr. Debbie Crans for support in graduate school. I also would also like to recognize all the members of my committee but foremost B. George Barisas. I also would like to acknowledge financial support from the National Science Foundation, the National Institutes of Health, the Colorado State University College of Natural Sciences and Colorado State University's WINS program.

TABLE OF CONTENTS

LIST OF TABLES

LIST OF FIGURES

Background

Biological role of the luteinizing hormone receptor

Healthy reproductive function relies on functional luteinizing hormone receptors. In females, the receptors are located on the ovary in luteal, granulosa and theca cells. On luteal cells, signaling by LHR promotes ovulation, corpus luteum (CL) formation, and maintains progesterone levels. On granulosa and theca cells, LHR promotes steroid production and follicle maturation for ovulation [1]. In males, LHR is located in the testis on Leydig cells and promotes sperm maturation and steroid production [2].

In granulosa cells of the female, LHR regulates follicular development and triggers ovulation. Luteinizing hormone (LH) is released cyclically due to rising estrogen in the blood stream. As LH levels rise, the granulosa cells develop and transform to luteal cells to form the CL [2, 3]. This rise in estrogen creates a LH surge before ovulation, promoting the rupture of the ovulatory follicle, releasing an egg. The follicle forms a structure called the CL which produces progesterone, causing the uterus lining to thicken to receive a potential fetus. The CL is Latin for yellow body because a yellow-colored tissue fills the ruptured follicular cavity [2, 3]. If pregnancy occurs, human chorionic gonadotropin (hCG) is synthesized in the placenta by syncytiotrophoblastic cells [4] and helps prolong the lifetime of the CL. If no pregnancy occurs, progesterone is no longer produced and menstruation occurs, shedding the lining of the uterus.

Structures of luteinizing hormone receptor and cognate hormones

LHR binds the two hormones hCG and LH. LHR is a seven transmembrane (TM) domain receptor (Figure 1) and is called a "G protein-coupled receptor" (GPCR) because it activates G proteins for cell signaling. There are over 1000 GPCRs [5, 6], making this the largest class of membrane receptors. GPCRs are known for having similar structures. These receptors all have seven α-helical TM domains connected by three extracellular loops and three intracellular loops. The α-helical segments are each comprised of 25-35 amino acids [7].

The LHR is a 669 amino acid single polypeptide chain [8] divided into three domains. The extracellular domain is a glycosylated N-terminal section with 340 amino acids responsible for ligand binding [9]. The transmembrane domain spans the phospholipid bilayer with each of the seven segments connected by three extracellular loops and three intracellular loops. The intracellular domain is the C-terminal cytoplasmic tail domain with 70 amino acids which aids in signal transduction of the receptor [10]. The rat LHR (rLHR) and the human LHR (hLHR) are both about 80,000 Daltons (Da) [9] with amino acid sequence homology of 88% for the extracellular domain, 92 % for the TM domain and 69% for the intracellular domain [11].

Figure 2a-b is of human chorionic gonadotropin (hCG), a 74,000 Da glycoprotein hormone consisting of an α-subunit and β-subunit, 92 and 145 amino acids, respectively, held together by noncovalent interactions [12, 13]. The wrapping of the β-subunit around

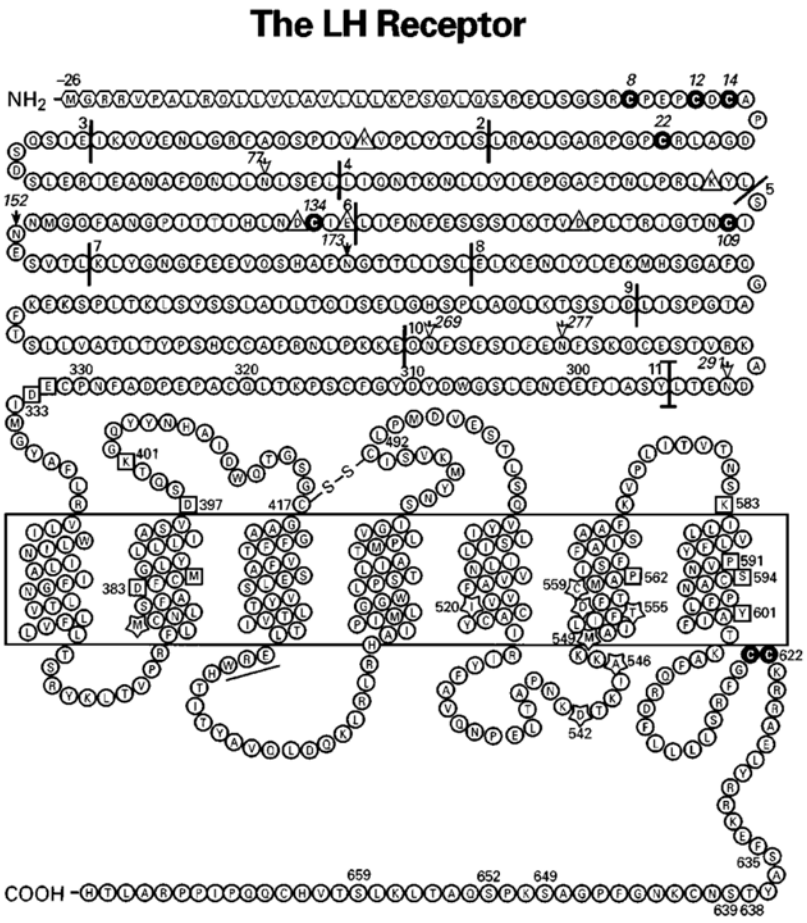

Figure 1: Amino acid sequence of LHR. LHR consists of three domains. The extracellular domain is a glycosylated N-terminal domain with responsible for ligand binding. The transmembrane domain spans across the phospholipid bilayer with each of the seven segments connected by three extracellular loops and three intracellular loops and the intracellular domain is the last domain which is a C-terminal cytoplasmic tail domain. From Dufau [2].

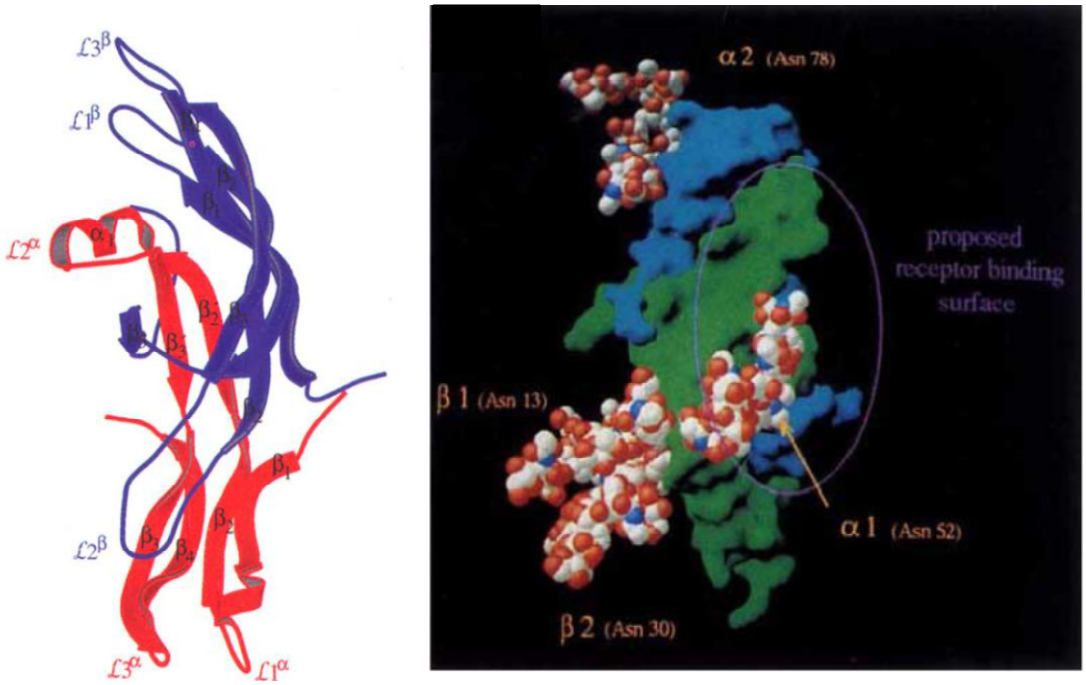

a. b.

Figure 2: Structure of hCG showing (a) the α-subunit and β-subunit held together by noncovalent interactions. The wrapping of the β-subunit around the α-subunit creates a distinctive "seat-belt" arrangement. From Hendrickson et al. [12]. (b) The hCG structure showing LHR binding sites. From Lapthorn et al. [14].

the α-subunit creates a distinctive "seat-belt" arrangement [14] which is essential for holding the subunits together. There are five disulfide bridges in the α-subunit and six in the β-subunit. While both subunits contain two N-linked carbohydrate sites, only the β-subunit contains four O-linked carbohydrate sites [12, 13]. This is the only glycoprotein hormone that contains four O-linked carbohydrate sites on the β-subunit and 30-35% of hCG's molecular weight is attributed to carbohydrates [12]. The carbohydrates are required for biological activity and also regulate the rate of hormone clearance from the body. Additionally, carbohydrates can be removed from hCG [15] to yield deglycosylated-hCG which binds LHR with the same affinity as hCG but which is non-functional because there is no activation of adenyl cyclase (AC), a protein that converts adenosine triphosphate (ATP) to cyclic adenosine monophosphate (cAMP) in the signal transduction pathway [16]. In this deglycosylated form of hCG, approximately 94% of the carbohydrates are removed by treatment of hCG with anhydrous hydrofluoric acid [15, 17].

LHR also binds LH as well as hCG. The structure of LH involves α- and β-subunits similar to hCG. The α-subunit consists of 92 amino acids, while the β-subunit consists of 121 amino acids [9]. In 1997, Roess and co-workers observed that LHRs treated with LH were rotationally mobile on MA-10 cells [18]. Conversely, hCG-treated MA-10 cells exhibited LHRs that were rotationally immobile. The results of these studies suggest that the extra carbohydrates on hCG can interact with cell proteins creating large

molecular weight complexes leading to slower rotational diffusion rates for hCG-occupied LHR relative to LH-occupied receptors.

Luteinizing hormone signal transduction

The LHR, like other G protein-coupled receptors or GPCR, activate G-proteins which are heterotrimeric proteins consisting of α, γ and β subunits, which generate cell signals in response to extracellular ligands. LHR is inactive when there is no hormone bound (Figure 3a). Hormone binding activates the receptor (Figure 3b). The G_α subunit of the G-protein undergoes an allosteric change and GDP (guanosine diphosphate), a nucleotide, is displaced with GTP (guanosine triphosphate) resulting in G_α dissociating from the G_γ and G_β subunits and binding to the receptor in which it interacts with the 3rd intracellular loop [19]. Subsequent activation of adenyl cyclase converts adenosine triphosphate to secondary messengers, cAMP, which carries signals to other systems in the cell (Figure 3c) [19]. After cAMP is released, a specific mechanism exists to stop signaling. ARF nucleotide binding site opener (ARNO) binds to the base motif of the 7th domain (Figure 3d), which promotes the displacement of GDP by GTP in ADP ribosylation factor 6 (ARF6) [19]. G_α returns to the G_γ and G_β subunits making the G-protein heterotrimeric once again. β-arrestin 2, a protein with the ability to stop signal transduction, is then released and binds to the 3rd intracellular loop for signal termination (Figure 3e) [19].

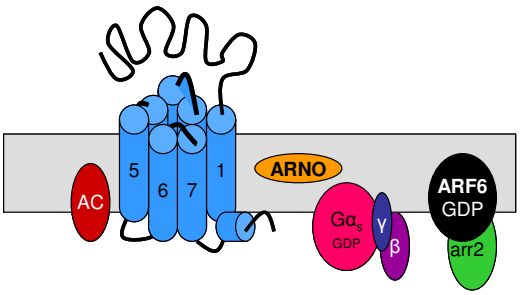

3a

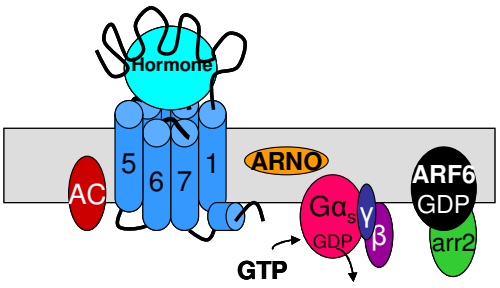

3b

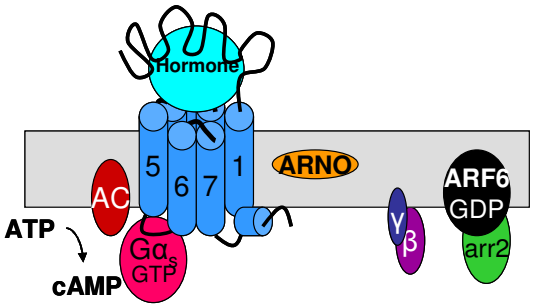

3c

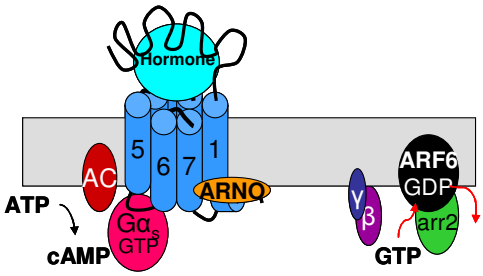

3d

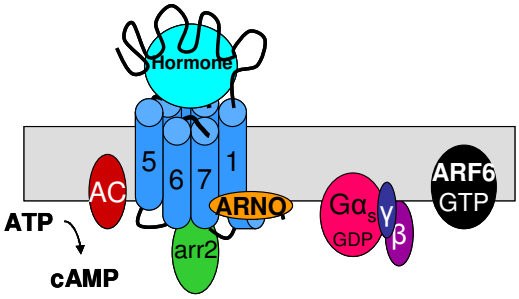

3e

Figure 3: Signal transduction pathway of LHR. (a)LHR is inactive when there is no hormone bound. (b) LHR is active when there is hormone bound to the receptor. (c) The G_α subunit of the G-protein undergoes an allosteric change and displaced with GTP and G_α dissociates from the G_γ and G_β subunits and binds to the receptor. AC is activated to convert ATP to cAMP. (d) After cAMP is released, ARF nucleotide binding site opener (ARNO) binds to the base motif of the 7th domain, which promotes the displacement of GDP by GTP in ARF6. (e) G_α returns to the G_γ and G_β subunits making the G-protein heterotrimeric one again. β-arrestin 2 is then released and binds to the 3rd intracellular loop for signal termination.

Why study the luteinizing hormone receptor?

There are several reasons to study the luteinizing hormone receptor. One of these is the importance of the receptor to mammalian fertility. Signal transduction of LHR in both sexes is important for successful reproduction. LHR has natural-occurring mutations that result in human diseases. Therefore, a better understanding of the receptor will help in understanding such conditions. One example of such a disease is familial male-limited precocious puberty (FMPP), which is early puberty in males caused by high levels of testosterone. This occurs due to constitutive activity of mutant LHR in the absence of hormone, causing testicular tumors arising from prolonged exposure to elevated testosterone levels [20]. Other examples of LHR-related diseases occur in women where infertility, polycystic ovaries and ovarian tumors can result from hyperandrogenism, namely high steroid production attributed to excess LH production [20]. Recently, it was also found that increased levels of LH are associated with cognition impairment and higher risk of Alzheimer's disease [21].

Additionally, the study of LHR is important because G protein-coupled receptors (GPCR) represent 50% of targets for new drug development [22, 23]. Thus better understanding of GPCRs can lead to new and improved drug therapeutics. Relatively little is known about GPCR interactions with protein ligands. Computerized modeling approaches are often used in drug design by pharmaceutical companies to determine receptor ligands and biological function [22, 24] due to limited experimental information on how GPCR interact with ligands on actual cells. Thus, increasing our understanding of

the GPCR transduction pathway in actual cells will result in a better understanding of structural features that activate receptors and thus lead to more selective receptor targeting in drug development. Furthermore, this will lead to new therapeutics including those with reduced non-specific drug effects. Examples of GPCRs targeted in the pharmaceutical industry are Zyprexa, Claritin and Serevent [24]. Zyprexa targets the serotonin 5-HT_2 receptor to treat schizophrenia or psychosis. Claritin targets the histamine H_1 receptor and treats rhinitis or allergies and Serevent targets the β_2-adrenergic receptor and treats asthma.

Models for the plasma membrane

LHR is a transmembrane protein, therefore it is important to understand the nature of the plasma membrane in which it is imbedded. In 1925, lipid arrangement in cell membranes was proposed by Gorter and Grendel [25]. In a Langmuir trough at the air/water interface, molecular surface areas in monomolecular layers of lipids extracted from red blood cells were compared to surface areas of individual red blood cells. From their data, they proposed the lipid layer was two lipids thick. Danielli and Davson [25] extended this model by adding adsorbed proteins to the external and internal hydrophilic surfaces of the membrane layer (Figure 4).

In 1972, Singer and Nicolson [26] proposed the Fluid Mosaic Model to describe the organization of the plasma membrane. This model suggests that the plasma membrane is a two-dimensional bilayer of phospholipids with integral and peripheral

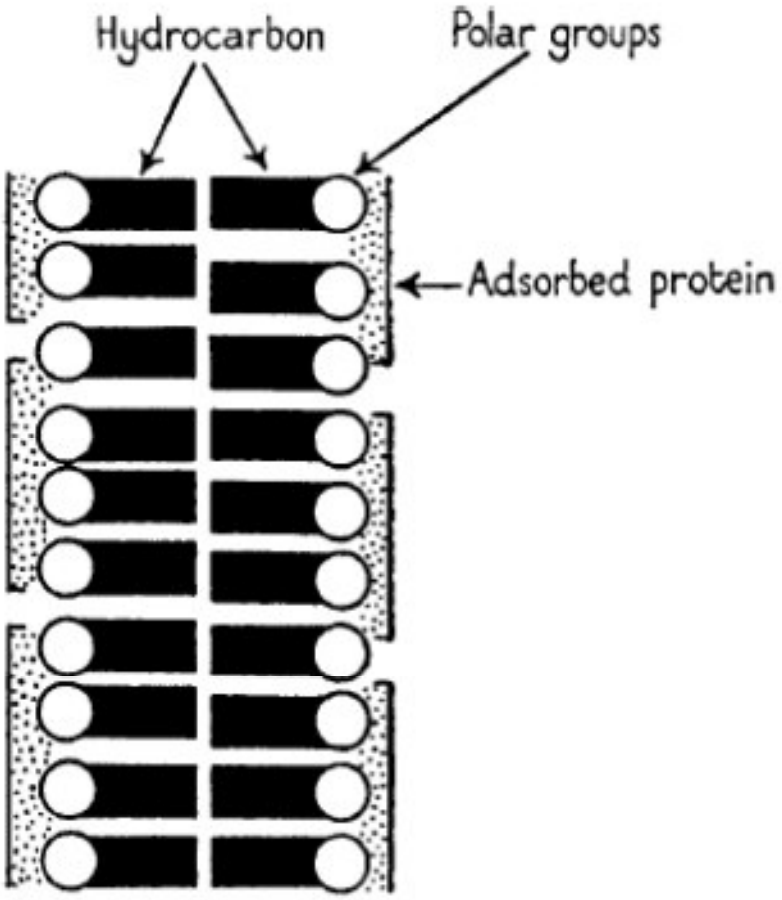

Figure 4: Diagram of the lipid layer proposed two lipids thick by Gorter and Grendel. Danielli and Davson extended this model by adding adsorbed proteins to the external and internal hydrophilic surfaces of the membrane layer [25]. From Weiss [25].

proteins within and sitting atop, respectively, the plasma membrane (Figure 5). The fluid mosaic model was distinct from the dynamic model proposed by Danielli and Davson in 1934. In the fluid mosaic model, the phospholipids have polar heads consisting of ionic residues that react with water. The phospholipids' non-polar hydrocarbon chains face the inside of the phospholipid bilayer to interact with each other. The hydrophilic and hydrophobic interactions of the phospholipids in an aqueous environment lead to the organization of plasma membrane phospholipids in a thermodynamically-stable structure. Electrostatic interactions and hydrogen bonding are secondary in the phospholipid bilayer organization. Proteins in the phospholipid bilayer are oriented so that their charged and polar residues interact with the aqueous environment and the hydrophobic surfaces of their amino acid residues interact with the hydrocarbon chains for the phospholipids.

In 2005, Kusumi and co-workers [27] added that the cytoskeleton, a structure that maintains the integrity of the cell membrane, plays a role in regulating lateral diffusion of plasma membrane proteins. They observed that lipid and protein diffusion in cell membrane is compartmentalized with sub-micron compartment sizes of 32-230 nm and that diffusion within a compartment was much faster than diffusion over longer distances, i.e. between compartments. The slower diffusion rates were attributed to plasma membrane proteins and lipids hopping over the barriers to move to another compartment. They termed this "hop diffusion" (Figure 6) and introduced the Compartmentalized Fluid Model for the organization of the plasma membrane.

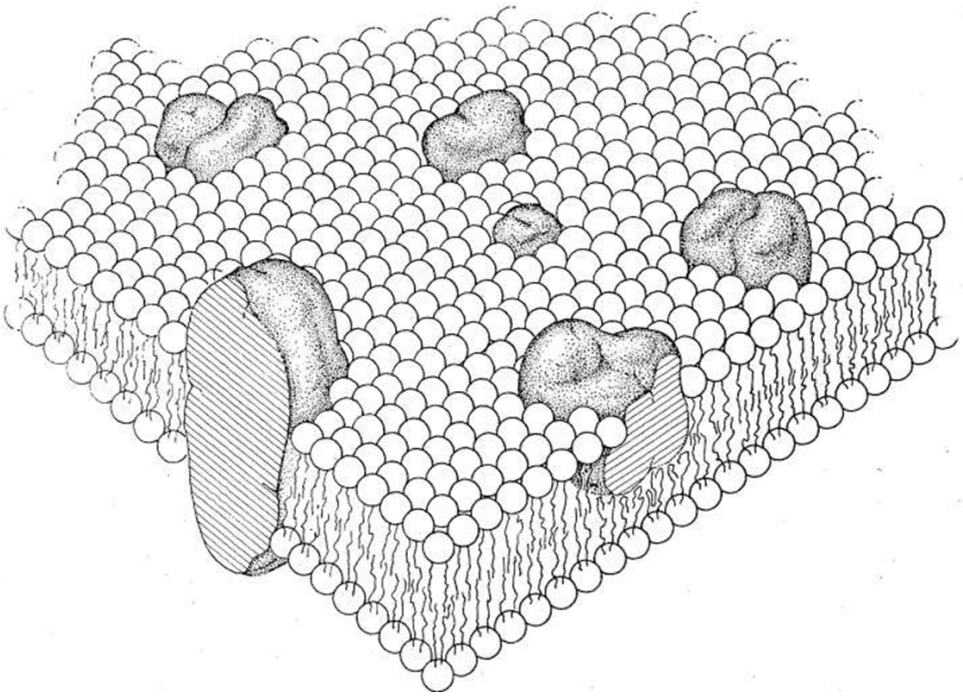

Figure 5: Singer and Nicolson's fluid mosaic model. This model explains that the plasma membrane is a two-dimensional phospholipid bilayer with integral and peripheral proteins within and atop, respectively, the plasma membrane. From Weiss [25].

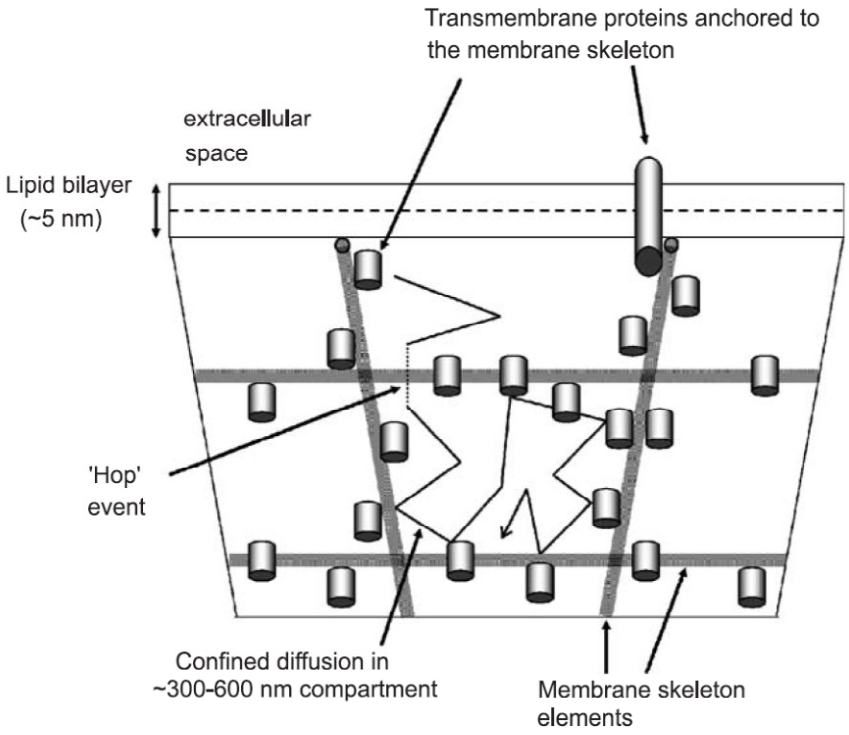

Figure 6: Diagram of Compartmentalized Fluid Model proposed by Kusumi and co-workers [28]. In this model, the cytoskeleton, a structure that maintains the integrity of the cell membrane, plays a role in restricting lateral protein diffusion in the plasma membrane. They experimentally observed proteins and lipids hopping over barriers such as the cytoskeleton to move to another compartment. From Schmidt et al. [29].

Biophysical studies of membrane molecule dynamics and interactions

In the 1970s, various groups demonstrated lateral diffusion of molecules within the plasma membrane. In 1972, Singer had proposed that proteins and lipids in the plasma membrane are capable of lateral and rotational motion [26]. One of the first studies demonstrating free diffusion in the plasma membrane was that of Frye and Eddin. In 1970 Frye and Eddin [30] used fluorescein isothiocyanate [31] and tetramethylrhodamine isothiocyanate (TRITC) to label two antibodies directed against surface antigens on human and mouse lymphocytes, respectively. Human and mouse lymphocytes were fused by Sendai virus to form heterokaryons which, upon treatment with the antibodies exhibited red- and green-fluorescence. With fluorescence microscopy, mouse and humans antigens were observed as halves of the plasma membrane after cell fusion and, after approximately 40 minutes, they observed a 90% mix occurring. In 1973 Loor and co-workers [32] found that the plan lectin concanavalin A promoted aggregation of membrane proteins on lymphocytes. They saw large clusters or "caps" of fluorochrome-labeled glycoproteins after treatment with concanavalin A, a lectin which aggregates mannose- and glucose- containing glycoproteins. In addition, Poo and Cone [33] monitored absorption after photobleaching of rhodopsin in retinal rod outer segments, to observe lateral diffusion of membrane proteins. By this method Poo and Cone were able to measure diffusion of rhodopsin in retinal rod outer segments freshly removed from frogs and mudpuppy eyes with values of 3.5×10^{-9} and 3.9×10^{-9} cm^2/sec, respectively. In 1974 Peters and co-workers [34] observed lateral diffusion of 3×10^{-12}

cm^2/sec for FITC-labeled proteins on erythrocytes using an early implementation of fluorescence recovery after photobleaching (FRAP).

In 1976 fluorescence photobleaching recovery (FPR), an improved version of Peters et al.'s technique, was developed by Alexrod and co-workers [35] to measure lateral diffusion in the plasma membrane. Fluorescently-labeled molecules in a small spot, 1-10 μm in diameter are photobleached by a brief pulse of a focused laser beam, and the subsequent recovery of the fluorescence is monitored by the same, but attenuated, laser beam. Recovery occurs from lateral transport of intact fluorophores from the surrounding surface to the bleached spot. This technique also was independently developed by Jacobson and co-workers [36] after which FPR became more commonly known as FRAP.

FRAP measures both the lateral diffusion coefficient of a molecule and the fraction of that molecule that is mobile in the plasma membrane. Both the diffusion coefficient and "mobile fraction" reflect the interactions of the protein with other membrane molecules and/or structures. FRAP fluorescence recovery intensity can be plotted versus time and, from the measured recovery half-time $t_{1/2}$, diffusion coefficients can be calculated, using

$$t_{1/2} = \frac{r^2}{4D} \qquad (1)$$

where D is the diffusion coefficient and r is the laser beam $1/e^2$ radius. The mobile fraction or percent recovery % R can be calculated as

$$\%R = \frac{F_\infty - F_t}{F_o - F_t} \times 100 \qquad (2)$$

Where F_0, F_t, and F_∞ represent the pre-bleached fluorescence, the immediate post-bleach fluorescence and the fluorescence recovered at long post-bleach times.

Using photobleaching methods, Jacobson and co-workers were able to show that, in mouse fibroblast cells treated with fluorescein-succinyl concanavalin A (F-SConA), surface proteins exhibited lateral mobility values close to that predicted by theory [36]. In 1979 Barisas and co-workers [37] performed photobleaching on rabbit lymphocytes. Plasma membrane proteins of T cell and B cells were stimulated by succinyl concanavalin A (S Con A), a lectin that induces aggregation but not capping as does concanavalin A. They observed a decrease over time in the diffusion constant from 1.6×10^{-10} to 6.5×10^{-11} cm^2/sec for T cells and from 1.4×10^{-10} to 5.5×10^{-11} cm^2/sec for B cells. Diffusion constants of fluorescently-labeled lipids remained relatively unchanged at 1.9×10^{-8} cm^2/sec for T cells and 1.5×10^{-8} cm^2/sec for B cells, suggesting receptors with lowered lateral motilities do not have a significant effect on the surrounding lipid environment. Mobile fractions for cells treated with S Con A were 90% for cells labeled with 1,1'-Dioctadecyl-3,3,'3' – tetramethylindocarbocyanine iodide (DiI), a fluorescent lipid dye, and 60% for cells treated with tetramethyl rhodamine (TMR) S Con A. Barisas and co-workers [38] later demonstrated that laser bleaching and probe beams not focused on exactly the same sample location would lead to inaccurate recovery times and diffusion coefficients. From theoretical calculations, Barisas showed that beam misalignment cannot exceed 0.3 times the $1/e^2$ beam radius for diffusion coefficients to

be within ~10% accuracy. Additionally, Barisas showed that neutral density filters of different degrees of wedge can yield diffusion coefficients varying by 3-to 15-fold, therefore the same neutral density filter should be retained between experiments.

There are now newer biophysical techniques that complement FRAP in measuring lateral diffusion and more complex organization such as protein interactions in the plasma membrane with living cells. These include fluorescence correlation spectroscopy (FCS) and single particle tracking (SPT).

FCS can measure the number of fluorescent molecules in a defined sample volume to probe molecular density and diffusion. FCS uses a small focal volume of several femtoliters defined by a laser beam and pinhole to monitor intensity fluctuations in a sample over time [39]. The number of observed molecules is low enough so that each molecule contributes a substantial amount of measured signal. Fluorophores diffusing in and out of the detection area give rise to fluctuations in the emitted signal. From the measured intensity, the time autocorrelation function G(τ), which is the measure of the signal's self-similarity, can be defined as

$$G(\tau) = \frac{\langle \delta F(t)\ \delta F(t+\tau) \rangle}{\langle F(t) \rangle^2} \qquad (3)$$

where δF(t) is the measured intensity fluctuation about the mean at time t and δF(t+τ) is the fluctuation at a later time (τ) from t. From a plot of G(τ) versus correlation time τ, the number N of molecules in the illuminated area of the sample can be calculated as

$$G(\tau) = \frac{1}{N}\left[\frac{1}{1+\tau/\tau_D}\right] \quad (4)$$

where τ_D is the characteristic time for fluctuation decay.

SPT is also used to measure lateral diffusion coefficients, and domain size accessed by, particular molecules. Hence this technique also provides information to evaluate protein interactions in the plasma membrane. In SPT, 20-40 nm gold nanoparticles are attached to the protein of interest and imaged over time to track protein motions [29]. Quantum dots or organic dyes can also be used for labeling plasma membrane proteins as can fluorescent proteins such as visible fluorescent protein (VFP) constructs. Particle-labeled cells in a microscope are imaged using a CCD camera. To analyze SPT data, the positions of the particles are determined for every image in the video and mean square displacements (MSD) are calculated [40]. MSD indicates the distance a particle travels over time. The definition of MSD is given by Equation 5

$$M = \left\langle \left(x(t) - x(t+\tau)^2 + (y(t) - y(t+\tau))^2\right) \right\rangle \quad (5)$$

where τ is the lag time and x and y are particle coordinates. The brackets in Equation 5 denote averages over time. Normal diffusion is unrestricted diffusion of the particle within the plasma membrane. Anomalous subdiffusion considers effects of components in the plasma membrane that interact with the labeled protein to alter the normal linear dependence of MSD on time. Confined diffusion could involve immobile proteins, proteins with restricted motion from lipid rafts, proteins confined within boundaries imposed by the cytoskeleton or proteins tethered to other immobile species. Feder and co-workers [41] derived theoretical equations for particles moving in different motions in

three dimensions. Equation 6 is for normal diffusion, Equation 7 is for anomalous subdiffusion, and Equation 8 for directed motion with diffusion in three dimensions [40].

$$M(\tau) = 6D\tau \tag{6}$$

$$M(\tau) = 6D\tau^{\alpha} \tag{7}$$

$$M(\tau) = 6D + (\upsilon\tau)^2 \tag{8}$$

where υ is velocity of the particle and D is the diffusion coefficient, τ is lag time, and α is a coefficient less than one. Equation 5, mentioned above, is for a 2-dimensional system such as lateral diffusion of a cells surface protein. SPT experiments also yield the diffusion coefficients [42] as defined by Equation 9.

$$D = \frac{L_r^{\,2}}{4\tau} \tag{9}$$

where L_r is compartment diameter and τ is particle residence time in the compartment. Figure 7 shows four theoretical curves for various modes of particle motion. Curve I is for a protein in active transport corresponding to Equation 5, curve II is for random diffusion and corresponds to Equation 6, curve III is for anomalous subdiffusion corresponding Equation 7 and curve VI is for a confined protein corresponding to Equation 8.

Over the last decade, techniques have been developed to directly image fluorescently-labeled proteins in the plasma membrane with resolution sufficient to determine protein positions on the scale of molecular dimensions. On example of such a technique is stimulated emission depletion microscopy (STED) which provides super-resolution images beyond the Abbe resolution limit normally applicable to optical

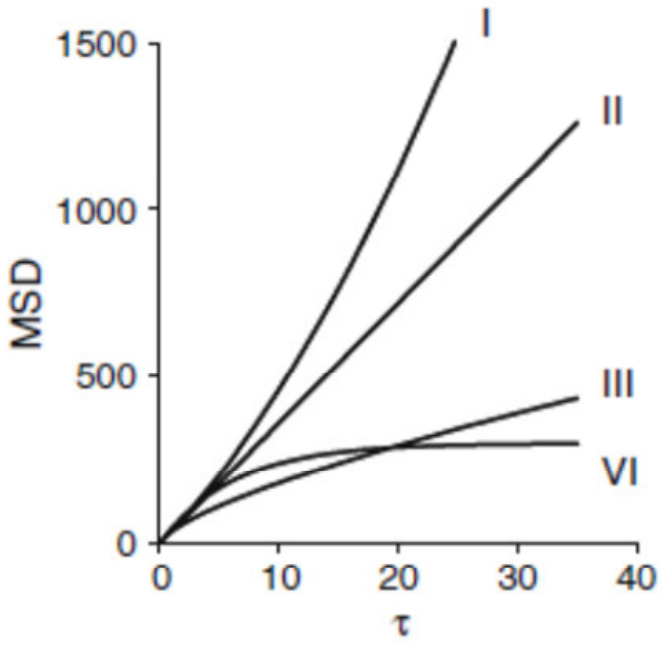

Figure 7: Mean square displacement versus time curves. (I) protein active transport (II) random diffusion (II) Anomalous subdiffusion that considers components in the plasma membrane that may interact with the labeled protein (IV) confined protein. From Gratton et al. [43].

microscopes. STED uses a doughnut-shaped depletion beam combined with a Gaussian probe beam to deplete florescence emission from the outside ring leaving only the central fluorescence emission [44] which can be smaller than the Abbe-limit; the spot size that is observed for imaging ranges from 30 to 80 nm [44, 45]. Localization microscopy such as photoactivated localization microscopy (PALM) and stochastic optical reconstruction microscopy (STORM) obtain images with approximately 10 nm localization by using intermittent fluorescence from which a super-resolution image can be reconstructed [44]. Unfortunately, these techniques require expensive equipment, long experiments and complex post-processing.

Molecular crowding

A high concentration of proteins in a given area is termed molecular crowding or the excluded volume effect because the effective protein concentration is much larger than the bulk concentration in that area. Molecular crowding is important because it has kinetic and thermodynamic effects on cell membrane molecule behavior. Minton and Ross proposed that, in surfaces that are uncrowded, the equilibrium constants and reaction rates for surface molecules can differ by orders of magnitude from cells with crowded conditions [46, 47]. However, molecular crowding is often overlooked and little attention has previously been paid to consequences of varying surface densities of membrane receptors [48, 49]. Molecular crowding is significant since some membrane proteins normally function at low concentrations but when these proteins are artificially expressed in cells, at high concentrations, molecular crowding can change the proteins'

signaling characteristics. Therefore, protein studies concerning oligomerization or aggregation should report protein surfaces densities so that possible consequences of molecular crowding can be assessed.

Molecular crowding has substantial effects on reaction equilibria. Ross and co-workers [50] reported the activity coefficient of hemoglobin as a function of hemoglobin concentration (Figure 8a). They demonstrated that the apparent concentration is higher than its actual concentration and that the relationship between the activity coefficient and hemoglobin concentration is non-linear. This is based on previous calculations that macromolecules in the cell occupy 20-30% (200-300 g L^{-1}) of the total volume [51-55]. Zimmerman [55] reports activity coefficient versus molecular weight for the macromolecule chicken egg lysozyme in *Escherichia coli* (*E. coli*) cells (Figure 8b). As molecular weight increases, the activity coefficient triples as molecular weight approaches 3000 g/mol and increases over two orders of magnitude when molecular weight approaches 50,000 g/mol, thus demonstrating the effect of molecular crowding on thermodynamic activity.

The significance of molecular crowding is that it promotes self-association of proteins by reducing the available cell volume or surface area. This can increase association constants by two or three orders of magnitude [49]. Increasing the number or size of proteins in a cell lowers the entropy of each protein, thus resulting in an increased contribution to total free energy of the surrounding environment [49]. Aggregation is favored because there is a limited amount of unoccupied volume in the cell and self-

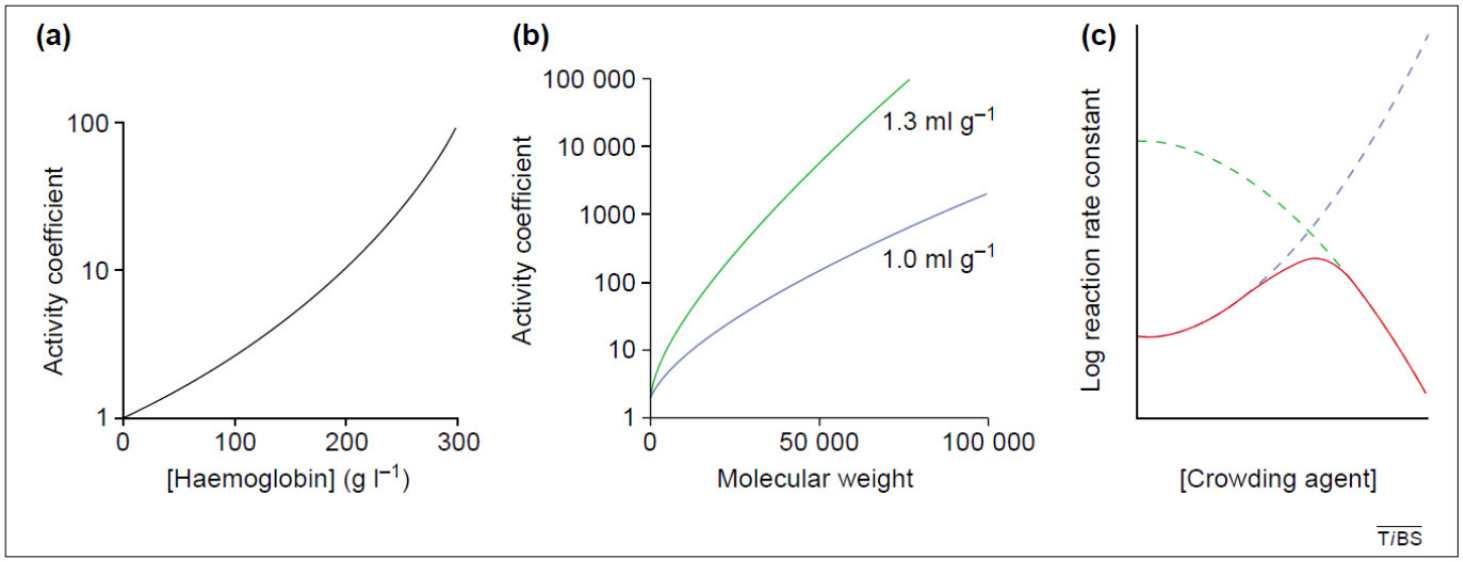

Figure 8: Effects of molecular crowding of thermodynamic and kinetic parameters. (a) This curve demonstrates activity coefficient versus hemoglobin concentration is non-linear and its apparent concentration is higher than its actual concentration. (b) The activity coefficient triples as molecular weight approaches 3000 g/mole and increases over two orders of magnitude when molecular weight approaches 50,000 g/mole, thus demonstrating the effect of molecular crowding on thermodynamic activity. (c) For a reaction, A +B ↔ AB* ↔ AB (where AB* is the transition state) the reaction is diffusion-limited (green curve) or transition state limited (blue curve), so that the overall reaction is limited by molecular crowding (red curve). From Ellis [49].

association occurs because low free volume causes an increase in effective concentration which drives aggregation. After aggregation, there may be a slight increase in available volume which lowers total free energy of the surrounding environment.

Additionally, reaction rates are affected by molecular crowding. A biological system becomes diffusion-limited at very high surface densities because there are more proteins blocking the protein's path from one point to another. Zimmerman and Minton [55] graph a theoretical curve (Figure 8c) showing the log of reaction rate versus crowding agent or fractional volume occupancy. The graph shows that, for a reaction, A +B $\leftrightarrow$ AB* $\leftrightarrow$ AB (where AB* is the transition state), the reaction is diffusion-limited (green curve) or transition state limited (blue curve) and the overall reaction is limited by molecular crowding (red curve).

The relevance of molecular crowding to actual biological phenomena varies widely among cell systems. Some endogenous membrane proteins, such as the Type I Fcε receptor appear naturally at very high surface densities [56]. Others, such as peptide hormone receptors including LHR, are typically expressed at relatively low levels [57] so that molecular crowding would thus be expected to have limited significance to their normal biological function. However, difficulties can arise when such normally sparsely-expressed receptors are artificially expressed in cells by transfection. This process begins by transient transfection which produces a cell population which typically contains a very wide range of protein expression levels.

Cell transfections can be used to study a protein of interest on cells that are easier to maintain than on cells where it is naturally expressed. Alternatively, transfection can be used to provide cells expressing a genetically modified protein or to provide a fluorescent, form of a protein that cannot be labeled via fluorophore conjugation. This can provide intrinsically fluorescent proteins. Transient transfection is a rapid technique that only takes 1-2 days for optimal expression, depending on the DNA and the cell type. However, this type of transfection may lead to high and varying expression levels since the cells take up varying amounts of DNA and so express various receptor numbers.

Stable transfections follow from transiently transfected cell samples. The transfected DNA is integrated into the chromosome and thereby stably expressed from generation to generation. After DNA is cultured with cells for 24-48 hours with a transfecting agent in a petri dish, the cells are moved to a culturing flask. Cells are cultured with the only disturbance being when a fresh change of media as needed. The media contains geneticin which is an antibiotic that allows only cells that have taken up particular DNA to live. A typical geneticin concentration amount in media for CHO cells is 400 μg/mL. The initial stable cell line selection can take anywhere from one to two weeks at which time, after a massive cell death, only successfully-transfected cells remain.

A transfected cell colony can be selected from the culture flask with a micropipette, and plated into a 24-well petri dish. After the cells in the wells reach approximately 90% confluency, which may take up to 10 days, a (hopefully) monoclonal

sample from a well is transferred to a 6-well petri dish and recloned. Alternatively, a cell line can be started from one cell in a 96-well petri dish. A hemocytometer or flow cytometry can be used to achieve a suitable dilutions giving one cell per well. To use a hemocytometer, the number of cells in a microscopic volume square of known dimensions, such as 10^6 μm^3, is counted to obtain the number of cells per mL. The appropriate volume is then calculated for one cell per well and added to a 96-well petri dish. When 90% confluency is reached in the 6-well dish, the cells are transferred to a new culture flask to grow. The 6-well petri dish culturing can take up to 14 days to for 90% confluency. The more common technique is to use flow cytometry, a technique measuring fluorescence intensity exhibited by individual cells in a population, to electrostatically sort cells in a petri dish and to determine receptor density in the cell population.

In any case, often it is the most highly expressing cells which are examined directly in transiently transfected cells or which are selected for cloning into stable cell lines. Receptors in such highly-expressing cells may thus exhibit significant molecular crowding effects which would be completely irrelevant to the physiology of receptors occurring naturally on cells.

Fluorescence resonance energy transfer and bioluminescence resonance energy transfer

The aggregation states of LHR after various cell treatments and in LHR mutants have been matters of considerable interest [18, 58-67]. Fluorescence resonance energy transfer (FRET) is a biophysical phenomenon by which distances between specific molecules can be evaluated and gives rise to the most powerful current methods for identifying intermolecular interactions on intact cells. FRET can be measured through steady state or time-resolved fluorescence measurements using fluorescently labeled molecules. FRET was first observed by Perrin in 1926 [68]. Perrin observed reduced polarization of uranin in glycerol as uranin concentration was increased. Reduced polarization was due to energy transfer manifested by practically randomized orientation of the acceptor excited state. In 1948, Förster proposed long range molecular interactions between chromophores and derived equations relating spectroscopic properties of fluorophores to interchromophore distance [69]. Förster calculated that resonance energy transfer occurs when there is dipole coupling between the donor and acceptor fluorophores. FRET efficiency (E) depends on the inverse sixth power distance (r) between the donor and acceptor as

$$E = \frac{1}{\left[1 + \left(r / r_o\right)^6\right]} \tag{10}$$

In Equation 10, r_o is the distance where FRET efficiency is 50%, also called the Förster distance, and is defined as

$$r_o = \left[8.8\times10^{-23} n^{-4} Q \kappa^2 J(\lambda)\right]^{1/6} \quad (11)$$

where n is the refractive index of the medium, Q is the quantum yield of the donor in absence of the acceptor, κ is the orientation factor of the two dipoles, and J(λ) is the spectral overlap. κ depends on the orientation of the donor and acceptor dipoles (Figure 9) and is defined by

$$\kappa^2 = \left[Cos\theta_T - 3Cos\theta_A \times Cos\theta_D\right] \quad (12)$$

where θ_T is the angle between donor and acceptor transition dipole moments and θ_A and θ_D are the angles between the separation vector, r. Kappa can vary from 0 to 4 but is usually taken to be 2/3, which is an average for all the possible angles between the donor and acceptor transition dipoles. J(λ) is defined by

$$J(\lambda) = \int_0^\infty F_D(\lambda) E_A(\lambda) \lambda^4 \, d\lambda \quad (13)$$

which is the integral between the donor fluorescence intensity $F_D(\lambda)$ and the overlapping acceptor excitation spectrum $E_A(\lambda)$.

In 1951, Weber [70] examined FRET effects on fluorescence polarization. BSA and ovalbumin were conjugated with dansyl groups and fluorescence intensity was measured for each conjugate in phosphate buffer. Within experimental error the depolarization of both BSA and ovalbumin conjugates agreed with Perrin's theoretical Equation 14 for relating polarization, rotation and the excited state lifetimes of fluorophores.

$$\frac{1}{P} - \frac{1}{3} = \left(\frac{1}{P_o} - \frac{1}{3}\right)\left(1 + \frac{3\tau}{\rho}\right) \quad (14)$$

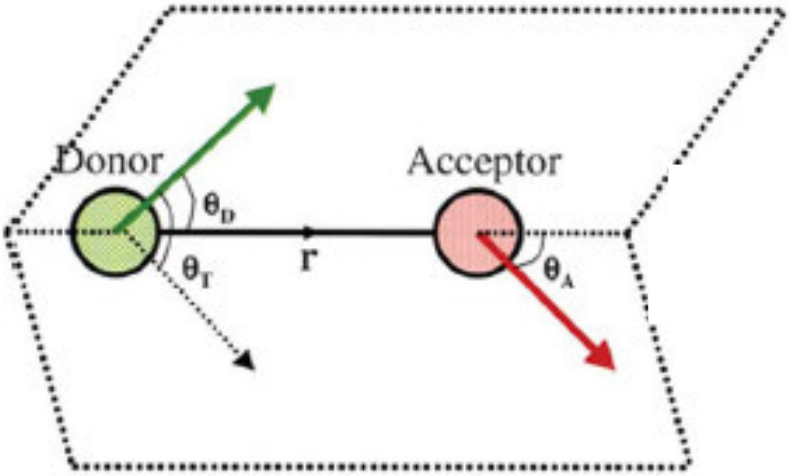

Figure 9: Dipole-dipole coupling in FRET where θ_T is the angle between donor and acceptor transition dipole moments and θ_A and θ_D are the angles between the separation vector, r and the acceptor and donor transition dipoles, respectively. Adapted from Rao and Mayor [71].

where P is observed polarization, P_o is intrinsic polarization, τ is the excited state lifetime and ρ is the Debye rotational relaxation time. In 1961, Dandliker and Feigen [70] developed the first polarization immunoassay. Fluorescein isothiocyanate [31] was conjugated to ovalbumin and antibodies that bind ovalbumin were raised to FITC-ovalbumin. Fluorescence polarization intensity was measured to detect formation of the antigen-antibody complex. Haber and Bennett [71] used fluorescence anisotropy to study FITC-insulin, FITC-ribose nucleic acid (RNA), and FITC-BSA binding to their respective antibodies in 1962. In this study, they found that, when FITC was excited with a 495 nm laser, compared to the 436 nm laser used by Dandliker and Feigen, the observed polarization was lower. This suggested that excitation wavelength could affect polarization values.

Stryer and co-workers [72] verified Förster's theory by measuring energy transfer between a naphthalene donor and a 1-dimethylanimonaphthalene-5-sulfonyl chloride (dansyl) acceptor using poly-L-proline oligomers to separate them at known distances ranging from 12-46 Å. Energy transfer efficiencies ranged from 16 to 100%, as distances between donor and acceptor molecules decreased. They observed an inverse 5.9±0.3 power dependence for FRET between donor and acceptor fluorophores which was in agreement with Förster's theory. Stryer proposed that FRET can be used as a spectroscopic ruler to determine distances between biological species [72]. In 1967, Kuhn and co-workers [73] also demonstrated there was an inverse six power dependence in FRET using by multilayers of fatty acids of known dimensions to separate cyanine dyes. In 1969, Haugland and co-workers [74] showed that the energy transfer rate depicted by

Förster reflects the overlap J between the fluorescence donor emission and acceptor absorbance. They used the rigid steroid 1'-methylindolo (3',2':2, 3)-2(5α)-androsten-17-one which has an N-methylindole donor group at one end of the molecule and a ketone group acceptor, at the other end. The distance between the donor and acceptor was 10.2 Å. Transfer rates were obtained using a nanosecond fluorimeter and excitation/emission spectra were recorded with a spectrofluorimeter as the rigid indole steroid structure was placed in solvents of varying polarity. As the solvent polarity increased, the transfer rate decreased and the donor emission shifted to the red while the acceptor emission shifted slightly to the blue. They observed that J varied by a 40-fold range as the solvent polarity increased. An advanced instrument to measure fluorescence polarization was developed by Spencer and co-workers [75] in 1973. It is described as an automated flow-cell polarization fluorometer. The flow-cell polarization fluorometer was mainly used to measure fluorescence polarization in studies of the enzyme-inhibitor or antigen-antibody interactions.

In practice, fluorescence resonance energy transfer can be measured between proteins on the surface of intact cells. The proteins of interest are labeled with fluorophores, where one is the donor and the other the acceptor. For energy transfer to occur there must be overlap between the donor emission and the acceptor excitation spectra. When an excitation source excites the donor and when both proteins are in close proximity, 1-10 nm, there is non-radiative energy transfer from donor to the acceptor. The acceptor fluorescence emission is monitored. FRET is typically performed in a fluorescence microscope, equipped with using an arc lamp or laser for an excitation. Two

types of microscopes are used namely, wide-field and confocal microscopes. The key difference is that confocal microscopy uses an aperture placed before the detectors which rejects light above and below the focal plane yielding a sharper image compared to wide-field microscopy. A confocal microscope thus images a single plane in a 3-dimensional sample.

FRET experiments using two different types of fluorophores, such as cyan (CFP) and yellow fluorescent protein (YFP), are called hetero-FRET. YFP is a highly fluorescent protein commonly fused to plasma membrane proteins. YFP is a variant of green fluorescent protein (GFP) found in jelly fish *Aequoria victoria* [76], shown in Figure 10. The overall structure of GFP involves of 11 β-strands and short segments of α-helices that form caps on the top and bottom of the cylinder structure [76]. To increase florescence intensity in experiments, enhanced green fluorescent protein (eGFP) and enhanced yellow fluorescent (eYFP) were constructed from wild type GFP and YFP, respectively. Enhanced YFP (eYFP) differs from GFP by having a threonine residue 203 (Thr203) positioned near the chromophore which causes a shift in excitation and emission spectra (Figure 11). For eGFP and eYFP, the excitation maxima are 484 nm and 514 nm, and the emission maxima are and 507 nm and 527 nm, respectively. The fluorescent form of these proteins arises when tyrosine 66 (Tyr 66) is oxygenated, causing serine 65 (Ser 65) and glycine 67 (Gly 67) to undergo rapid cyclization [76], Figure 12. The π-π* and n-π* transitions in the aromatic ring are the source of protein fluorescence. CFP can be excited at 457 nm laser source and, when YFP is in close

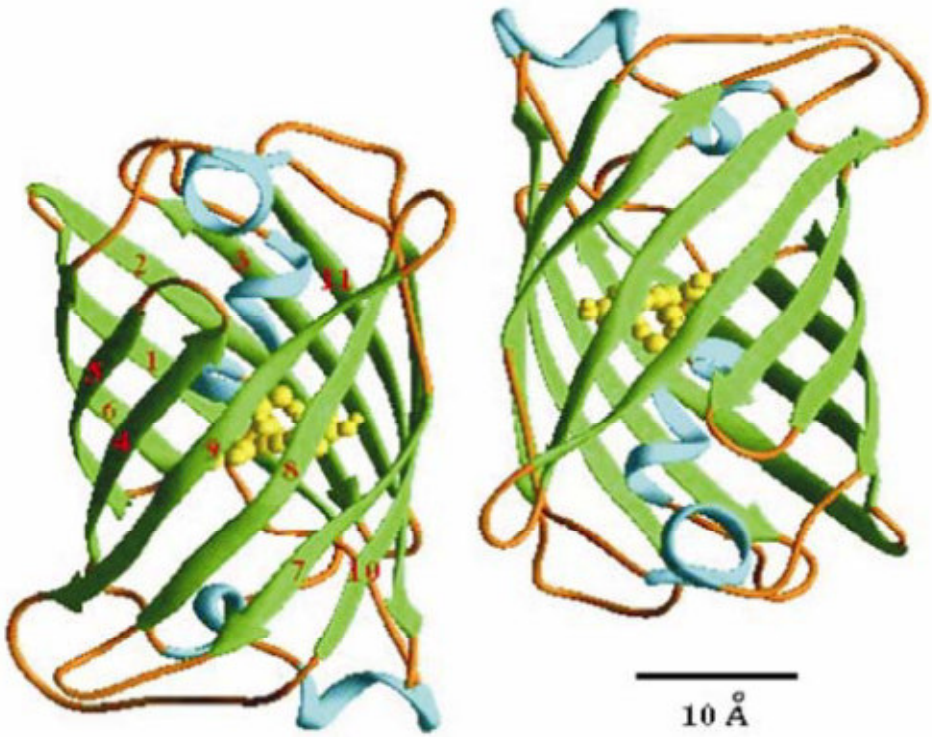

Figure 10: Two views of the GFP structure. The molecule GFP consists of 11 β-strands and short segments of α-helices that form caps on the top and bottom of the cylinder structure. From Krishna and Ingole [76].

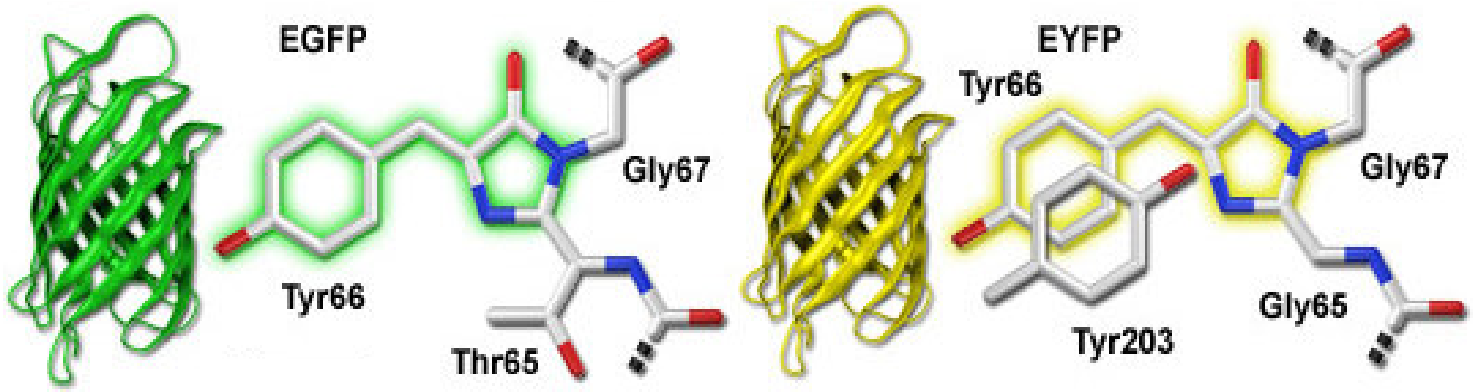

a. b.

Figure 11: Structure of eGFP and eYFP. Enhanced YFP (eYFP) differs from GFP by having a tyrosine residue at position 203 (tyr203) near the chromophore which causes a shift in excitation and emission spectra. Adapted from Olympus Microscopy Resource Center.

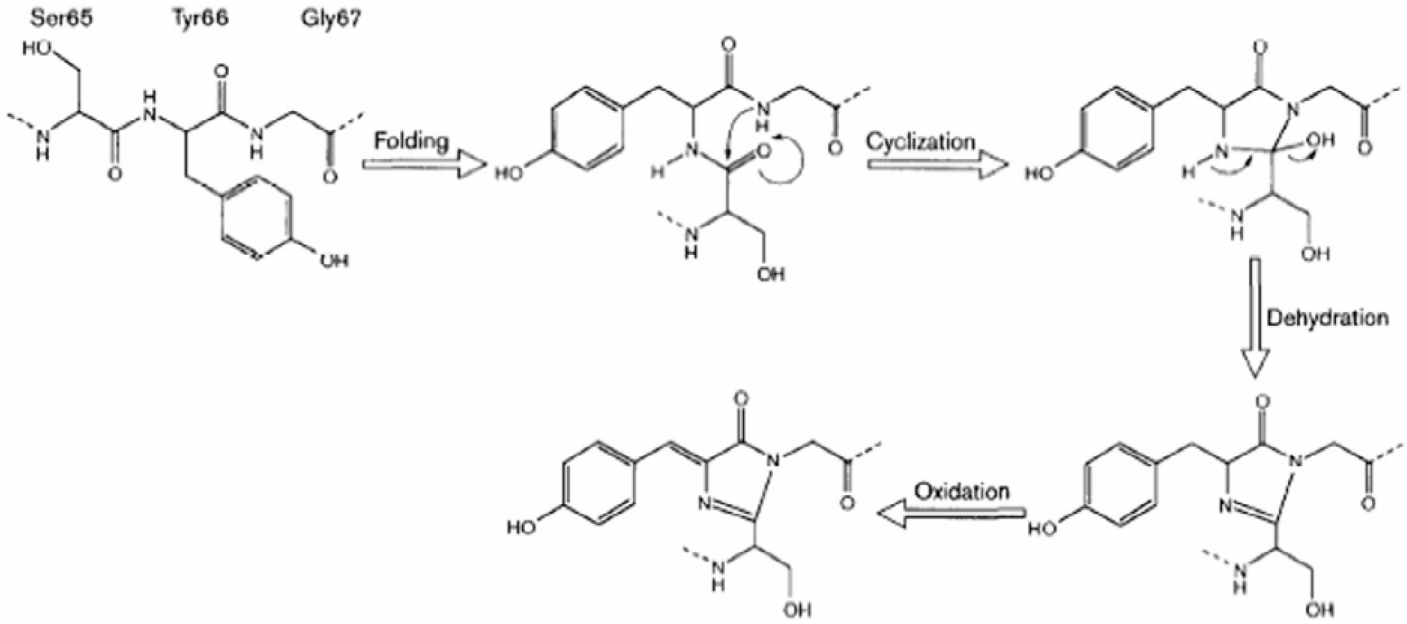

Figure 12: Fluorescent form of GFP. Fluorescence occurs when tyrosine 66 (try66) is oxygenated causing serine 65 (ser 65) and glycine 67 (gly 67) to undergo rapid cyclization. From Krishna and Ingole [76].

proximity, namely less than 10 nm [77], energy is transferred non-radiatively to YFP. YFP will then fluoresce at 527 nm (Figure 13a).

Acceptor depletion FRET is commonly used to analyze hetero-FRET data. In this method, cells with acceptor and donor fluorophores are examined before and after the acceptor fluorophores are bleached away. Donor emission is measured before and after acceptor photobleaching and percent energy transfer efficiency (E) is defined by

$$E = \left[1 - \left(\frac{F_{AD}}{F_D} \right) \right] x\ 100 \qquad (15)$$

where F_{AD} is the fluorescence emission of the donor in the presence of the acceptor and F_D is the fluorescence emission of the donor in the absence of the acceptor. Hetero-FRET can be used to observe interactions between the same or different proteins.

Another approach to evaluating FRET is through fluorescent lifetime measurements but this method requires time-correlated single photon counting methods. Percent energy transfer efficiency (E) is calculated using

$$E = \left[1 - \left(\frac{\tau_{AD}}{\tau_D} \right) \right] x\ 100 \qquad (16)$$

where τ_{AD} is the florescence lifetime of the donor in the presence of the acceptor and τ_D is the fluorescence lifetime of the donor in the absence of the acceptor. The advantage with this technique is measurements do not depend on the intensity of fluorescence and are thus independent on the extent of protein labeling. The lifetime

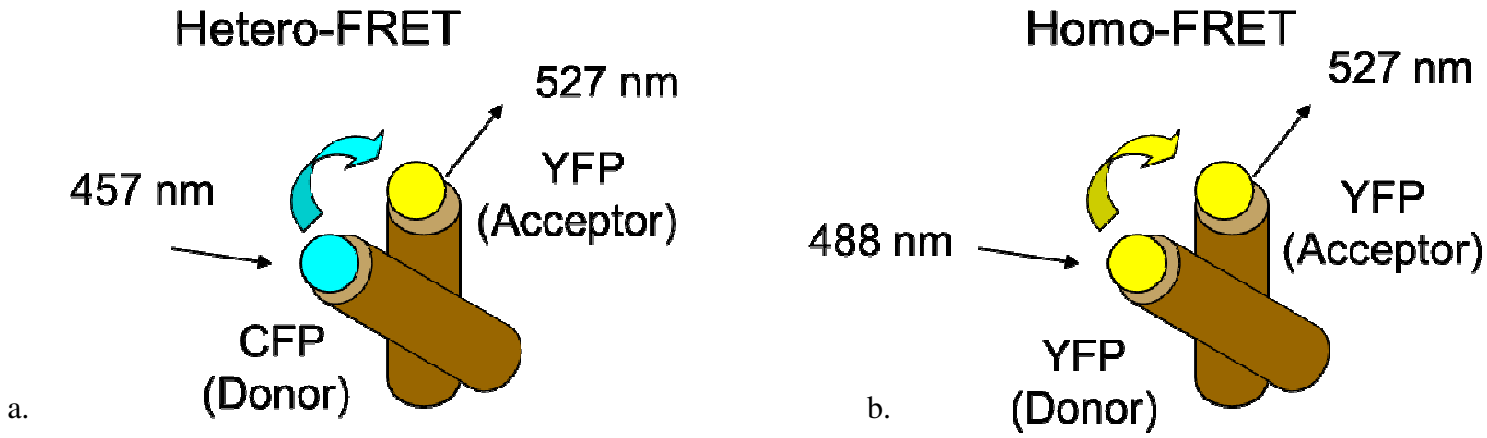

Figure 13 a-b: There are two types of FRET, hetero-FRET and homo-FRET. In hetero-FRET two different types of fluorophores are used, such as cyan (CFP) and yellow fluorescent protein (YFP). CFP can be excited at 457 nm laser source and when YFP is close, less than 10 nm, energy is transferred non-radiatively to YFP. YFP will then fluoresce at 527 nm. In homo-FRET the same fluorophore, for instance YFP, acts as both donor and acceptor. A 488 nm excitation source can be used to excite YFP. When another YFP is nearby, non-radiative energy is transferred to this YFP and this YFP will fluoresce at 527 nm.

approach can be implemented in a microscope to yield fluorescence lifetime imaging microscopy (FLIM). Both hetero-FRET and homo-FRET can be analyzed using FLIM imaging.

BRET is a variant of FRET that can be performed on intact cells or cell lysates [77]. Here, a bioluminescent enzyme donor, Renilla luciferase, is used which produces light upon chemical stimulation from a compound such as coelenterazine. The acceptor is a construct of YFP or GFP. $BRET^1$ refers to Rluc and YFP construct while $BRET^2$ refers to Rluc and a GFP construct, the superscripts in $BRET^1$ and $BRET^2$ being parts of the method name, not indications of powers. $BRET^2$ with GFP^2 is most popular due to a $BRET^2$ has separation of 115 nm from the Rluc emission peak compared to the YFP having a separation from Rluc of 55 nm. GFP^2 is a mutant of GFP that excites at 400 nm instead of 485 nm. This greater separation in Rluc and GFP^2 fluorescence emission allows easier isolation of GFP^2 fluorescence emission. BRET is commonly performed in a microplate luminometer. For experiments, saturation assays are used, where BRET signal is measured for samples where the donor is held constant and the acceptor ratio increased. BRET signal (B) is defined by Equation 17

$$B = \frac{F_A}{F_D} \tag{17}$$

where F_A is acceptor emission and F_D is donor emission. To analyze data, BRET signal is graphed as B versus acceptor/donor ratio. The amount of acceptor required at half-maximal BRET (B_{50}) for a given donor amount reflects the relative affinity of the acceptor/donor pairs. BRET cannot distinguish between dimers and oligomers. B_{50} values

are used to determine protein interactions where higher values indicate protein interaction.

Homo-FRET

Homo-FRET is the second type of FRET also termed energy migration FRET (emFRET) or polarization FRET. Three years after Förster introduced FRET, Gregorio Weber [70] examined FRET effects on polarization fluorescence leading to the technique now termed homo-FRET. Homo-FRET represents energy transfer between two identical fluorescent probes and is now used to determine the aggregation state of plasma membrane proteins. In homo-FRET, as opposed to hetero-FRET, only one fluorophore is used. This allows easier labeling; hence, it is well-suited to observing self-association of a protein. This method requires a fluorophore with small Stokes shift between absorption and emission peaks, such as that exhibited by YFP, and is based on the polarization of emitted fluorescence. If one considers fluorophores with randomly-oriented transition dipoles (Figure 14a) being excited with polarized light, photoselection occurs (Figure 14b). The probability of a fluorophore absorbing light is proportional to cosine squared of the angle θ between the direction of exciting light polarization and the absorption transition dipole [71]. These excited fluorophores transfer energy to nearby acceptor fluorophores with a probability proportional to the square of cosine of the angle γ between the donor emission transition dipole and the acceptor absorption transition dipole and FRET can be observed (Figure 14c). This re-emitted fluorescence has reduced

polarization because the emission dipoles can be differently oriented with respect to the polarization of exciting light (Figure 15).

Since only one type of fluorophore is involved and since all such molecules are equivalent, homo-FRET does not affect emission intensity. However, homo-FRET does partially depolarize acceptor emission. This depolarization is measured by anisotropy (Equation 13). Anisotropy r is calculated from emitted fluorescence intensities $I_{\parallel}$ and $I_{\perp}$, polarized parallel and perpendicular to the polarization of exciting light, respectively, as

$$r = \frac{I_{\parallel} - I_{\perp}}{I_{\parallel} + 2I_{\perp}} \tag{18}$$

Since, $I_{\parallel}$ and $I_{\perp}$ light are measured in separate channels which typically have different detection efficiencies, a correction factor called the g-factor (G) [78], which is the ratio of the sensitivities of the detection system for $\parallel$- and $\perp$- polarized fluorescence, respectively, must be applied. G is defined by Equation 19.

$$G = \frac{I_{VV}}{I_{VH}} \tag{19}$$

where I_{VV} is the fluorescence intensity observed for excitation and emission polarizers both oriented vertically with respect to the laboratory axis and I_{VH} is the intensity measured for excitation and emission polarizers vertically and horizontally oriented, respectively. Then, r becomes

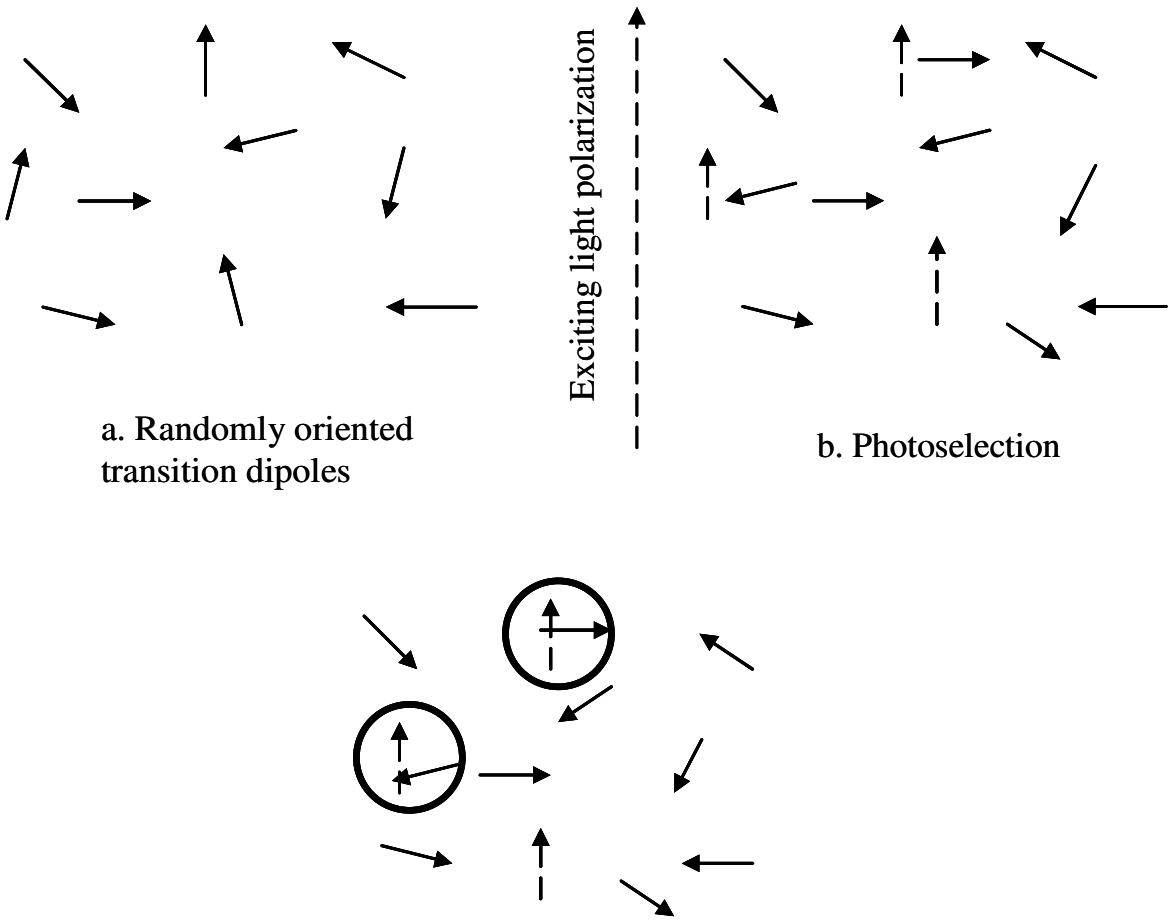

Figure 14: Polarization of fluorescence. (a) fluorophores with randomly oriented transition dipoles (b) when fluorophores with randomly oriented transition dipoles are excited with polarized light a subset of the molecules oriented parallel to the polarization of the exciting light are excited, photoselection (c) These excited fluorophores transfer energy to nearby acceptor fluorophores which subsequently emit partially depolarized fluorescence.

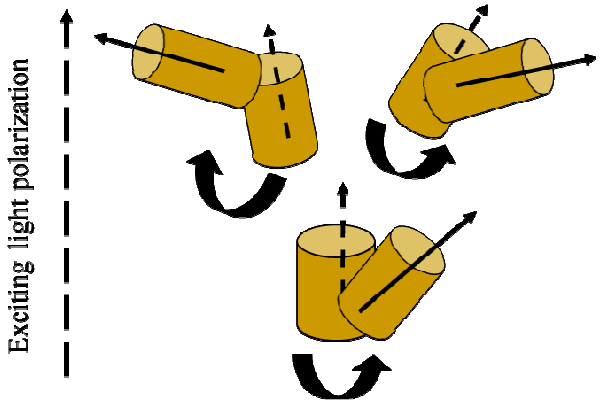

Figure 15: Fluorescence emitted after homo-FRET events has reduced polarization because the emission dipoles can be more extensively randomized with respect to the polarization of exciting light.

$$r = \frac{I_{\parallel} - GI_{\perp}}{I_{\parallel} + 2GI_{\perp}} \tag{20}$$

and, as the fluorophores are irreversibly photobleached away over time, an increase in anisotropy is observed. This is because, as fluorophores are irreversibly photobleached, the density/proximity of fluorophores decreases. Thus, anisotropy increases as photobleaching proceeds because fluorophores are getting further apart. In the limit of complete bleaching the measured anisotropy approaches that of a single fluorophore. In practice, cells labeled with YFP are bleached to 1-10% of their initial fluorescence with a polarized light source. Simultaneously, parallel and perpendicular fluorescence emission is monitored so anisotropy r can be calculated. To analyze the data anisotropy upon photobleaching versus normalized intensity an example is shown in Figure 16. FRET efficiency E is commonly calculated using Equation 20

$$\mathrm{E} = 1 - \left(r / r_0 \right) \tag{21}$$

where r_0 is an intrinsic anisotropy of a single fluorophore and r is the measured anisotropy for a group of fluorophores. Equation 21 assumes there may be energy transfer among donor species, that energy transfers do not return to the same donor and that the donor lifetime does not change [79].

Lipid rafts and techniques for study

Previous reports demonstrate that LHR is associated with lipid rafts [58, 59]. Lipid rafts (Figure 17) are plasma membrane microdomains enriched with cholesterol and sphingomyelin (Figure 18) and are signaling platforms that range in size from 10-200

nm [80]. The current model for raft-mediated receptor signaling is that receptors partition into rafts upon hormone activation and there aggregate. Other receptors that have been shown to be associated with lipid rafts are the epidermal growth factor (EGF), insulin and FcεRI [81]. Raft microdomains are held together by strong van der Waals interactions [82]. Raft sphingolipids have a saturated hydrocarbon chain that interacts with the steroid ring in cholesterol through hydrogen bonding between the amide groups in sphingolipids and the OH groups in cholesterol [83, 84]. Concentration of LHR in lipid rafts could also promote aggregation of those receptors. This concentration could be facilitated by cytoskeleton compartmentalization of the plasma membrane. Receptor oligomers could be confined to a cytoskeletally-defined compartment or could interact with proteins tethered to the cytoskeleton (Figure 19).The factors governing LHR partitioning into lipid rafts are not well understood. After hormone activation, the receptor could undergo a conformational change causing it to interact more strongly with cholesterol and sphingolipids.

Alternatively, LHR could oligomerize to yield oligomers having enhanced affinity for lipid rafts. If LHR oligomerizes before lipid raft association, this could either arise from coiling of the intracellular domain after a hormone binding-induced conformational change or from receptors being constitutively dimerized. In addition, the carbohydrates on the receptor could form intermolecular hydrogen bonds with other receptors when brought in proximity by lipid rafts.

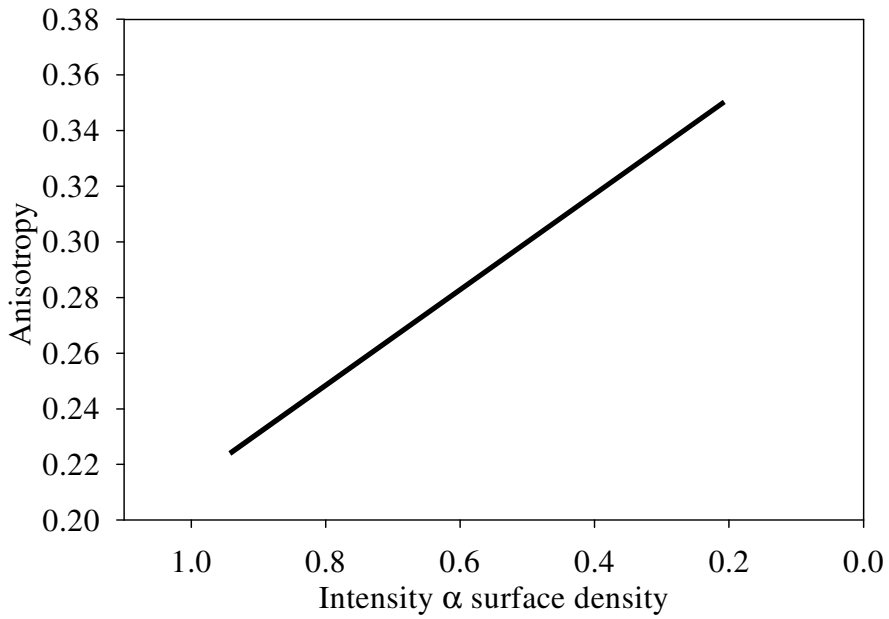

Figure 16: An example of how homo-FRET data is plotted. For homo-FRET data, anisotropy upon photobleaching versus normalized intensity is plotted for data analysis. The density/proximity of fluorophores decreases as fluorophores are irreversibly photobleached. Hence, anisotropy increases as photobleaching proceeds because fluorophores are getting further apart.

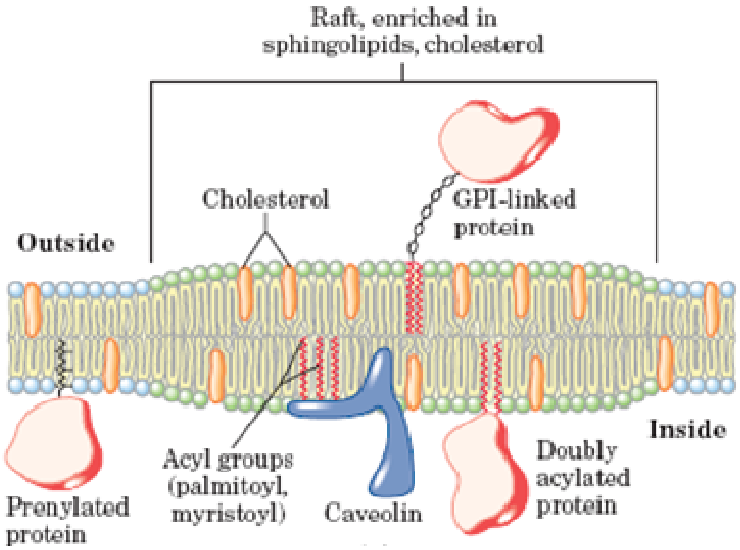

Figure 17: Diagram of plasma membrane components associated with lipid rafts. From Saslowsky et al. [85].

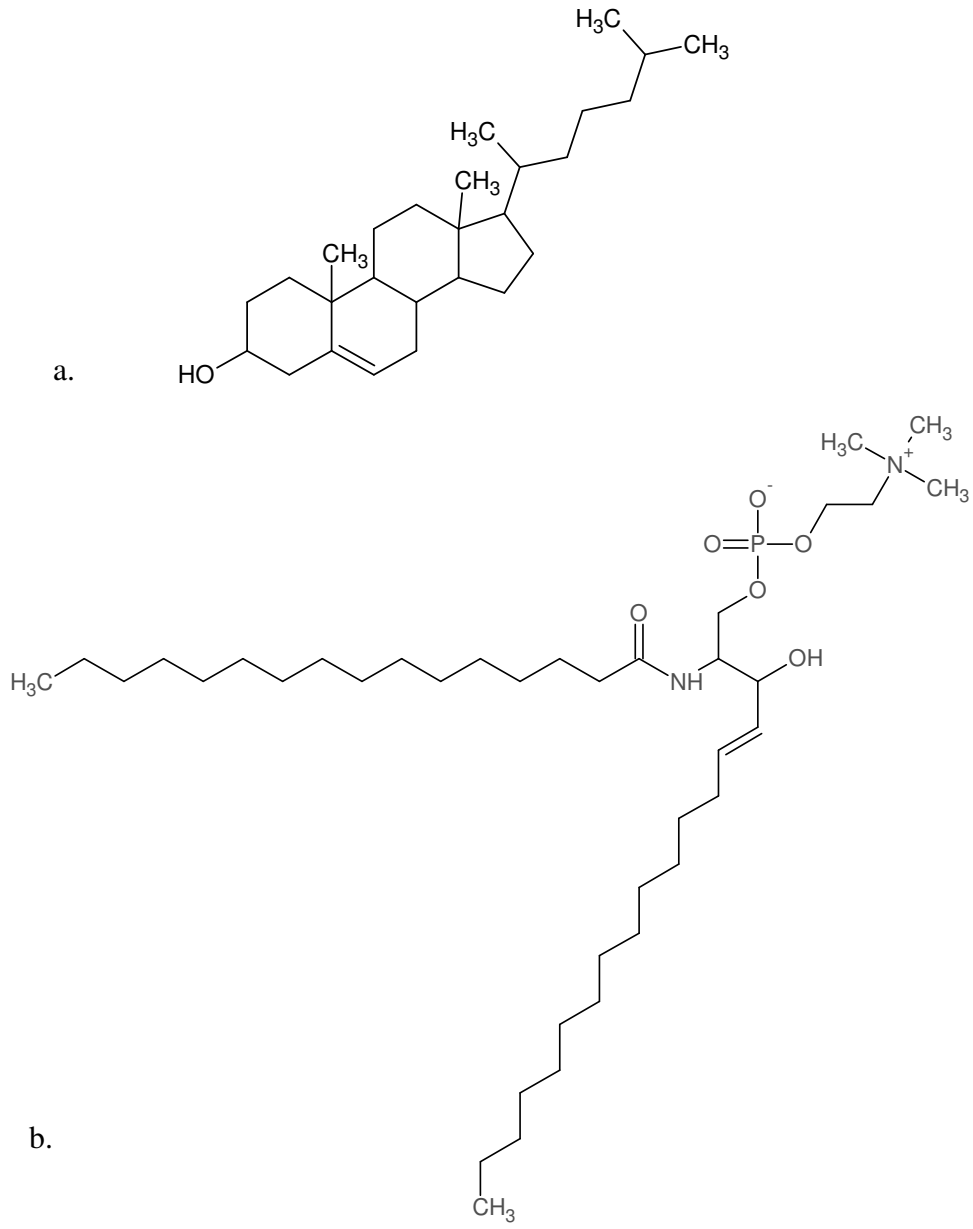

Figure 18. (a) Cholesterol structure (b) Sphingomyelin structure. Hydrophobic moieties of cholesterol and sphingomyelin interact to form lipid rafts in the plasma membrane of cells.

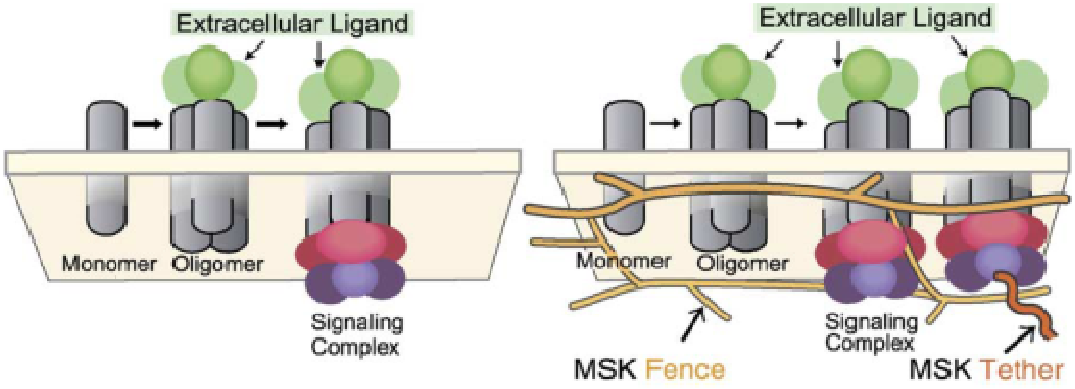

a. b.

Figure 19: Compartmentalization of the plasma membrane by the cytoskeleton could also promote aggregation of LHR. Oligomers could be confined to a compartment or could interact with a protein tethered to the cytoskeleton. (a) no compartmentalization and (b) compartmentalization with cytoskeleton. From Kusumi and Suzuki [27].

Isolation of detergent resistant membrane fragments (DRMs) is commonly used to determine if a particular receptor is present in lipid rafts [86]. A non-ionic detergent such as Triton X-100 is used along with density gradient centrifugation. Cell lysates in detergent are subjected to gradient centrifugation and the DRMs move within sucrose density gradients and translocate to rafts. The low density fractions contain the more buoyant lipid rafts and can be analyzed by western blotting to identify the receptor of interest. A difficulty with this technique is that receptors many translocate to rafts as a consequence of detergent treatment rather than being constitutively present in rafts. FRET is a more straightforward approach for these studies. Unlike density gradient ultracentrifugation, FRET is applicable to receptors *in vivo*. To determine lipid raft association with the protein of interest, a marker for lipid rafts is labeled with an acceptor fluorophore and the receptor with a fluorescent donor. Presence of the receptor in rafts is then indicated by hetero-FRET between the fluorescent donor receptors and acceptor raft lipids. Ganglioside GM1 can be labeled by B subunit of cholera toxin conjugated with a fluorophore. Another acceptor labeling method is afforded by fluorescently labeling a GPI-anchored protein. These species are plasma membrane proteins with a glycolipid attached to the protein via a carbohydrate chain and have been shown to associate with lipid rafts [87]. A third method is to employ lipids covalently conjugated with fluorescent probes such as the BODIPY fluorophore. Such fluorescent lipid derivatives include GM1 and various cholesteryl derivatives.

Recently Loew and co-workers [88] have shown that di-4-ANEPPDHQ, a membrane-staining dye, exhibits spectral differences when situated in lipid-ordered and

lipid-disordered regions of the plasma membrane. Lipid-ordered regions include lipid rafts because the structure of raft domains is rigid compared to the rest of the plasma membrane. Lipid-disordered regions include non-raft regions. The maximal possible spectral shift in di-4-ANEPPDHQ fluorescence emission maxima is 60 nm between lipid-ordered and lipid-disordered regions.

Receptor aggregation and lipid rafts in luteinizing hormone receptor signaling

Many GPCRs function as dimers or oligomers for cell signaling when hormone or other ligand binds the receptor. An example is the Type I Fcε receptor (FcεRI) [89]. In the past, the LHR also appeared to oligomerize when hormone was bound. However, some recent data has been interpreted to suggest that these LHRs may be oligomerized to some extent in the endoplasmic reticulum (ER) and trafficked to the plasma membrane where they remain oligomers. Therefore, the actual aggregation states of unliganded and liganded LHR remain uncertain.

Three techniques are commonly used alone, or in conjunction with the dynamic techniques mentioned above, to determine interactions between specific proteins. These techniques are co-immunoprecipitation, FRET and BRET. These latter techniques will be described in a subsequent separate section. In co-immunoprecipitation, cells are co-transfected with proteins containing two epitope tags, genetically-introduced protein sequences that can be recognized by specific antibodies. Cells are lysed and the lysate

centrifuged. Two antibodies are selected that exclusively bind each protein of interest. One or another of these antibodies is used to precipitate proteins bearing the particular epitope. The mixture is then centrifuged to isolate complexes from the mixture and gel electrophoresis performed to separate the proteins. The proteins from the gel are transferred to nitrocellulose paper, incubated with antibodies specific for the epitope-tagged protein of interest. This is termed a "western blot". This process is then repeated for the other epitope-tagged protein of interest. If both proteins appear at the same location on their respective blots, it provides evidence of protein interaction. Western blots can be calibrated by obtaining a control using pre-stained molecular weight standards. The disadvantage of co-immunoprecipitation is that cells have to by lysed prior to running the western blot which may disrupt less thermodynamically stable interactions.

Constitutive oligomerization of MHC class II molecules

Major Histocompatibility Complex class II receptors are transmembrane receptors associated with antigen-presenting cells such as B cells, macrophages, and dendritic cells [91]. These receptors are essential to cellular immune responses. When there is an infection in the body, MHC class II molecules present antigens, foreign molecules in the body that trigger immune responses, to T helper cells. B and T cells are groups of white blood cells also known as lymphocytes. T helper cells activated by antigen release lymphokines, chemical that help regulate immune responses. Other cells such as

phagocytes, which ingest and kill antigens, are then sent to the area of infection to create inflammatory response destroying antigens present from the disease [91].

The MHC class II molecule is a αβ-heterodimer (Figure 20). The α-chain in class II is 33-35 kDa [91, 92]. The β-chain is 25-30 kDa [91, 92]. Class II molecules are synthesized in the ER along with an invariant chain (Ii) and directed to MHC class II-containing compartments (MIIC) where Ii is degraded for antigen binding. Ii is a transmembrane glycoprotein that helps regulate antigen presentation [91, 93]. Antigens can enter the cell expressing class II molecules via endocytic mechanisms, entering endosomal compartments with distinct composition and functional properties (Figure 21). The antigens are transferred to MIIC where the class II molecules are located. The class II molecules acquire antigens in MIIC compartments and when trafficked to the cell surface they present the antigens.

Past experiments suggest indirectly that Major Histocompatibility Complex class II receptors may aggregate, [94-97] to form four-chain $(\alpha\beta)_2$ species. Since class II molecules already exist as αβ-heterodimers, such putative cell-surface aggregates are called “dimers of dimers” or “super-dimers” [98, 99]. Homo-FRET experiments provide an opportunity to directly resolve the question of whether MHC class II molecules are actually aggregated constitutively on living cell surfaces.

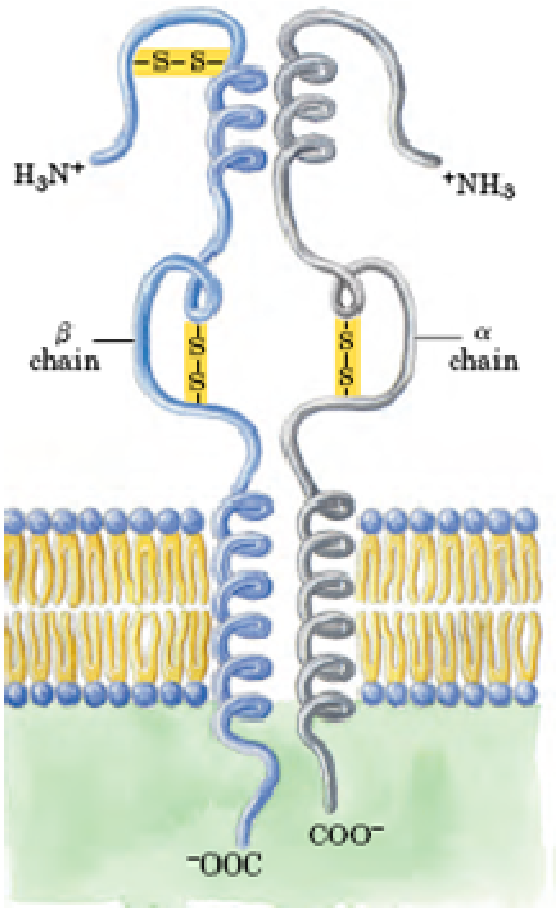

Figure 20: The MHC class II molecule is a αβ-heterodimer. The α-chain in class II is 34,000 Daltons. The β-chain is 28,000 Daltons. MHC class II has a molecular mass of 62,000 Daltons. From Lehninger [100].

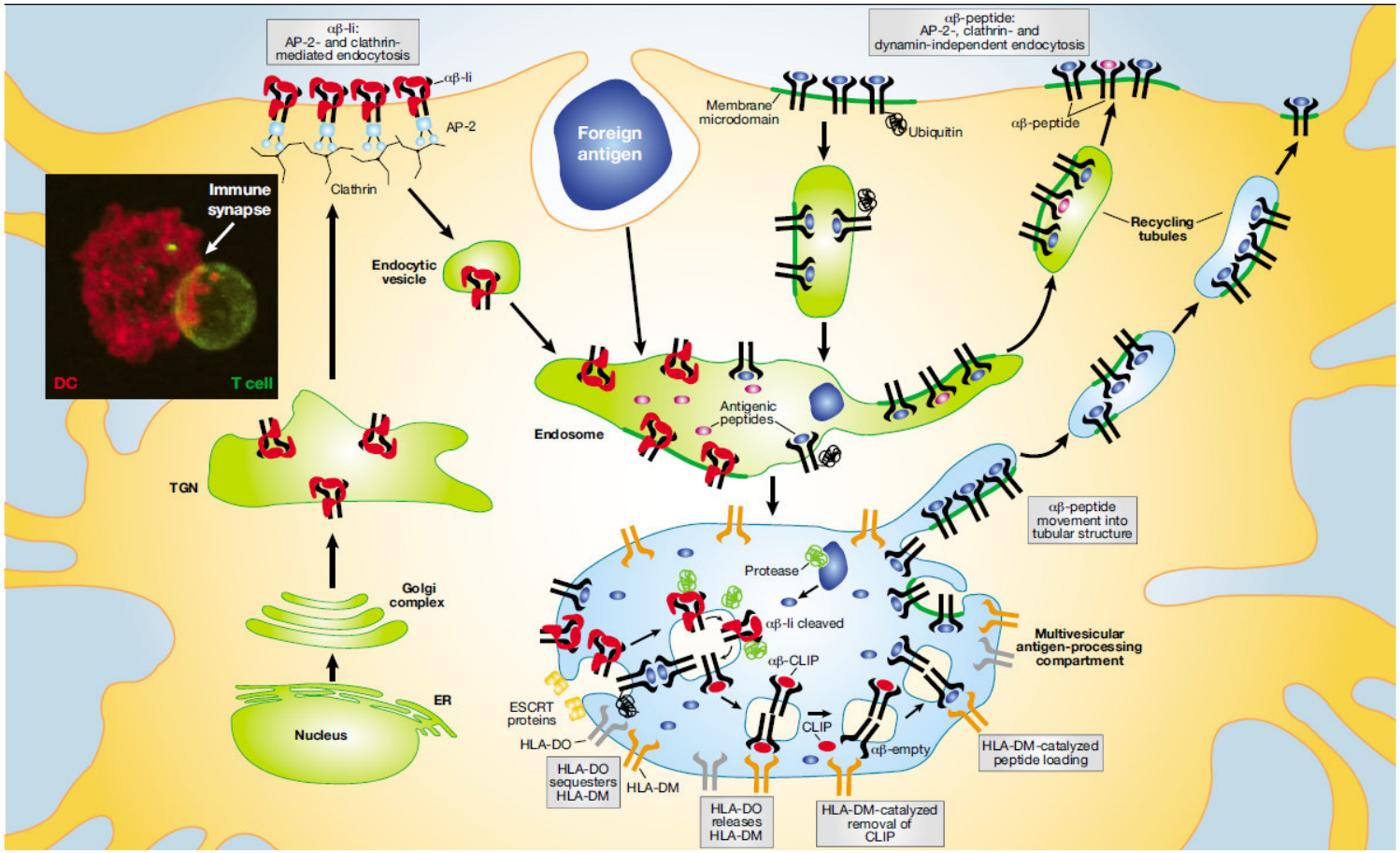

Figure 21: Class II molecules are synthesized in the endoplasmic reticulum with an invariant chain and directed to MIICs where Ii is degraded for antigen binding. Antigens can enter the cell expressing class II molecules via endocytic mechanisms, entering endosomal compartments with distinct composition and functional properties. The antigens are transferred to MIIC where the class II molecules are located. The class II molecules acquire antigens in MIIC compartments and, when trafficked to the cell surface, they present the antigens to T helper cells. From Berger and Roche [101].

Research goals

Previous work in our group has suggested that LHR on untreated cells exists as monomers located in the bulk membrane. However, upon hormone binding, or for certain mutants, receptors exist as aggregates located in lipid rafts [18, 58-67]. However, recent work using BRET measurements on LHR expressed by transient transfection have suggested that wild type LHR may be constitutively associated in the absence of hormone. The overall goal of this dissertation is to suggest how these discordant results might be reconciled.

Transient transfections are commonly used in cell experiments to examine proteins on live cells. This fast technique takes 1-2 days depending on available DNA and cells for optimal expression. However, this type of transfection leads to high expression of the DNA, possibly inducing molecular crowding that can alter signaling events. Therefore, if a technique such as FRET or BRET is used to determine self-association of a receptor, the FRET/BRET phenomenon may arise from molecular crowding and not from specific receptor interactions.

Moreover hormone-binding LHR have in the past have been found localized in lipid rafts [81]. Since rafts which can cover 2 to 30% of the plasma membrane [102, 103], local receptor concentrations may be substantially higher than expected based on overall expression levels and effects of molecular crowding.

This dissertation presents studies of possible self-association of LHR expressed on Chinese Hamster Ovary cells (CHO) cells as examined primarily by homo-FRET. The overall motivating goal is to determine whether the apparent receptor association observed in previous FRET and BRET measurements may represent molecular crowding rather than specific receptor aggregation into dimers or higher oligomers. The following specific questions are addressed:

1. Is there evidence for apparent association of LHR on untreated cells and do hormones affect this apparent association?
2. Do different receptor expression levels on individual cells affect apparent receptor association?
3. Do transfected cells exhibit a range of receptor expression levels? What numbers of receptors per cell might strongly-expressing cells possess?
4. Does theory suggest that LHR numbers measured in transfected cells could cause substantial apparent FRET/BRET simply through molecular crowding?
5. Is homo-FRET a useful general tool in assessing association in other systems?

Methods and Materials

Materials. Dr. George R. Bousfield, from the Department of Biological Sciences at Wichita State University, kindly provided human chorionic gonadotropin (hCG) and deglycosylated-hCG. Human chorionic gonadotropin was also purchased from Fitzgerald Industries (Acton, MA). Chinese Hamster Ovary cells were purchased from American Type Culture Collection (Manassas, VA). Dulbecco's Modified Eagle medium (DMEM) and geneticin were purchased from Cellgro (Manassas, VA). Penicilin/streptomycin, L-glutamine solution, and Benchmark fetal bovine serum (FBS) were purchased from Gemini-Bio-Products (West Sacramento, CA). 100 x MEM non-essential amino acid solution, bovine albumin and ethylenediaminetetraacetic acid (EDTA) were purchased form Sigma-Aldrich (St. Louis, MO). Lipofectamine 2000 reagent was purchased from Invitrogen (Carlsbad, CA). Quantum FITC MESF (molecules of equivalent soluble fluorophore) beads were purchased from Flow Cytometry Standards Corporation (San Juan, PR). WillCo Wells glass bottom cell culture dishes with 35 mm diameter and 12 mm diameter glass bottoms were purchased from Warner Instruments (Hamden, CT).

Cell lines. CHO cells transiently transfected were prepared with 1.6 μg of hLHR-eYFP, kindly prepared by Ying Lei, Department of Physiology at Colorado State University, using Lipofectamine 2000 in accordance with Manufacturer's instructions. Two microcentrifuge tubes each containing 100 μL of complete CHO media, outlined below without geneticin, had 1.6 μg of hLHR-eYFP in one microcentrifuge tube, 4 μL of Lipofectamine 2000 in the other microcentrifuge tube and they were incubated at room

temperature for 5 minutes. The two microcentrifuge tubes containing the DNA and lipofectamine are mixed together into one tube and incubated at room temperature for 30 minutes. This volume is then added to the cells in 35 mm petri dishes. Transfection proceeds for 41-43 hours. After transfection, cells were imaged or treated with hormones. Transfected cells were maintained in Dulbecco's Modified Eagle medium (DMEM) with 10% FBS, 1% P/S, 1% L-glutamine, 1% 1x non-essential amino acids and 200 μg/mL of geneticin. Untransfected CHO cells were maintained in the same media above but without geneticin. All cells were maintained in 5% CO_2 at 37°C.

Sample preparation for homo-FRET. After cells were 80-90% confluent in a 25 cm^2 culture flask, cells were incubated with 5 mM EDTA for 3 min and 0.5-1.0 mL of cells were plated in a 35 mm glass bottom petri dish. After 4 hours or overnight culture, the cells were transiently transfected. Cells were washed twice with 1xPBS and immediately imaged as described below.

Sample preparation for flow cytometry. Cells were grown to 80-90% confluence in a 25 cm^2 culture flask. Next, cells were incubated with 5 mM EDTA for 3 min in that same culture flask and the flask was partly washed with 3 mL of 1xPBS. The 3 mL of cell suspension was then placed in a 15 mL centrifuge tube analyzed using the MOFLO Flow Cytometer and High Speed Cell Sorter (Dako Colorado, Inc) with Quantum FITC Molecules of Equivalent Soluble Fluorophores (MESF) bead standards at Colorado State University Department of Environment and Radiological Health Sciences flow cytometry facility. The beads are 7.2 μm in size. The MESF values for the blank, bead standard 1,

bead standard 2, bead standard 3 and bead standard 4 are 0, 33024, 109996, 317482 and 1580198, respectively. Fluorescence intensity was collected using a 488 nm argon ion laser as an excitation source, a 530/30 nm emission filter and the amplifier operating in the logarithmic mode.

Homo-FRET measurements. The Förster distance for the YFP-YFP donor-acceptor pair is 5.11 nm [104] so that energy transfer between such chromophores occurs only when donor-acceptor pairs are 1-10 nm apart. Homo-FRET data were collected on the Olympus FV300 confocal laser scanning microscope. Fluoview software allows visualization of cells during experiments. Fluorescence emission was collected using a 488 nm argon ion laser to bleach the cells to ~10% of initial fluorescence within approximately 30 images. Parallel and perpendicular fluorescence emission images, with respect to polarization of exciting light, were collected simultaneously using a polarizing beam splitter that is directly placed in front of the photomultiplier tubes (PMTs) (Figure 22). A 535/50 nm emission filter was used to isolate YFP fluorescence. A 300 μm confocal aperture placed directly in front of the polarizing beam splitter (Figure 22) was used. The confocal aperture provides z-axis resolution by rejecting light above and below the focal plane. All cells were focused on the equatorial plane, which appear as a ring-like shape (Figure 23). Cells were bleached for 2-3 minutes while being imaged with one cell per image. Images for g-factor calculation were acquired by lowering transmitted light until both the parallel and perpendicular channels were medium-gray, namely about 2000 units of a maximum of 4095. Background images were taken by completely minimizing any transmission of light in the microscope and coving the objective with

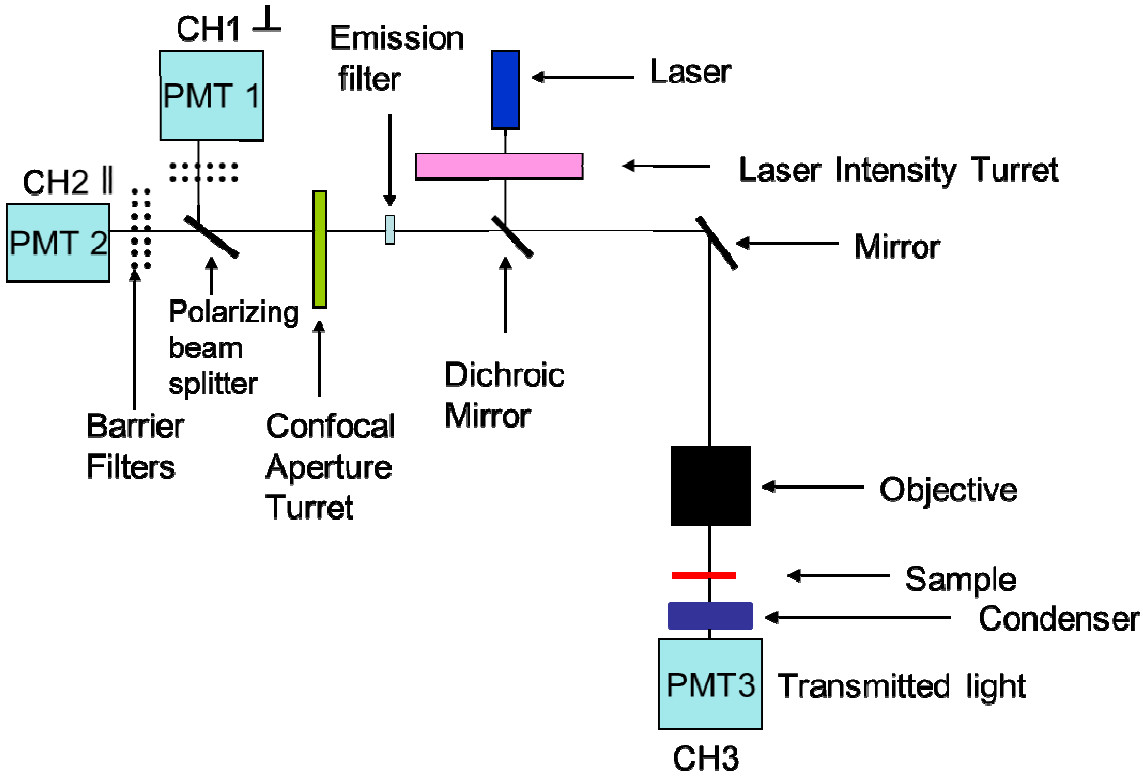

Figure 22: Light path for FV300 Confocal Scanning microscope. There are three channels to monitor parallel, perpendicular emission and transmitted light images. An emission barrier filter is placed before aperture turret which, in turn, is located in front of the polarizing beam splitter.

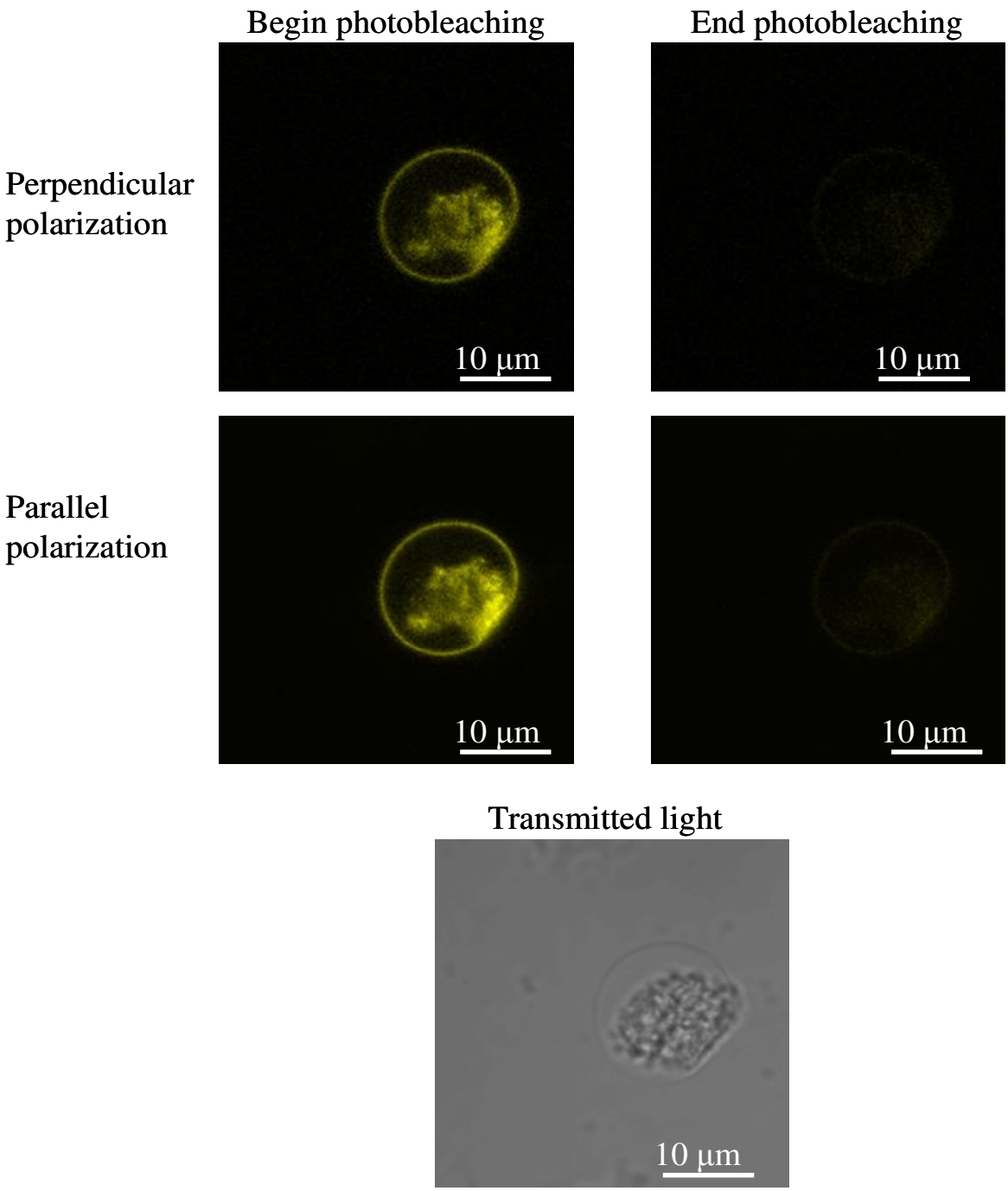

Figure 23: Confocal images of a CHO cells transfected hLHR-YFP and photobleached during homo-FRET. The two images on the top are perpendicular fluorescence emission polarized perpendicular to the excitation polarization and the two images on the bottom are florescence emission polarized parallel to the excitation polarization. The images on the left are when photobleaching begins and on the right where photobleaching ends. The bottom picture is the transmitted light image of the cell.

a black cap. Background and g-factor images were analyzed in Adobe Photoshop 7.0. Background was subtracted from fluorescence emission images and g-factor was applied to correct for different sensitivities that arise from the two PMT detectors. G-factor is calculated using Equation 19. Masking of the cells was performed in Adobe Photoshop 7.0 to isolate the ring-like membrane fluorescence. The brush tool with a diameter of 9 pixels was used. Masking allows for analyzing only the fluorescence emission from the cell membrane and rejecting out-of-focus cytoplasmic fluorescence. Using a custom analysis program, background was subtracted from each image and anisotropy calculated using Equation 21. The intrinsic anisotropy, which is the anisotropy value of a single isolated eYFP fluorophore, was set to 0.35 for all cells, close to the value Clayton and co-workers [23] assumed for eYFP. For each petri dish, 10-20 cells are analyzed.

Flow cytometry data analysis. To determine the range of receptor numbers on transfected cell populations, FITC fluorescence signal intensities measured in cytometer for Quantum MESF beads needs to be related to signals measured for hLHR-eYFP on the cell surfaces. In a Quantum MESF kit, each microsphere population is assigned a value corresponding to the number of FITC molecules in solution which give a same signal as the bead. For example, a Quantum FITC microsphere with an MESF value of 50,000 has the same fluorescence intensity as an equivalent volume of solution containing 50,000 FITC molecules. There are no bead standards for eYFP or for other fluorophores such as cyan fluorescent protein (eCFP), blue fluorescent protein (eBFP) and red fluorescent coral protein (DsRed). Hence, being able to convert measurements performed FITC standard beads to another fluorophore signal obtained for cell samples is essential.

Calculations for FITC to YFP signal conversion. Ignoring any wavelength dependence of detector quantum efficiency over emission filter bandwidth, relative fluorescence signal F for various fluorophores measured in an instrument at constant settings will be

$$F = \frac{a(\lambda_e)}{a(\lambda_{pk})} \; \varepsilon(\lambda_{pk}) \; \frac{\sum_{\lambda_d - w_d/2}^{\lambda_d + w_d/2} f_\lambda}{\sum_{0}^{\infty} f_\lambda} \Phi_f \; I \; n \qquad (22)$$

where $a(\lambda_e)$ is the absorbance for a given fluorophore at the excitation wavelength λ_e, $a(\lambda_{pk})$ is the maximum absorbance value, $\varepsilon(\lambda_{pk})$ is the molar absorptivity for the given fluorophore, f_λ is some linear measure of fluorescence intensity at wavelength λ, λ_d is detector wavelength, w_d is emission filter band width, Φ_f is fluorescence quantum yield, I is intensity and n is the number of fluorophores. From Equation 22, $\sum_{\lambda_d - w_d/2}^{\lambda_d + w_d/2} f_\lambda$ is the sum of absorbance values from 510-550 nm and $\sum_{0}^{\infty} f_\lambda$ is the sum of absorbance values from 250 nm to 650 nm. Table 1 shows the values for Equation 22 for FITC, Alexa 488, eGFP, and eYFP. Dividing the fluorescence of FITC by that of eYFP yields a value for how many eYFP yield a signal equal to a single FITC molecule. We calculate a value of 2.0 eYFP per apparent FITC. Excel 2003 was used to create a calibration curve of intensity measured in cytometer versus number of FITC per bead.

Statistics. All values, unless otherwise noted, are means ± SEM where numbers of points n are given in the text and/or in the corresponding table. Mean values asserted to differ yield $p<0.05$ in Student's t-test.

Results

LHR exhibit apparent association on untreated cells and hormone treatments affect this apparent association

Experiments to assess the possible presence of self-association of hLHR on CHO cells were performed. Additionally, effects of different hormone treatments on hLHR self-association were explored. The technique of homo-FRET was chosen to examine self-association of hLHR. This method has the advantage of requiring molecular labeling with only a single fluorophore type.

CHO cells were transiently transfected with hLHR-eYFP DNA in 35 mm glass bottom petri dish in complete CHO medium containing geneticin and maintained at 5% CO_2 and 37°C. Transfected cells were incubated at 5% CO_2 and 37°C for 20 minutes with 100 nM hCG, a ligand that activates the receptor. Transfected cells were incubated at 5% CO_2 and 37°C for 20 minutes with 100 nM DG-hCG, a related ligand, which inhibits receptor activity. Transfected cells not treated were used as the control. Data were collected in the dark with the FV300 confocal scanning microscope at room temperature using a 488 nm argon ion laser with laser power reduced to 20% of total

Table 1: Summary of fluorescence parameters for FITC, Alexa 488, eGFP and eYFP excited at 488 nm. These quantities can be used to convert flow cytometer signal from FITC bead standards to numbers of other fluorophore species that may be present on sample cell surfaces.

Fluorophore	$a(\lambda_e)$ (au)	$a(\lambda_{pk})$ (au)	$\varepsilon(\lambda_{pk})$ (L mol^{-1} cm^{-1})	$\sum_{\lambda_d - w_d/2}^{\lambda_d + w_d/2} f_\lambda$	$\sum_{0}^{\infty} f_\lambda$	Φ_f	Relative fluorescence (Equation 21)
FITC	77.3	100	68,000	2981	5010	0.95	28815
Alexa 488	75.2	100	71,000	3081	4951	0.92	30568
eGFP	100	100	50,000	2066	3850	0.60	16099
eYFP	38.1	100	84,000	2723	3809	0.61	13956

laser intensity. Fluorescence intensity was collected using a 535/50 nm emission filter. Images were acquired in a single plane over time with scan speed set to 0.45 seconds per scan. Focus mode was set to x4 to increase scan speed by four fold. Kalman filtering was used to average a specific number, typically, 6-8, of raw images for each image recorded. A sequence of 20-30 images was recorded per cell. After the sample is placed on the microscope stage, a cell is brought into focus on the microscope and viewed in Fluoview. Optical zoom ranged from 4x to 7x so that only one cell would be imaged at a time with 256 by 256 pixels per image. Detector channel voltages, which allow detector sensitivities to be adjusted, were set to obtain a suitable bright image. The cell was then bleached to ~10% of initial fluorescence intensity. G-factor and background images were collected at the end of experiments at every voltage setting used.

Homo-FRET measurements begin with acquisition of 20 to 30 sequential images of fluorescence polarized parallel and perpendicular to excitation polarization as samples are bleached. Intensities in parallel and perpendicular images are analyzed to yield average intensities and anisotropies in the annular region of interest defined by a mask isolating a region of cell membrane. The average intensities and anisotropy upon photobleaching are plotted as a function of time (see Figure 24a). Then, intensities are normalized to the range 0 to 1 (see Figure 24b), where 1 represents the initial fluorescence observed and 0 represents a cell fully bleached. Anisotropy is corrected so that the final anisotropy after complete bleach is 0.35. The corrected anisotropy at various degrees of photobleaching is then plotted versus normalized fluorescence. Change in anisotropy upon photobleaching, calculated as initial anisotropy ($r_{initial}$) subtracted from

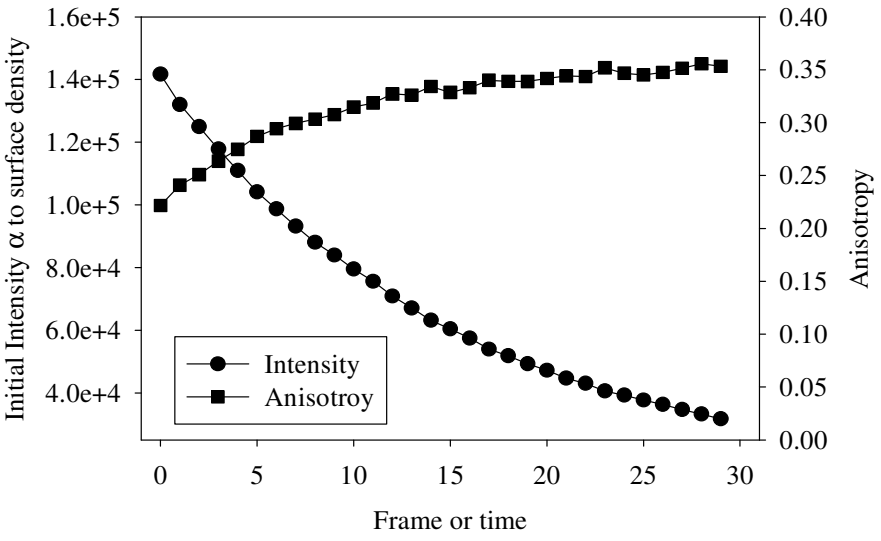

a.

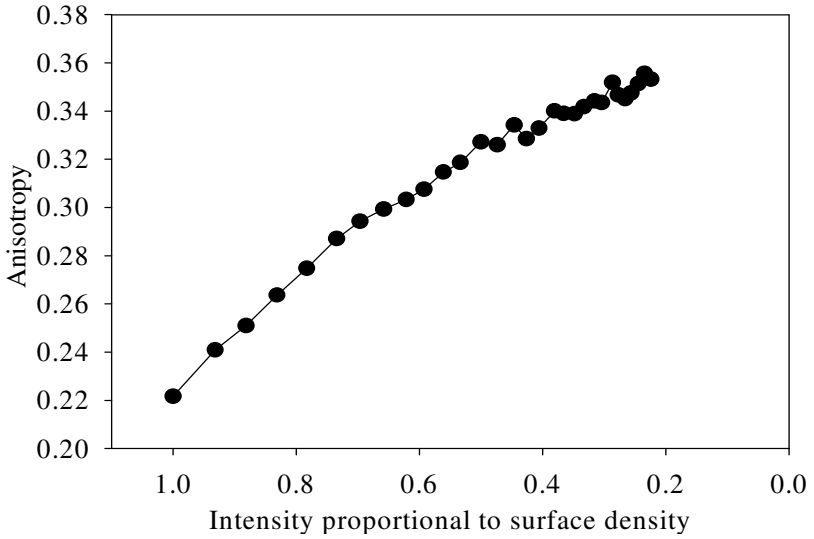

b.

Figure 24 a-b: Raw data from homo-FRET (a) As the fluorophores are irreversibly photobleached over time, anisotropy upon photobleaching increases. This is because, as the fluorophore is irreversibly photobleached, density/proximity of the total fluorophores decreases. Thus, anisotropy upon photobleaching increases because fluorophores become further apart and the value is approaches that of a single fluorophore. (b) Analysis of the data is best performed by examination of a plot of anisotropy upon photobleaching vs. normalized intensity.

final anisotropy (r_{final} or r_0), reflects either specific molecular aggregation and/or molecular proximity arising simply from concentration. Oligomers of fluorescent species have reduced anisotropy relative to that observed with single molecule excited by a linearly-polarized laser source because energy transfer from neighboring fluorophores in varying orientations. Thus change in anisotropy upon photobleaching can indicate if receptors are specifically associated in close proximity due to high receptor densities on the surface of the cell. Homo-FRET efficiency (%E) is calculated from $r_{initial}$ and r_0 using Equation 21.

Hormone treatment affects apparent hLHR self-association. Anisotropy versus normalized intensity for cells undergoing photobleaching was plotted for untreated CHO hLHR-eYFP cells and for cells treated with hCG and DG-hCG (Figure 25). Table 2 shows average anisotropy changes for these three cell groups. For control cells, namely those not treated, the average change in anisotropy upon photobleaching is 0.081±0.006. After hCG treatment, the change in anisotropy upon photobleaching increases to 0.099±0.010 for hCG-treated cells, which suggests that that there is increased oligomerization caused by this treatment. For DG-hCG treatment, the change in anisotropy upon complete photobleaching, decreases relative that for to untreated cells to 0.058±0.006, which is significantly lower than the control and hCG treated cells. This reduced change in anisotropy upon photobleaching for DG-hCG suggests that DG-hCG reduces oligomerization relative to untreated cells. Figure 26 shows that the change in anisotropy upon photobleaching is larger for hCG compared to the control and DG-hCG, and that DG-hCG has the lowest change in anisotropy. However, the change in

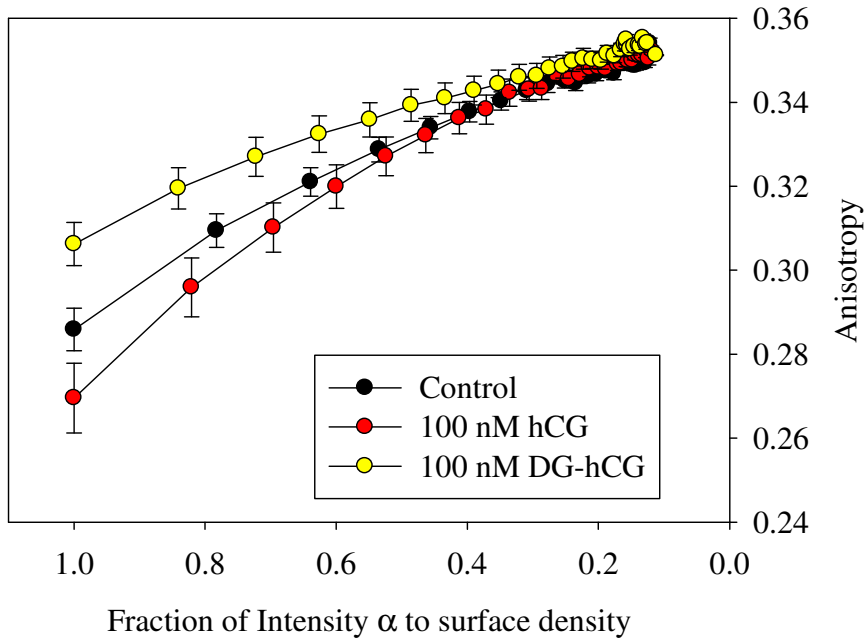

Figure 25: The change in anisotropy upon hormone treatment is larger for hCG-treated cells compared to the control and DG-hCG treated cells. DG-hCG treated cells exhibited the lowest change in anisotropy upon photobleaching. The intrinsic anisotropy was set to 0.35 which is the value of one fluorophore after all the other fluorophores have been irreversibly photobleached. The change in anisotropy upon photobleaching increases with hCG treatment, which further supports the notion that hCG increases oligomerization. For DG-hCG the change in anisotropy upon photobleaching decreases which is significantly lower than the control and hCG treated cells. This decrease in change in anisotropy for DG-hCG supports the assertion that DG-hCG suppresses oligomerization.

Table 2: Summary of change in anisotropy upon photobleaching for hCG and DG-hCG treated cells plus a control. CHO-hLHR-eYFP cells were untreated and treated with 100 nM hCG and DG-hCG. Data shown are means ± SEM for indicated number of cells.

Cell Line	Treatments	number of cells examined	final-initial anisotropy
Control	None	67	0.081 ± 0.006
CHO hLHR-eYFP	hCG (100 nM)	37	0.099 ± 0.010
CHO hLHR-eYFP	DG-hCG (100 nM)	46	0.058 ± 0.006

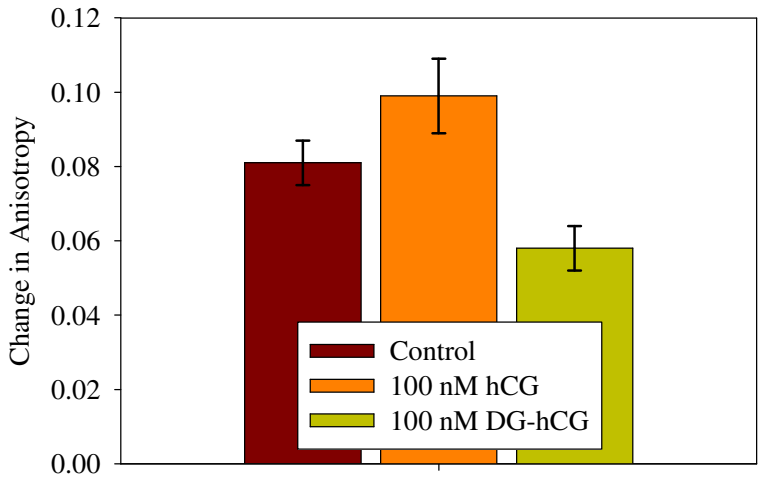

Figure 26: Change in anisotropy upon photobleaching for CHO hLHR-YFP upon hCG and DG-hCG treatment. For untreated control cells, the change in anisotropy upon photobleaching is 0.081±0.006. The change in anisotropy upon photobleaching increases to 0.099±0.010, which further supports that hCG increases oligomerization. For DG-hCG the change in anisotropy upon photobleaching decreases to 0.058±0.006, which is significantly lower than the control and hCG treated cells. This decrease in change in anisotropy, upon photobleaching supports the hypothesis that DG-hCG treatment suppresses oligomerization.

anisotropy upon photobleaching remained high relative to untreated cells on the plasma membrane, supporting that hLHR transiently transfected on CHO cells are constitutively oligomerized. This can be seen in more detail in Figure 26 and Table 2.

These anisotropy changes upon photobleaching can be converted to efficiencies of homo-FRET between LHR by using equation 16. These average results are shown in Figure 27. CHO cells transfected to express hLHR-eYFP at high concentrations exhibit relatively high values homo-FRET efficiencies ranging from 17 to 28%. Control cells had a homo-FRET efficiency value of 23±2%, FRET efficiencies values exceeding 5% generally being considered to be significant [105]. Hence, the extent of apparent FRET exhibited by all treatment groups requires explanation.

With 100 nM hCG treatment, homo-FRET efficiency increased from 23±2% to 28±3% and this small increase in homo-FRET efficiency in cells treated with hCG suggests that adding hormone to LHR promotes oligomerization. The homo-FRET efficiency decreased from 28±3% to 17±2% when transfected cells were treated with 100 nM DG-hCG, which inhibits receptor activity. This decrease in homo-FRET efficiency suggests that DG-hCG suppresses oligomerization.

In summary, the high FRET efficiencies observed on untreated cells could arise either from constitutive aggregation of LHR or possibly from inter-receptor proximity caused simply by high receptor surface density. We cannot say which at this point. As regards hCG-treated cells, since hCG treatment does not increase surface expression, the

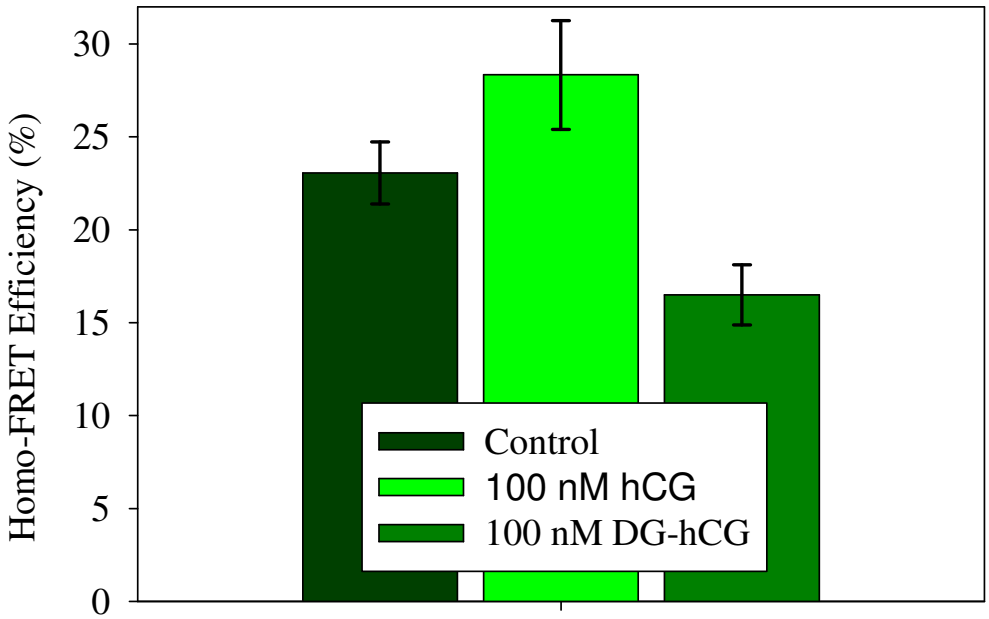

Figure 27: Homo-FRET efficiencies for CHO hLHR-YFP. Control cells had a homo-FRET efficiency of 23±2 %. FRET efficiencies of 5% or more are considered significant. This suggests that there is aggregation prior to treatment with hCG for transiently transfected cells or that the receptor surface is high enough to induce FRET by non-specific concentrated effects. With 100 nM hCG treatment, homo-FRET efficiency is significantly different, compared to the control cells. This small increase in homo-FRET efficiency, with cells treated with hCG, suggests that adding hormone to LHR promotes oligomerization. The homo-FRET efficiency decreased when transfected cells where treated with 100 nM DG-hCG, which inhibits receptor activity.

fact that we observe increased FRET efficiency after hCG treatment suggests that this increase (and only this increase) arises from aggregation. Similarly, for DG-hCG-treated cells, since DG-hCG treatment does not decrease surface expression, we infer that the decreased FRET efficiency arises from reduced aggregation. However, without further information, we cannot identify the origin of the very substantial FRET efficiency still present after DG-hCG treatment. Hence, we have not yet demonstrated significant constitutive specific receptor aggregation as distinct from possible concentration-based FRET caused by high surfaces densities.

LHR expression levels affect apparent receptor self-association

The high extents of FRET between receptors on control cells and on hCG- and DG-hCG-treated cells could arise either from specific aggregation of receptors or from simple molecular proximity arising from high surface concentrations. If observed FRET arises from receptor surface concentrations, then the initial anisotropy of cells should be lower for cells with high surface concentrations, that is, for cells with higher fluorescence intensities at the start of bleaching.

To determine if receptor density if fact affects anisotropy changes, initial anisotropy was examined as a function of normalized initial fluorescence intensity which is proportional to receptor surface density for control cells (Figure 28). The uncertainty in measurement of g-factors from cell to cell contributes to the variance of among anisotropy measurements. To minimize this effect, the g-factor was corrected for each

individual cell so that the final anisotropy at complete bleaching was 0.35. As initial receptor surface density increased, the initial anisotropy values decreased. For cells treated with 100 nM hCG or with 100 nM DG-hCG, as surface density increases, the initial anisotropy values also decreased as shown in Figure 29. The slopes of these initial anisotropy versus initial intensity plots reflect receptor aggregation as concentration-dependence of receptor proximity. Table 3 shows slopes of $-1.9\text{x}10^{-6}\pm1.2\text{x}10^{-7}$ and $-2.2\text{x}10^{-6}\pm1.7\text{x}10^{-7}$ for the control and 100 nM hCG treated cells, respectively. The steeper slope supports the notion that hCG promotes concentration-dependent aggregation. Cells treated with 100 nM DG-hCG, a hormone that inhibits receptor activity, also demonstrated decreasing initial anisotropy as surface density increased as seen in Figure 30. Compared to the control and hCG treatment, the slope of $-8.8\text{x}10^{-7}\pm2.7\text{x}10^{-7}$ for DG-hCG is less steep and this supports the idea that DG-hCG inhibits aggregation.

Data can also be plotted showing FRET efficiency as a function of initial intensity, which is proportional to receptor surface density, for individual cells. These data showed that, as receptor surface density increased, so did FRET efficiency (see Figure 31). After cell treatment with 100 nM hCG, FRET efficiency increased more strongly with surface density, Figure 32. Table 4 shows that the intercepts of these curves are grossly equal suggesting high-affinity constitutive aggregation. However, the concentration dependence of FRET efficiencies is higher for hCG treated cells. This is reflected in the slope values of $5.0\text{x}10^{-4}\pm0$ and $5.4\text{x}10^{-4}\pm1.8\text{x}10^{-20}$ for the control and cells treated with 100 nM hCG, respectively. Since both the control and hCG treated cells

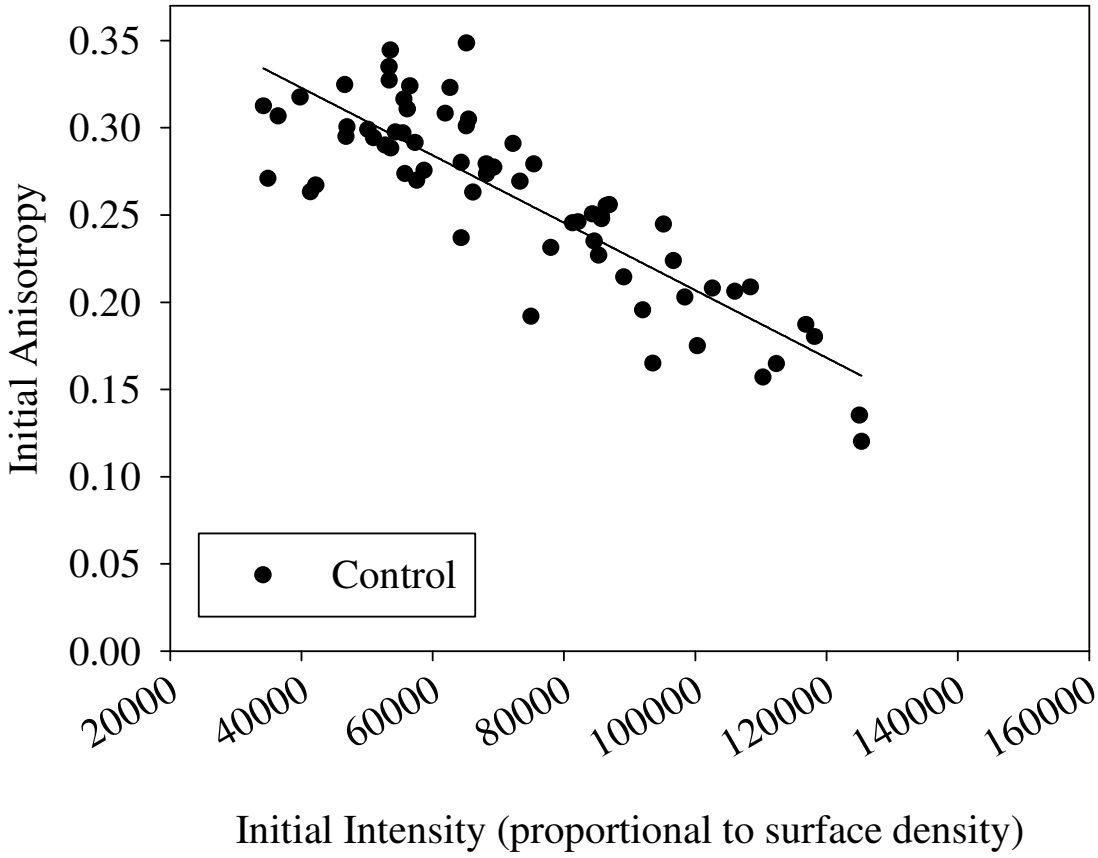

Figure 28: Plot of initial anisotropy versus initial intensity for untreated CHO hLHR-eYFP cells. As the surface density increases, the initial anisotropy values decrease suggesting that low-order oligomers may be predominate at lower receptor concentrations while at higher receptor concentrations mostly high-order oligomers.

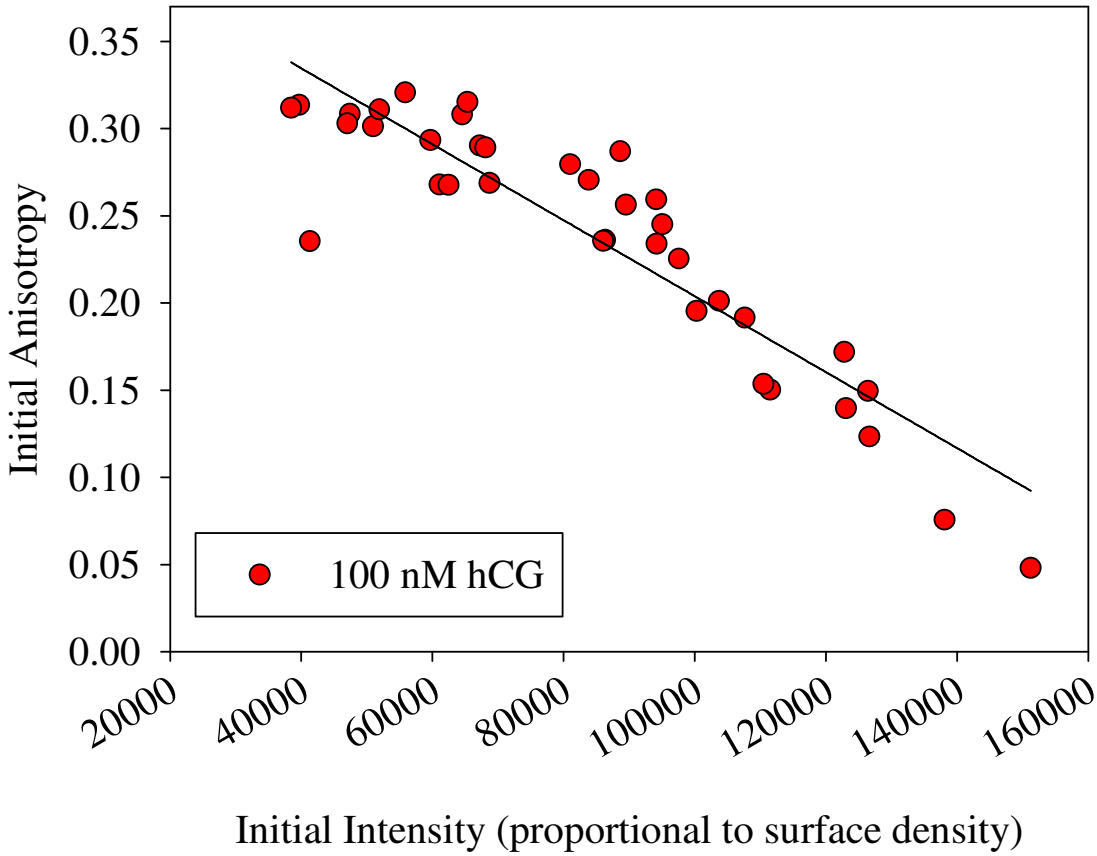

Figure 29: Plot of initial anisotropy versus initial intensity for CHO hLHR-eYFP cells treated with 100 nM hCG. Compared to the control, the hCG treated cells exhibit a steeper slope of $-2.2\times10^{-6}\pm1.7\times10^{-7}$ than that for control cells, $-1.9\times10^{-6}\pm1.2\times10^{-7}$, supporting the notion that hCG promotes concentration-dependent receptor aggregation.

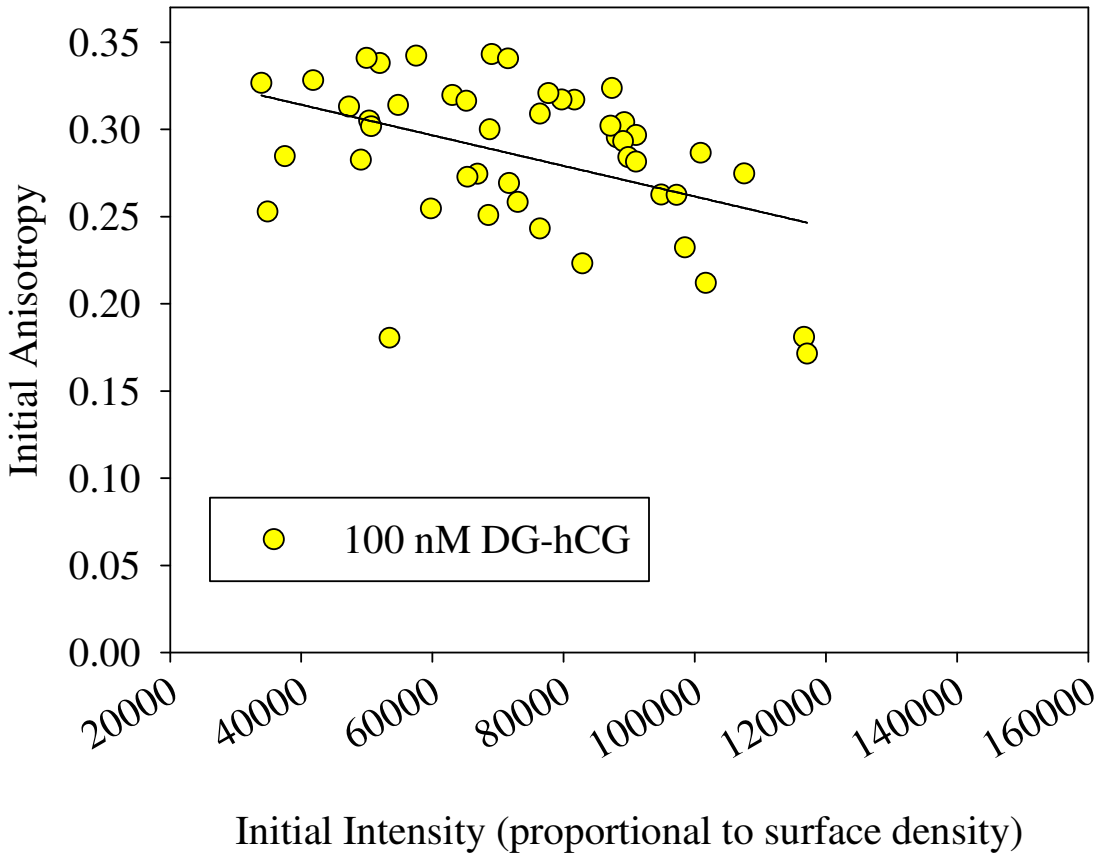

Figure 30: Plot of initial anisotropy versus initial intensity for CHO hLHR-eYFP cells treated with 100 nM DG-hCG. Compared to the control the hCG treated cells and the slope for DG-hCG slope of $-8.8 \times 10^{-7} \pm 2.7 \times 10^{-7}$ lower than that for control cells, $-1.9 \times 10^{-6} \pm 1.2 \times 10^{-7}$, supporting the notion that DG-hCG decreases receptor aggregation.

Table 3: Slope and intercept values for plots initial anisotropy versus initial intensity (proportional to receptor surface density) graphs. CHO-hLHR YFP cells were untreated and treated with 100 nM hCG and DG-hCG. Data shown are ± standard deviation.

Cell type	Treatment (100 nM)	number of cells examined	Intercept	Slope
Control	None	67	$4.0 \times 10^{-1} \pm 1.1 \times 10^{-2}$	$-1.9 \times 10^{-6} \pm 1.2 \times 10^{-7}$
CHO hLHR-eYFP	hCG	37	$4.2 \times 10^{-1} \pm 1.5 \times 10^{-2}$	$-2.2 \times 10^{-6} \pm 1.7 \times 10^{-7}$
CHO hLHR-eYFP	DG-hCG	46	$3.5 \times 10^{-1} \pm 2.1 \times 10^{-2}$	$-8.8 \times 10^{-7} \pm 2.7 \times 10^{-7}$

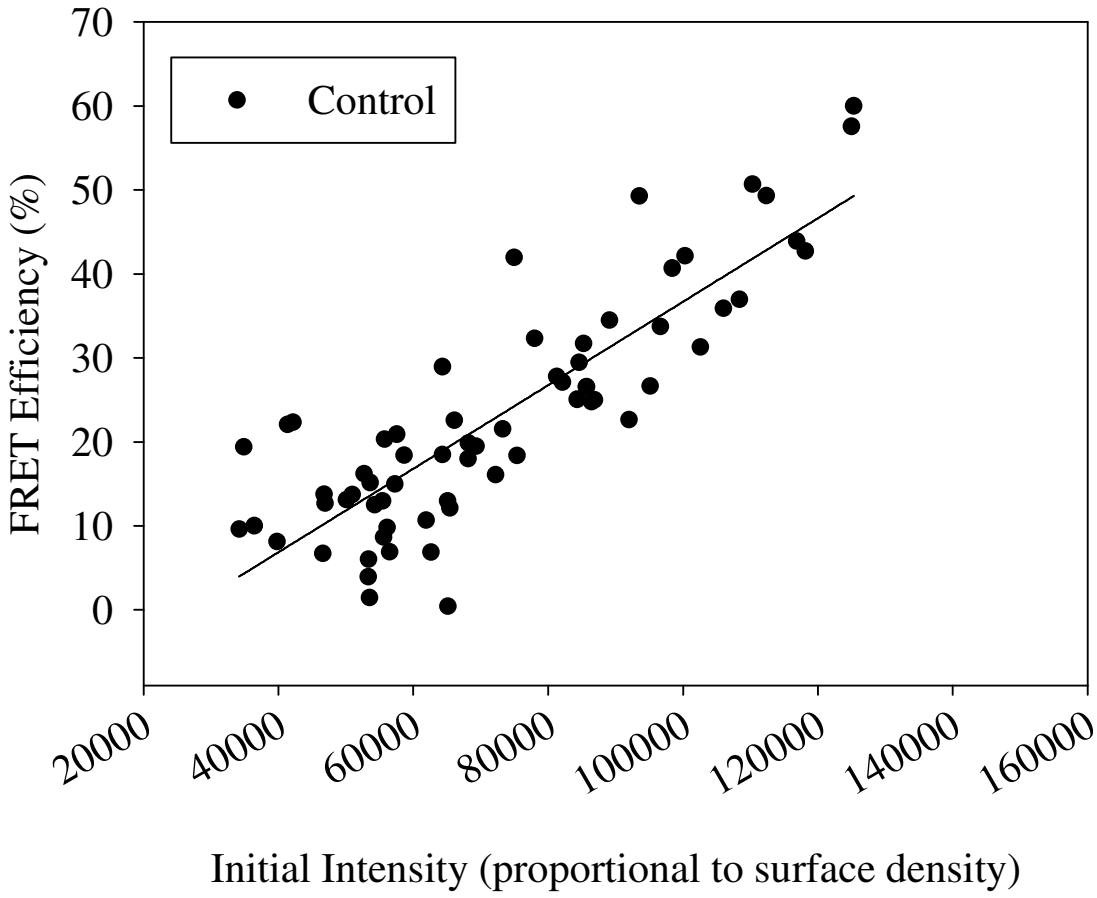

Figure 31: Plot of FRET efficiency versus initial intensity for untreated CHO hLHR-eYFP cells. As the hLHR surface density increased, FRET efficiency increased suggesting FRET suggesting FRET efficiency for hLHR is receptor concentration dependent.

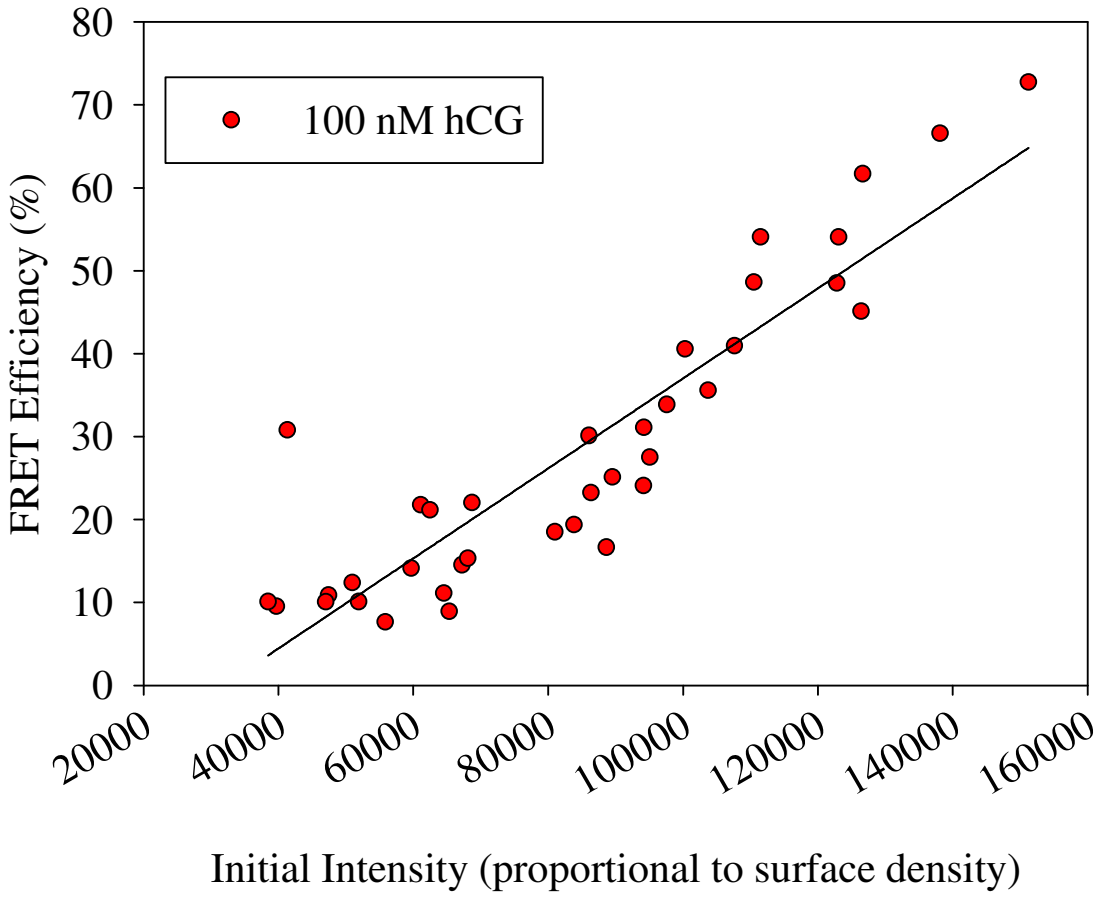

Figure 32: Plot of FRET efficiency versus initial intensity for CHO hLHR-eYFP cells with 100 nM hCG. With 100 nM hCG treatment, there increase in FRET efficiency as receptor surface density increased, the intercept of the curve was lower than for untreated cells. This suggests that hCG treatment increases oligomerization.

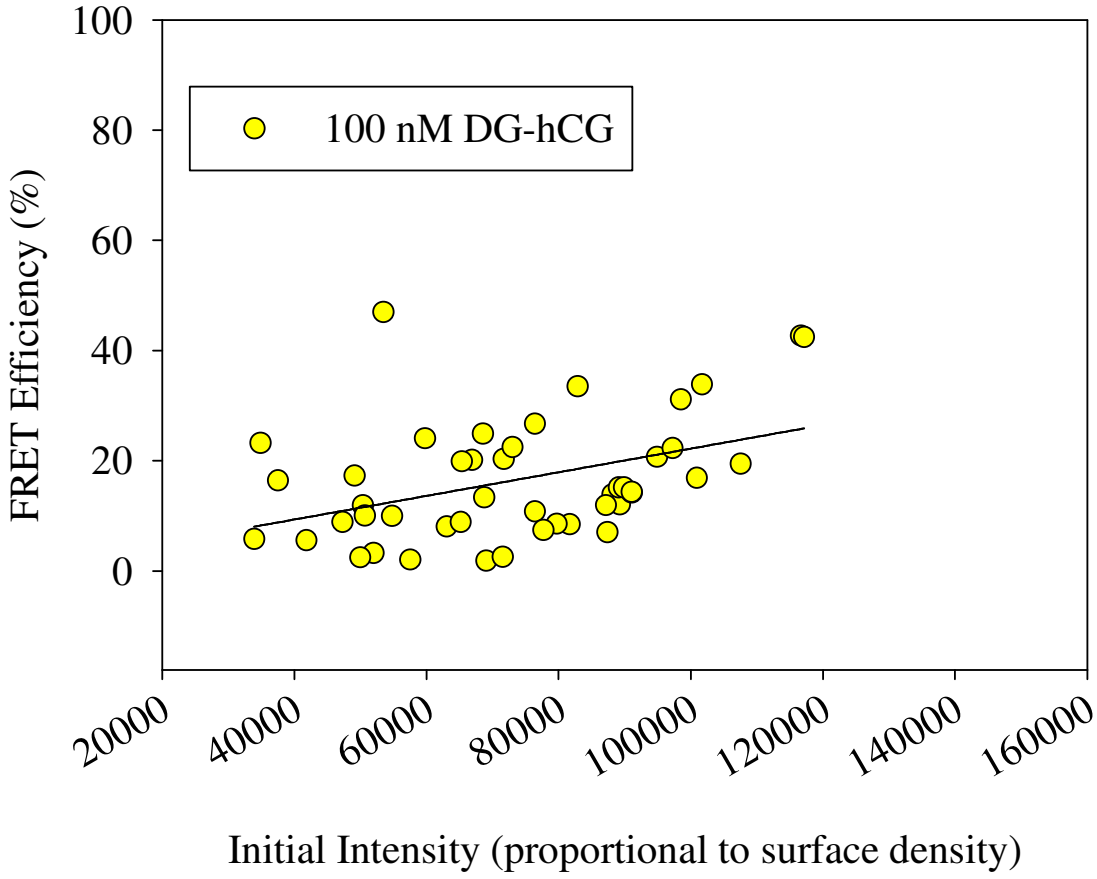

Figure 33: Plot of FRET efficiency versus initial intensity for CHO hLHR-eYFP cells with 100 nM DG-hCG. With 100 nM hCG treatment, there increase in FRET efficiency as receptor surface density increased, the intercept of the curve was higher than for untreated cells. This suggests that DG-hCG treatment suppresses oligomerization.

Table 4: Slope and intercept values for plots of FRET efficiency versus initial intensity, which is proportional to receptor surface density, graphs. CHO hLHR-eYFP cells were untreated and treated with 100 nM hCG and DG-hCG. Data shown are ± standard deviation.

Cell type	Treatment (100 nM)	number of cells examined	Intercept (%)	Slope
Control	None	67	-13±3	$5.0 \times 10^{-4} \pm 3.8 \times 10^{-5}$
CHO hLHR-eYFP	hCG	37	-17±4	$5.4 \times 10^{-4} \pm 4.3 \times 10^{-5}$
CHO hLHR-eYFP	DG-hCG	46	1±5	$2.1 \times 10^{-4} \pm 7.0 \times 10^{-5}$

showed increased FRET efficiency as a function of surface density, this indicates that hLHR expression levels affect the FRET phenomenon. When cells were treated with 100 nM DG-hCG, a hormone that inhibits receptor activity, a similar increase in FRET efficiency with surface density was observed (see Figure 33). However, compared to the control cells and hCG treated cells, the slope of the FRET efficiency versus initial intensity plot for DG-hCG-treated cells is less than both, reflecting generally lower concentration-dependence of FRET for all DG-hCG cells examined.

The fact that FRET efficiency on individual cells increases with initial fluorescence intensity, proportional to cell's receptor surface density, could be consistent with proximity-induced FRET arising from molecular crowding or with very weak specific receptor association. The latter phenomenon would occur if the receptor association constant K_a was low so that the extent of association increased as over the range of surface concentration explored. However, this sort of concentration-dependent specific association for GPCR has not been reported previously. Hence, it seems most logical first to consider the concentration dependence of FRET as possibly arising from concentration induced molecular proximity. However, the question of whether the actual surface concentrations reached in our cells and the fundamental physics of surface concentration-induced FRET could explain the observed concentration-dependent FRET remains to be addressed.

Transiently transfected cells exhibit a broad range of LHR expression

The range of receptor expression levels in transiently transfected cells was evaluated. Additionally, the number of receptors was in strongly-expressing cells was identified. Flow cytometry experiments yielding number of cells having particular fluorescence intensities were employed. The cells are hydrodynamically focused into a stream consisting of 1xPBS and one cell at a time passes through a 488 nm laser for eYFP excitation. An avalanche photodiode detector (APD) is placed along the laser excitation beam axis to collect forward scatter, light reflected from the cell in the forward direction relative to laser position. Forward scatter indicates cell size because magnitude of scatter is proportional to cell size. The second APD is placed 90° to the laser path to collect side scatter, light reflected at a larger angle relative to the cell. Side scatter indicates cell internal complexity because the light is reflected from the intracellular components. Fluorescence emission travels along the same path of side scatter then dichroic mirrors direct the light from eYFP to a PMT where fluorescence is collected. Fluorescence intensity was collected for Quantum FITC bead standards, three CHO cell populations each separately transiently transfected with hLHR-eYFP and an untransfected CHO cell population. All cells were maintained at 5% CO_2 and 37°C until prepared for the cytometer.

Flow cytometry yields histograms of numbers of cells versus log fluorescence intensity. Histograms of control and transfected cells are placed on a comparable basis by adjusting the amplitude and x-scale of the control cell histogram until the left half of the

control cell and transfected cell peaks optimally align (Figure 34). Then the adjusted control cell histogram is subtracted from that of the transfected cells to obtain an approximate histogram of successful transfected cells only. This histogram of the logarithms of fluorescence intensities can then be converted to linear intensities. A calibration curve of intensity measured in the cytometer versus number of FITC per bead was obtained using Quantum FITC bead standards. Using the equation for this line, FITC numbers per cell were calculated. Finally, using Equation 21, eYFP per FITC was calculated.

Flow cytometry was performed on four cell populations, three transfected with hLHR-eYFP and one untransfected population. Figure 35 shows the number of cells versus intensity for the three transfected cell populations with the untransfected population. Each transfected population has a different range of cells expressing hLHR with the second trial YFP 2 having the highest rate of transfection. We focus our subsequent attention on this second trial. Figure 34 shows the adjusted control untransfected cell histogram and the transfected cell population for the second trial. The transfected cell population histogram of the second trial with adjusted untransfected cell histogram subtracted is shown in Figure 36. The receptor numbers for the averaged transfected cell populations were calculated using a calibration curve (Figure 37) relating actual numbers of FITC in calibration beads to apparent numbers of FITC measured cytometrically using Quantum FITC bead standards. Numbers of hLHR-eYFP per cell were obtained by multiplying the apparent number of FITC per cell by 2.0 (Table 1). Figure 38 shows the average of the trials using the untransfected population used as the

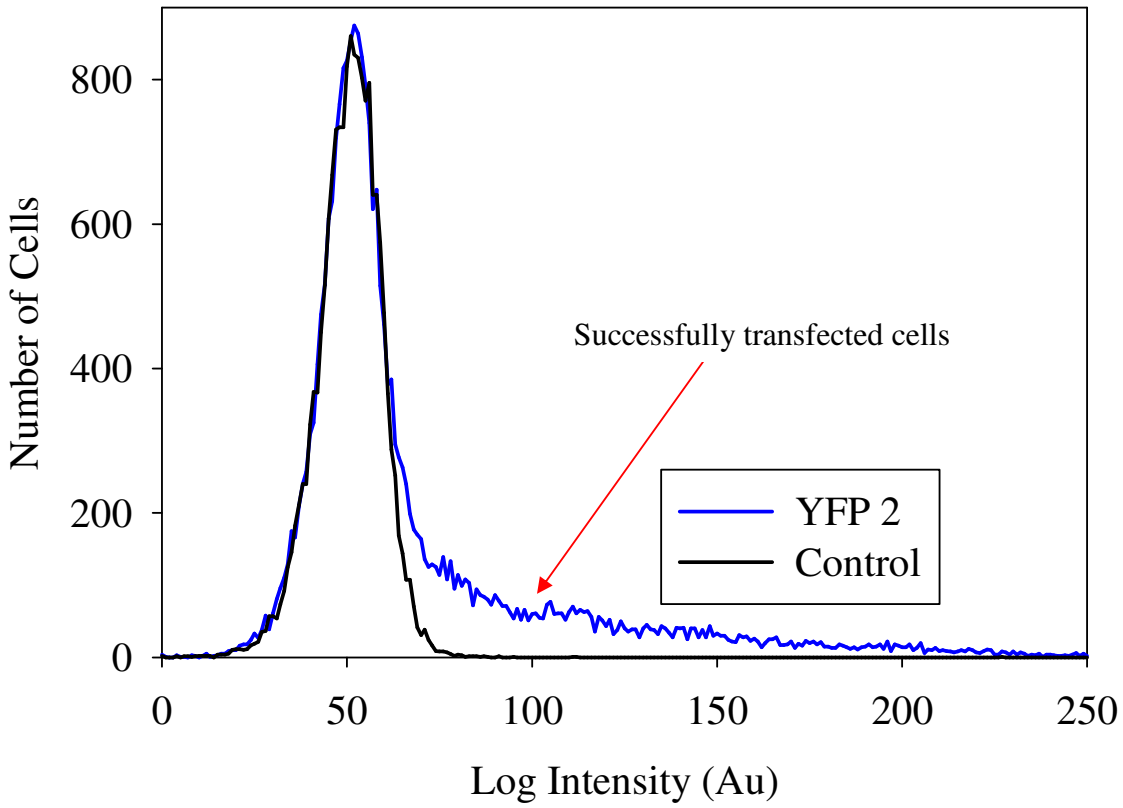

Figure 34: Flow cytometry histograms for trial 2 of CHO hLHR-eYFP compared with an untransfected population of CHO cells. The histograms were adjusted by optimally aligning the left halves of the amplitude and x-scale of both peaks.

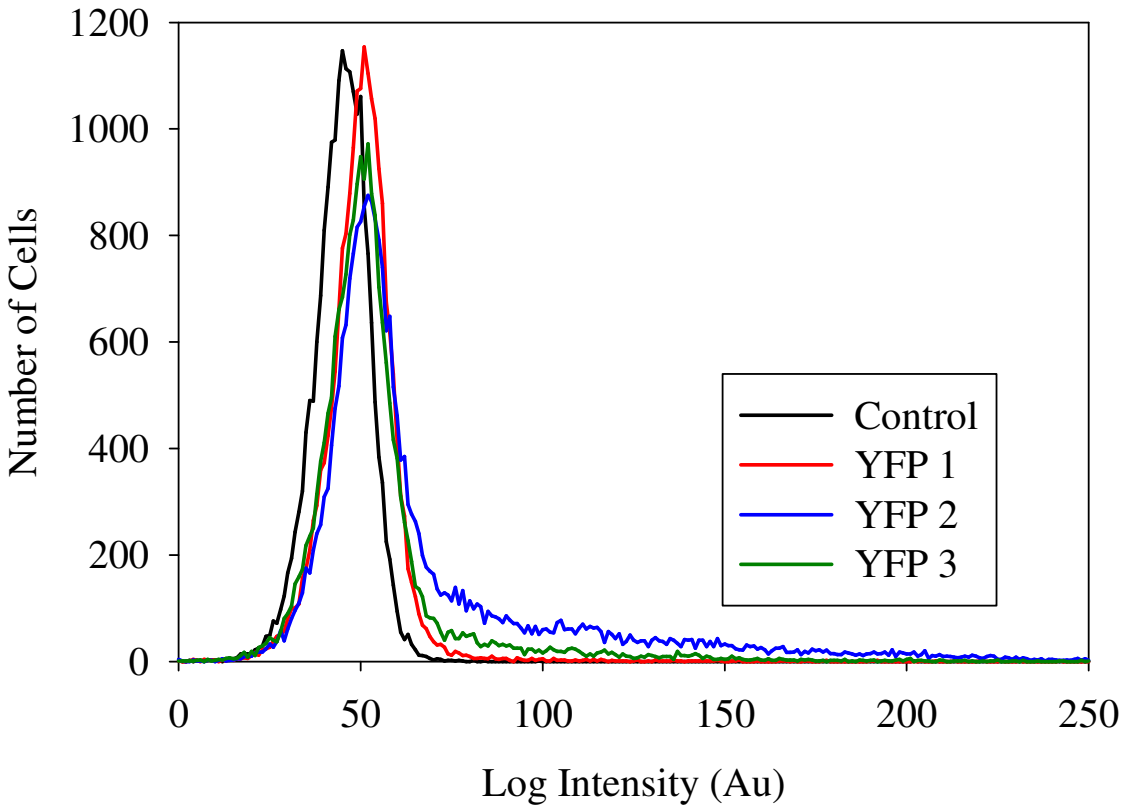

Figure 35**:** Flow cytometry histograms for three transfected populations YFP 1, YFP 2 and YFP 3 of CHO hLHR-eYFP. Different receptor expression levels are indicated by fluorescent intensity which was digitized in the cytometer on a scale of 0-255 arbitrary units. The second trial YFP 2 has the highest transfection efficiency.

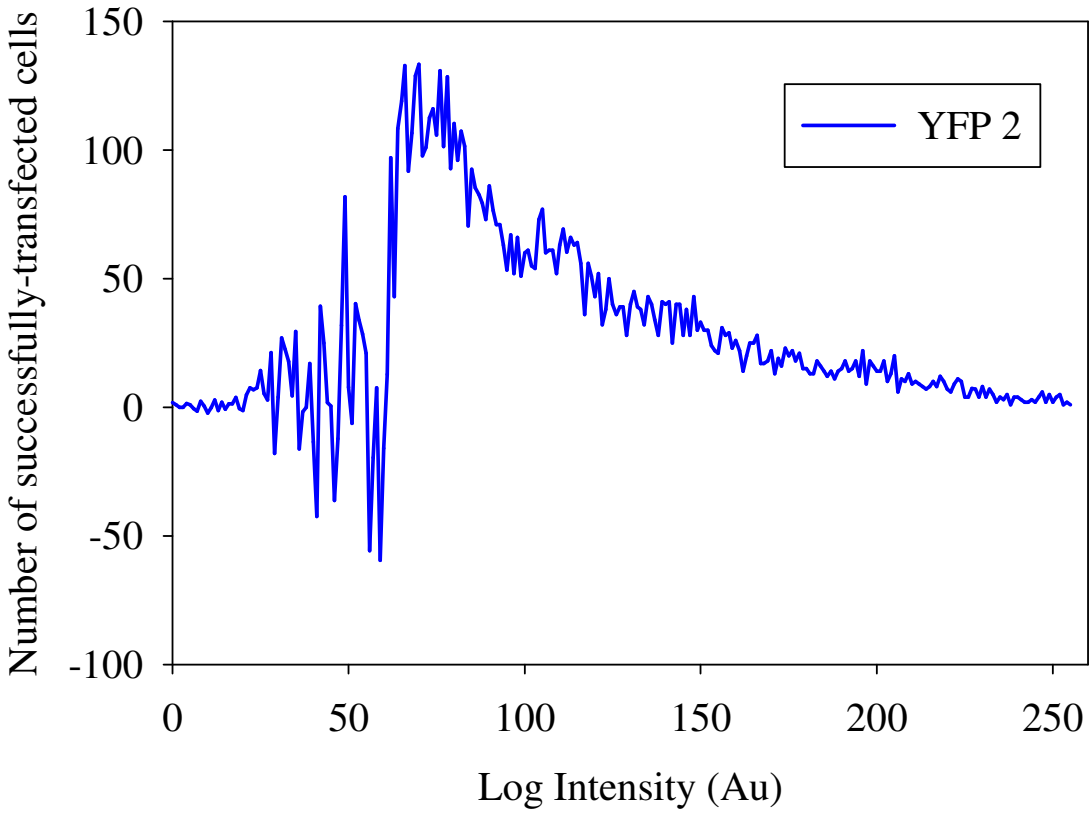

Figure 36: Transfected cell population histogram of the second trial with adjusted untransfected cell histogram subtracted.

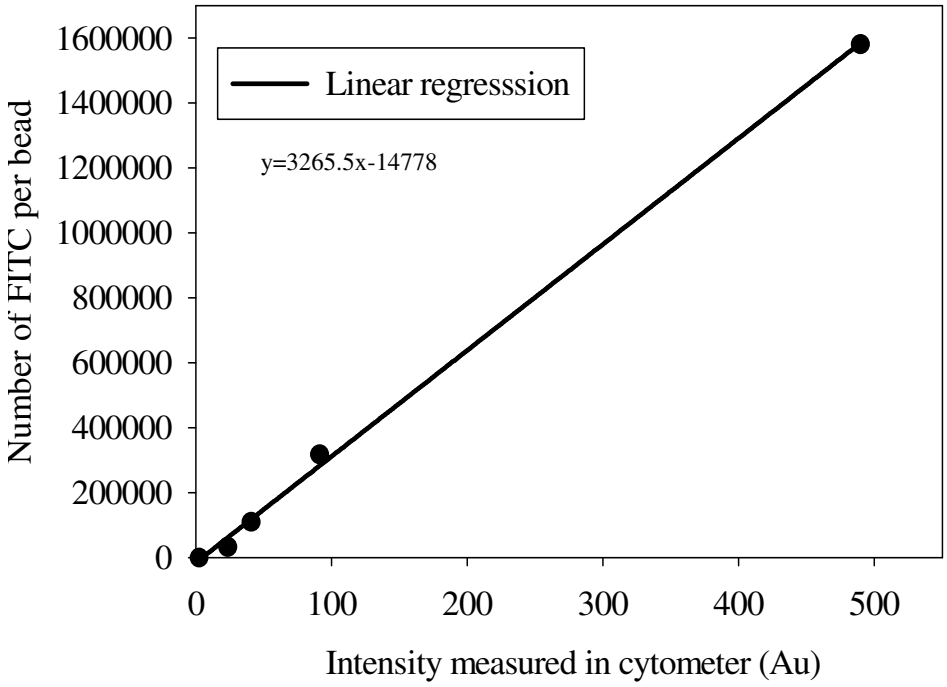

Figure 37: Calibration curve relating actual numbers of fluorescein isothiocyanate [31] in Quantum FITC bead standards to intensity measured in the flow cytometer.

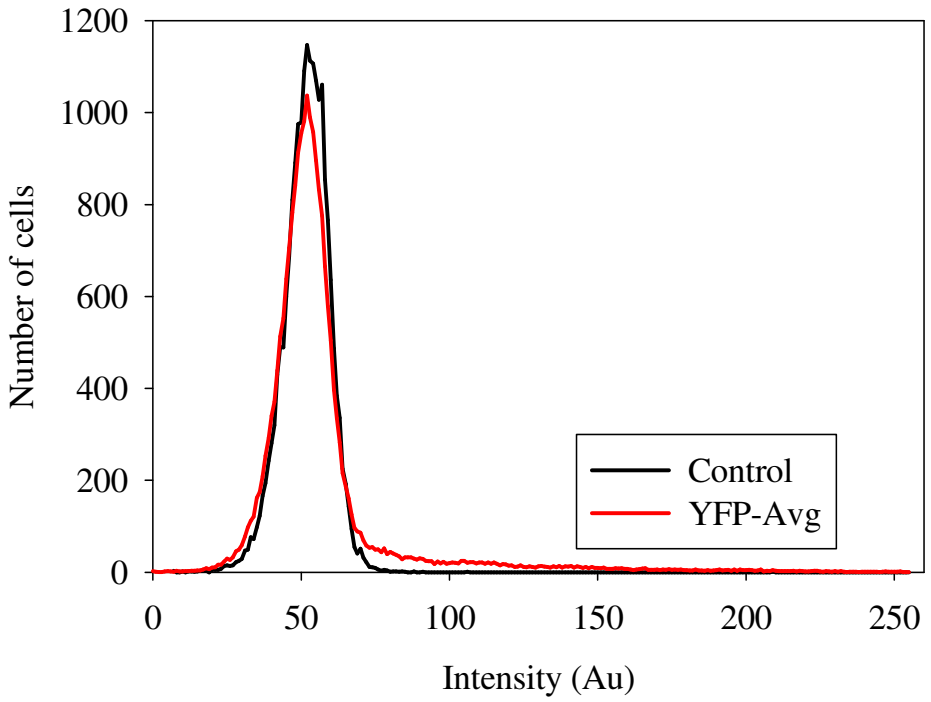

Figure 38: Average of flow cytometry measurements on transfected cells trials compared with an untransfected population. The mode of the difference between transfected and control cells occurs at about channel 80, which corresponds to an intensity of about 18, about 59,000 FITC, and about 118,000 eYFP.

control. A mode was most prominent in transfection 2 (see Figure 36) at approximately channel 80. At channel 80, the intensity measured in the cytometer is ~18 which yields a FITC signal of ~59,000 and thus eYFP signal of ~118,000. Therefore, the mode was 118,000 receptors per cell. However, it is obvious that many cells with much higher expressions exist in the population. This can also be seen in the averaged data for the three transfections (Figure 38). The apparent transfection efficiency is approximately 25%, approximately 7,400 cells after untransfected cell subtraction, out of a total of approximately 24,000 total cells.

Apparent FRET can arise from molecular crowding possibly on transiently transfected cells

FRET occurs when proteins of interest approach each other closely. Here FRET can also arise from proximity induced by high concentrations, as well as from specific molecular association. Therefore, using homo-FRET hLHR-eYFP numbers measured in transiently transfected CHO cells, calculations were performed to determine if a substantial amount of apparent FRET/BRET has arisen from molecular crowding. Additionally, the possibility that if hLHR-eYFP in lipid rafts affects the apparent FRET/BRET phenomenon was considered

To calculate the probability of FRET that will arise from molecular crowding, the probability of no FRET $P_{no}(r)$ for a molecule in a differential area of $2\pi r\, dr$ around

some excited molecule has to be considered, Figure 39. Probability of no FRET is given by Equation 23

$$P_{no}(r) = 1 - \left(\text{probability of a molecule in that area}\right) \left(\text{probability of FRET to that molecule}\right) \tag{23}$$

Since the differential dr is small, Taylor series expansion of ln P_{no} (r) yields Equation 24, which depends on the inverse sixth power of the distance between donor and acceptor

$$\ln P_{no}(r) = -\frac{2\pi\ r}{1+\left(r/r_0\right)^6}\sigma\ dr \tag{24}$$

where σ is surface density, r is distance between fluorophores and r_o (Förster distance) is the distance at which energy transfer efficiency is 50%. The probability of no FRET to any acceptor is obtained by Equation 25

$$\ln P_{no} = -2\pi\sigma \int_{r=0}^{\infty} \frac{rdr}{1+\left(r/r_0\right)^6} \tag{25}$$

Making the substitution $z=(r/r_0)^2$, yields the simplified Equation 26

$$\ln P_{no} = -\pi\sigma\ r_0^{\,2} \int_{r=0}^{\infty} \frac{dz}{1+z^3} \tag{26}$$

and, when integrated, Equation 27 is obtained.

$$\ln P_{no} = -\frac{2\pi^2\sigma\ r_0^{\,2}}{3\sqrt{3}} \tag{27}$$

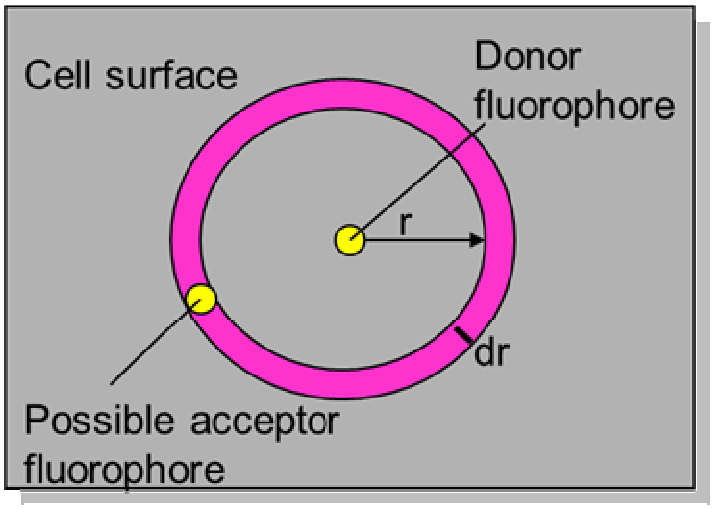

Figure 39: The probability P_{no} (r) of no FRET from an excited molecule surrounded by possible acceptors in a differential area $2\pi r\, dr$.

and the probability of FRET to some acceptor is Equation 28.

$$P_{FRET} = 1 - e^{-\frac{2\pi^2 \sigma \, r_0^2}{3\sqrt{3}}} \tag{28}$$

Equation 28 simplifies to Equation 29.

$$P_{FRET} = 1 - e^{-3.799 \sigma \, r_0^2} \tag{29}$$

where σ is the receptor surface density in receptors per μm^2 and r_0 is the Förster distance in nm.

Using Equation 29, Figure 40 was created for fluorophores with Förster distances of 4.5, 6.0, and 7.5 nm. These numbers bracket the range of Förster distance values for commonly-used donor acceptor pairs. In Figure 40, as local receptor concentration increases so does apparent FRET efficiency. With a 1100 μm^2 cell surface area, 5.11 nm Förster distance for YFP, and assuming the hLHR is uniformly distributed over the cell membrane, the apparent FRET efficiency for a 118,000 total receptors where the mode appears in Figure 36 is 1%. For a similar cell with 400,000 receptors, the apparent FRET efficiency is 4%. FRET efficiencies of 5% or greater are often considered significant [105] but the possible presence of the receptors in lipid rafts, also has to be considered. If these receptors are concentrated into lipid rafts, their local concentration will be higher than receptors uniformly distributed over the cell membrane. Previous data have shown LHR to be associated with lipid rafts [58, 106]. For the cell membrane area fraction that is covered with lipid rafts, while percent coverage is not directly measureable, 10% can

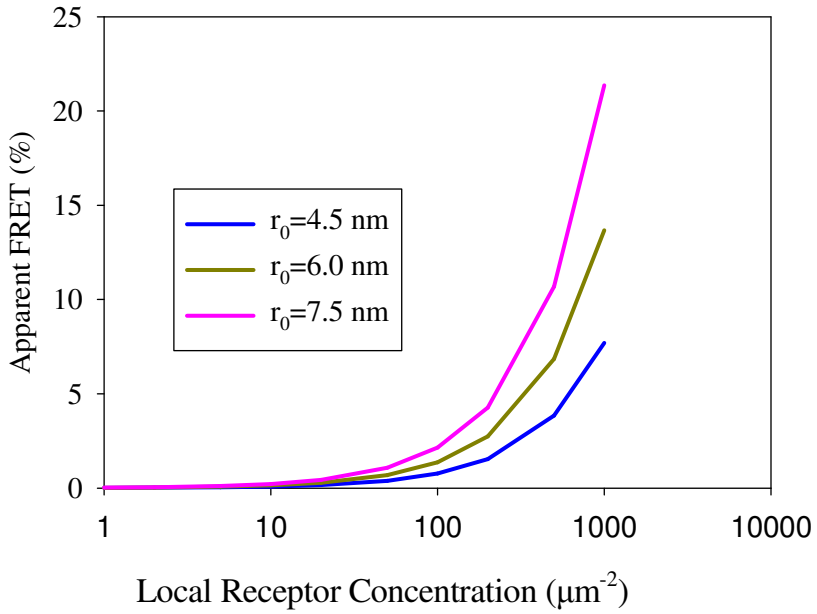

Figure 40: For fluorophores with Förster distances of 4.5, 6.0 and 7.5 nm, apparent FRET efficiencies were graphed as a function of local receptor surface concentration. These numbers bracket the range of Förster distance values. As local receptor concentration increases so does FRET efficiency.

be a typical estimate suggested by other investigators [102, 107]. For a CHO cells with a 1100 μm^{-2} surface area where receptors were uniformly distributed and localized in lipid rafts covering 10% of the plasma membrane, local receptor concentration would increase from 109 μm^{-2} in the absence of rafts to 1090 μm^{-2}. Therefore, for 118,000 receptors apparent FRET efficiency would be 10% and, for 400,000 receptors, 30%. Therefore, if most receptors are actually localized in lipid rafts, then most if not all of the FRET levels typically observed without hormone could be attributed to molecular crowding.

Since hLHR-eYFP was expressed by transient transfection, the receptors maybe experiencing molecular crowding phenomenon from high hLHR expression levels. The decreasing trend of initial anisotropy as surface density increases, seen in Figures 28-30, may be arising from proximity. As stated earlier, aggregate size lowers anisotropy. If there is molecular crowding, anisotropy will decrease due to proximity of nearby fluorophores. Therefore, this may further support that there is molecular crowding attributed from high expression levels in CHO cells transiently transfected with hLHR.

Homo-FRET reveals constitutive association of MHC class II molecules

A further demonstration that homo-FRET is valuable in evaluating self-association of other biological systems comes from raw homo-FRET data concerning three different types of MHC class II receptors on M12.C3 B lymphoma cells obtained by Dr. Jun Zhou and subsequently analyzed by this author. The M12.C3 B lymphoma cells contain endogenous MHC class II receptors. The M13C3.F6(αwt/βwt) cells contain fully

functional receptors. The M13C3.402(α-12/β-18) cells express the inactive form of MHC class II receptors because it is fully truncated. The M13C3.43.28.2(Dα185K/Rβ106E) cells express the partially active MHC class II receptors. Homo-FRET data were obtained for each cell type with no treatment to determine if MHC class II molecules exist as constitutive homodimers. Homo-FRET data were obtained on cells treated with 20 μg/mL of 10.2.16 mouse anti-A_{β}^{k} monoclonal antibody (mAb), to determine if crosslinking the receptor increases oligomerization. Homo-FRET data were also obtained in cells treated with 1 mM dibutyryl-cAMP (db-cAMP), which activates cAMP-dependent protein kinases in the receptor. Finally, homo-FRET data were obtained on cells treated with 1% (w/v) methyl-β-cycledextrin (MβCD) which depletes cells of cholesterol, a required component of lipid rafts. Decreasing raft formation may decrease oligomerization since rafts are known signaling platforms for MHC molecules.

Major Histocompatibility Complex class II molecules were labeled with Alexa 488 conjugated to hen egg lysozyme (Alexa 488-HEL). HEL is a peptide recognized by the MHC class II receptor. The cell lines were cultured for three days with 10 μM of Alexa 488-HEL where MHC class II receptors present Alexa 488-HEL on the cell surface. The homo-FRET data were collected on the FV300 confocal laser scanning microscope using a 488 nm argon ion laser to bleach the cells to ~1% of initial fluorescence within approximately 20 images. Dr. Jun Zhou collected homo-FRET data and produced plots of average intensity versus image frame and anisotropy upon photobleaching versus image frame as cells are irreversibly photobleached graphs. These data were subsequently analyzed for this study using Sigma Plot 11.0. Graphs of

anisotropy versus fraction of fluorescence intensity were then created and subjected to quadratic least squares analysis according to Equation 30

$$r = r_0 + ax + bx^2 \tag{30}$$

where r is anisotropy, r_0 is the anisotropy of one fluorophore with no depolarization, i.e. when fractional intensity is zero, a is the slope of the plot of anisotropy versus fractional fluorescence, x is the fractional fluorescence and b is the graph curvature term. The sum of r_0+a+b is the initial anisotropy that is when the fractional intensity is one. Using Equation 31, homo-FRET efficiency E% can be calculated.

$$E\% = -(a+b)/r_0 \; x \; 100 \tag{31}$$

Figure 41a shows confocal images obtained by Dr. Jun Zhou of a M13C3.F6 cell with endogenous MHC class II receptors binding HEL peptide conjugated to Alexa 488 with no treatment as the peptide is irreversibly photobleached. Figure 41b is the corresponding average fluorescence intensity and anisotropy upon photobleaching versus image frame number that shows at the peptide is irreversibly photobleached, its anisotropy increases. This is because, as photobleaching occurs, the likelihood that two molecules in a dimer both remain unbleached decreases and so the ability to exhibit homo-FRET decreases. This is because the overall distance between the fluorophores is increasing. Figure 41a-b represents confocal images of an M13C3.F6 cell binding HEL peptide conjugated to Alexa 488 photobleached over time. Figure 42 shows anisotropy upon photobleaching versus fraction of intensity for a single cell with accompanying quadratic least squares fitted line. Table 5 summarizes initial anisotropies r_0, a values, the slope of the plot of anisotropy versus fractional fluorescence, b values, the graph curvature term and FRET efficiencies. For untreated M13C3.F6 cells, FRET efficiencies averaged 55±9%. Since

a.

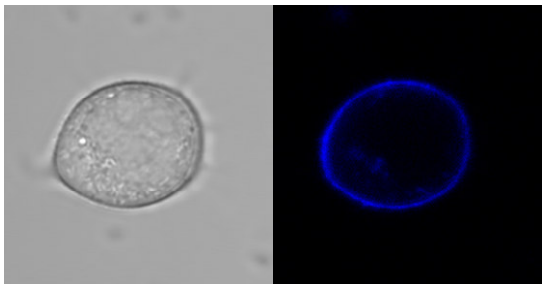

b.

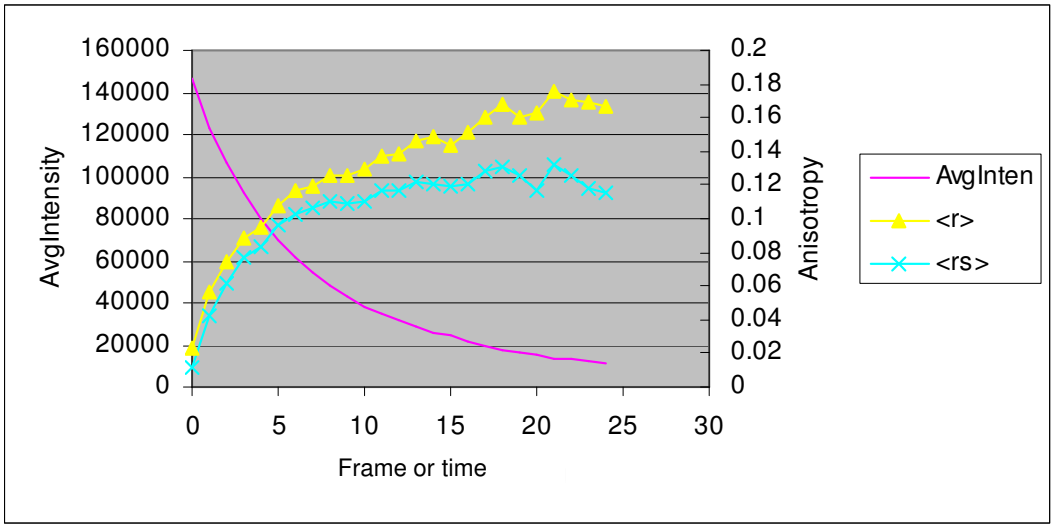

Figure 41: (a) Confocal images of untreated M13C3.F6 cell binding HEL peptide conjugated to Alexa 488 as the fluorescent peptide is irreversibly photobleached. (b) Plot of the cell's average fluorescence intensity and anisotropy upon photobleaching versus image frame number showing anisotropy increase as fluorescence is bleached away.
*Data obtained by Dr. Jun Zhou

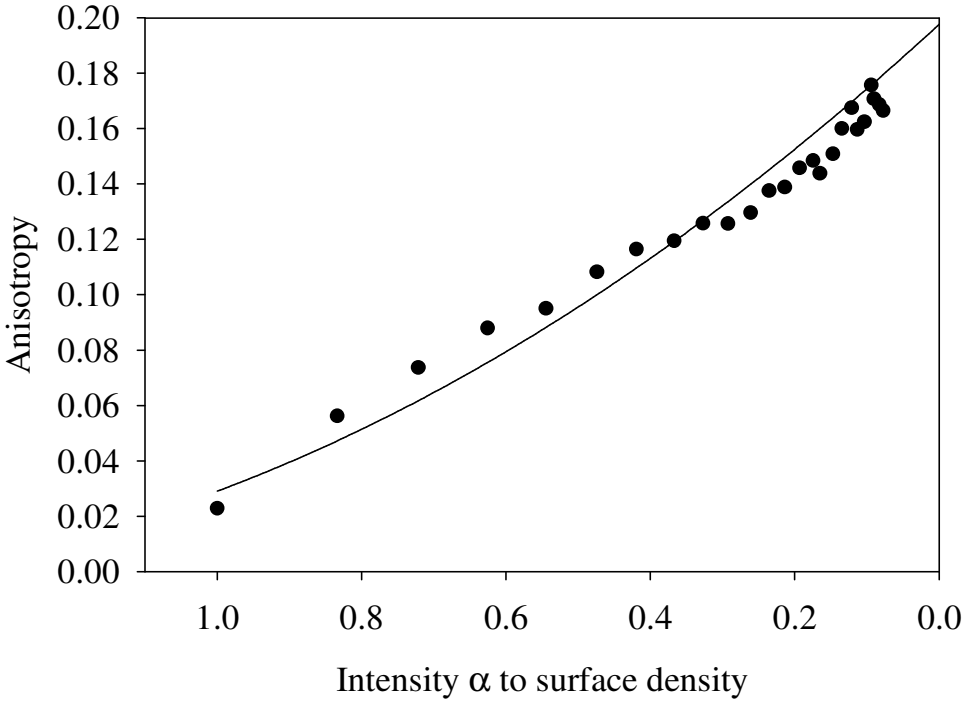

Figure 42: Anisotropy upon photobleaching versus fractional intensity for MHC class II molecules binding Alexa 488-HEL for a M12C3.F6 cell with quadratic least squares fitting. Smooth curve represents Equation 29 fitted to experimental data.

Table 5: Summary of initial anisotropies r_0, a values, the slope of the plot of anisotropy versus fractional fluorescence, b values, the graph curvature term and FRET efficiencies between peptides bound to I-Ak MHC class II molecules on M12.C3 B. lymphoma cells. Data shown are the mean ± standard deviation.

Clone and I-A phenotype	F6(wt/wt)	402(α-18/β-18)	43.28.2(Dα185K/Rβ106E)
Mean Ag presentation	Normal	Inactive	Partial/rescuable
None			
r_0	0.17±0.06	$0.20\pm4.6\times10^{-3}$	0.16±0.03
a	-0.16±0.20	-0.33±0.01	-0.18±0.11
b	0.05±0.14	0.22±0.01	0.06±0.08
E%	55±9	55±1	77±9
n[1]	7	3	7
MβCD			
r_0	0.20±0.03	0.19±0.02	0.21±0.03
a	-0.26±0.09	-0.28±0.09	-0.31±0.12
b	0.11±0.09	0.18±0.08	0.16±0.11
E%	77±5	52±2	59± 14
n[1]	5	3	4
10.2.16 mAb			
r_0	0.21±0.01	0.22±.01	0.29±0.04
a	-0.27±0.07	-0.38±0.065	-0.55±0.13
b	0.08±0.06	0.25±0.06	0.34±0.12
E%	89±4	56±1	72±4
n[1]	5	6	4
db-cAMP			
r_0	0.21±0.03	0.18±0.02	0.19±0.04
a	-0.27±0.05	-0.26±0.09	-0.30±0.16
b	0.11±0.04	0.17±0.06	0.16±0.15
E%	50±24	54±6	54± 22
n[1]	3	3	3

[1]n is number of cells examined for each specific treatment.

FRET values of 5% can be considered significant, this is a considerable amount of energy transfer showing that MHC class II molecules were oligomerized on M13C3.F6 cells.

When MβCD and 10.2.16 mAb (crosslinker) was used as treatment, FRET efficiency increased to 77±5% and 89±4%, respectively. MβCD might be expected to theoretically reduce efficiency because it dissipates lipid rafts. However, if MHC class II molecules interact strongly with other raft components, then a reduction in the number of lipid rafts might yield an increase in the MHC class II concentration in those rafts which remain. 10.2.16 mAb treatment should increase FRET because receptors are brought in close proximity by crosslinking, as is observed in F6 cells, though not on the other cell types. FRET between MCH class II molecules on cells where db-cAMP was used to activate cAMP-dependent protein kinases, compared to the cells not treated, remained the same within experimental error at 50±24%. M13C3.402 cells not treated revealed FRET efficiency of 55±1% which indicates MHC class II molecules oligomerized on the plasma membrane. The FRET efficiencies for MβCD, 10.2.16 mAb, and db-cAMP where all the same within experimental error compared to the cells not treated at 52±2%, 56±1% and 54±6%, respectively. This reveals that non-active MHC class II receptors remain aggregated on the plasma membrane. M13C3.43.28.2 cells expressing partially active MHC class II receptors had a FRET efficiency of 77±9% for cells not otherwise treated, again showing constitutive oligomerization of MHC class II molecules in the plasma membrane. Compared to the cells not treated, M13C3.43.28.2 cells treated with MβCD, 10.2.16 mAb, db-cAMP revealed FRET efficiencies of 59±14%, 72±4% and 54±22%, respectively which are within experimental error. Overall, for the three different cell

types and treatments, substantial degrees of constitutive dimerization were shown for MHC class II molecules binding the 488-conjugated peptide HEL.

DISCUSSION

The data demonstrate, first, that hLHRs appear in close proximity in untreated living cells since FRET efficiencies of 23% are observed on control cells. hCG treatment caused an increase in FRET efficiency compared to the already significant FRET values observed for untreated cells. This result supports the notion that hLHR form aggregates when liganded [60, 108]. This could also have arisen from hCG activating the receptor, causing it to migrate into lipid rafts and form larger oligomers [108]. When treated with the antagonist DG-hCG, there was a significant decrease in FRET efficiency compared to the control. These data show that antagonist treatment does reduce affect self-association of hLHR.

However, expression levels of hLHR have a significant effect on receptor association. For hCG and DG-hCG-treated cells and untreated cells, Figures 31-33 show that, as receptor as receptor surface density increases, FRET efficiency increases as well. Flow cytometry shows that hLHR-eYFP transiently transfected into cells exhibit a broad range of expression levels, with most cells having receptor numbers of 118,000 per cell but with many much more highly-expressed cells being present. Compared to endogenous receptor levels of 20,000 to 40,000 per cell, hLHR-eYFP transfected into CHO cells are highly expressed. The high FRET efficiencies, in conjunction with high

hLHR expression levels, suggest that observed apparent FRET arose not only from molecular crowding but also from self-association. The FRET efficiency values for cells treated with DG-hCG were significant, even though reduced relative to control cells. Thus, it is likely that FRET in these cells arises both from specific receptor aggregation and from non-specific effects of high receptor surface density. The data clearly show that the oligomerization of hLHR is density-dependent. To support this, Figures 28-30 show the extent of oligomerization for transiently transfected hLHR as initial anisotropy is plotted as a function of receptor surface density. Such behavior has been observed previously. For example, Gerritsen and co-workers [109] also found that fluorescence anisotropy upon photobleaching of clustered receptors decreases with increasing cluster size. Given those observations, study of a cell line more closely resembling naturally expressing receptors [61] would lead to a better understanding of the signal transduction pathway of LHR. Additionally, lower FRET efficiencies on untreated cells would be observed because receptor molecular crowding would be eliminated.

Finally, MHC class II molecules examined by homo-FRET show that this technique can be used as a general tool to assess self-association of other biological systems. This approach has shown here that active, inactive and partially active MHC class II molecules are constitutively dimerized on cells treated with MβCD, a crosslinker and db-cAMP, as well as on control cells. These data are summarized in Table 5.

Past experiments by Roess and co-workers suggest that LHR self-associates in the plasma membrane after ligand treatment [18, 58, 60, 63-66, 106]. FRAP experiments

showed that, for endogenous LHR, lateral diffusion coefficients and recovery percentages decreased upon treatment with fluorescently-labeled LH. Moreover hCG bound to LHR was laterally immobile on luteal cells, suggesting hCG-binding LHR exist as large oligomers [62, 110-112]. Time-resolved phosphorescence anisotropy (TPA), a technique that measures rotational correlation times, was used to show that liganded LHR had long rotational correlation times, suggesting receptor presence in large aggregates [18, 65]. LH and hCG were fluorescently labeled with erythrosin isothiocyanate (ErITC). A non-functional LHR mutant (LHR K583R) exhibited decreased rotational correlation times compared to functional LHR. DG-hCG treatment decreased rotational correlation times for both wild type and mutant receptors. TPA measurements on cells treated with cytochalasin D, which disrupts actin filaments in cells, showed significantly shorter rotational correlation times, indicating that LHR interacts with the cytoskeleton [18]. The data shown in this dissertation supports the notion that hLHR forms oligomers with hormone treatment. CHO cells transiently transfected to express hLHR-eYFP exhibited FRET values ranging from 23% for unliganded receptors to 28% for liganded receptors. Additionally, when FRET efficiencies are plotted as a function of receptor surface density, slope values become steep from $5.0x10^{-4}\pm3.8x10^{-5}$ for untreated cells to $5.4x10^{-4}\pm4.3x10^{-5}$ for hCG-treated cells further supporting that hCG promotes aggregation of LHR.

Interference fringe FPR, a technique by which diffusion information can be gathered from an entire cell, has been applied to the study of LHR diffusion by Roess and co-workers [66]. When LHR was liganded with LH or hCG, receptor fractional mobilities

were calculated to be 25% lower than the fractional mobility of the non-functional receptor, LHR-K583R. This suggested that aggregates of increased molecular size exhibit lower lateral diffusion. Hetero-FRET was used to determine self-association of LHR. LHR were labeled with mixtures of FITC-LH/tetramethylrhodamine isothiocyanate-LH (TRITC-LH) or FITC-hCG/TRITC-hCG. FRET values of ~13% and ~17% for LH and hCG treated cells, respectively, were observed. However, a control to test possible FRET between unliganded receptors could not be used because there was no suitable florescence label for endogenous hLHR. Later, hetero-FRET data for LHR fused to CFP and YFP stably co-transfected into cells revealed self-association showing FRET values ranging from 0% for unliganded receptors to 18% when liganded [60]. Compared to the data shown in this dissertation, transiently transfected hLHR-eYFP showed FRET values ranging from 23% for unliganded receptors to 28% for liganded receptors. This further supports the notion that transiently transfected hLHR show apparent oligomerization which actually arises from molecular crowding. The stably transfected cells for LHR fused to CFP and YFP mentioned above show 0% FRET unliganded receptors, supporting that a stable cell line expressing physiologically-realistic levels of receptors will not show apparent constitutive FRET.

To evaluate possible association of LHR with lipid rafts, Roess and co-workers [106] employed isopycnic density gradient ultracentrifugation. For hCG-treated cells, rat LHR (rLHR) banded in low density sucrose fractions compared to rLHR not treated with hormone. This indicates that rLHR is associated with lipid rafts, since rafts are buoyant and appear in low density gradient fractions [113]. Single particle tracking was

performed on rLHR-FLAG, in which FLAG is an epitope tag, stably transfected into CHO cells. These experiments revealed that rLHR treated with hCG is confined in smaller membrane compartments than is untreated rLHR [106]. This, together with results of density gradient studies, suggests that rLHR partitions into lipid rafts with restricted motion within the raft [106]. DG-hCG treatment, and 1% MβCD significantly increased compartment size accessed by rLHR. This would be consistent with LHR partitioning into lipid rafts when liganded for receptor aggregation. The data shown in this dissertation show that, upon hCG treatment, the changes in anisotropy upon photobleaching, were 0.081±0.006 for untreated cells and 0.099±0.010 for hCG-treated cells. This supports the notion that hCG promotes self-association; hence it is likely hLHR partitions into lipid rafts. Upon DG-hCG treatment, the hLHR anisotropy change upon photobleaching of 0.058±0.006 was smaller than that of the untreated cells with a value of 0.081±0.006. This shows that DG-hCG treatment suppresses oligomerization and may inhibit hLHR partitioning into lipid rafts.

Roess and co-workers [106] examined three constitutively active hLHR mutants by hetero-FRET to investigate possible self-association, as was observed for hLHR-wt [58]. For the three mutants and hLHR-wt, CFP- and YFP-fusion proteins were created and stably transfected into CHO cells. For all three mutants, liganded receptors showed FRET values ranging from 11-15% the same within experimental error as the untreated mutants. SPT and isopycnic ultracentrifugation were also performed, though only the mutant, LHR-D578H, was examined [58]. SPT showed a much smaller compartment size compared to hLHR-wt and the compartment size decreased even more upon hCG

treatment. Isopycnic ultracentrifugation revealed there was a moderate shift of hLHR to lower sucrose density fractions after hCG treatment. When cells were treated with MβCD, there was shift towards the higher density fractions when compared to untreated LHR-D578H.

For all the constitutively active mutants, FRET values were significant for both untreated and hCG-treated cells. Since wild-type LHRs are not constitutively active and exhibit FRET values of 0% for unliganded receptors and 12% for liganded receptors, the FRET observed in this dissertation must arise primarily from molecular crowding on the transiently transfected hLHR-eYFP CHO cells examined. The FRET values for hLHR-eYFP observed in this dissertation are comparable to those of the constitutively active hLHR mutants. When the three mutants were treated with hCG, FRET values remained the same within experimental error while the hLHR-wt exhibited a significant increase. Transiently transfected cells examined in this study showed an increase in FRET values upon hCG treatment. This further supports that hCG promotes aggregation of hLHR and that aggregates likely partition into lipid rafts upon hormone treatment as Roess and co-workers observe in their SPT and isopycnic ultracentrifugation studies. In addition, these data support the notion that receptor level affects hLHR self-association. The transiently transfected hLHR-eYFP that exhibit a broad range of receptor numbers show FRET values of 19% for untreated cells and the stable line mentioned above show FRET values for 0%. Thus FRET values observed in the present study most likely arise from high receptor surface densities, i.e., molecular crowding.

Segaloff and co-workers [67] reported BRET^2 studies suggesting that hLHRs are constitutively oligomerized on the plasma membrane. However, this contradicts their previously reported co-immunoprecipitation data showing that stably-transfected cells exhibit an increase in oligomerization upon treatment with increasing hCG concentrations [61]. The co-immunoprecipitation data suggest that hLHR aggregates upon hCG treatment. The discrepancy between their previous and current data is likely due to transient transfections used to produce LHR-expressing cells for BRET studies. In these BRET^2 studies, receptor number per cell was not reported. Human embryonic kidney (HEK) 293t cells were transiently co-transfected with GFP^2-hLHR and Rluc-hLHR. In addition, cell lysates instead of live cells were used for the majority of their experiments. BRET^2 ratios (light emitted by GFP^2 divided by that produced by chemoluminescence of Rluc) was plotted as a function GFP^2:Rluc expression where GFP^2 increased in concentration as Rluc expression was held consent. These plots for cell lysates were the same within experimental error as those for hCG treated cells, suggesting hLHR does not aggregate when liganded. BRET^2 ratios were also graphed as a function of density of sucrose fractions in isopycnic ultracentrifugation to determine possible association of LHR with lipid rafts. Again, cells lysed and treated with buffer and hCG gave BRET^2 ratios ranging from 0.2 to 0.3 within experimental error. B_{50} values, explained earlier in background, were calculated for hLHR-wt and hLHR for mutants such as M398T, T577I, L457R and D578Y. These results showed that hLHR-wt exhibited B_{50} values comparable to the constitutively-active mutants, suggesting that hLHR-wt is also constitutively aggregated. However, there needs to be a comparison of B_{50} values for hLHR wt and the mutants, all after hCG treatment, to confirm these results. Since transient transfections

were used and since the number of expressed receptors was not reported, it seems possible the apparent constitutive oligomerization of hLHR these authors observed is in fact attributable to molecular crowding as shown here in this dissertation. We show that cells transiently transfected with hLHR-eYFP exhibit apparent constitutive FRET and that hCG promotes self-association. Moreover, the use of cell lysates cannot provide unambiguous data if the number of cells lysed per well in the microplate luminometer is not reported because more lysates per well can exhibit stronger BRET signals. Since receptors per well can vary considerably, this further supports the supposition that the $BRET^2$ signal most likely arose from molecular crowding. We show in our data that FRET between hLHR is surface density-dependent. When FRET efficiency was plotted as a function of receptor surface density for hLHR-eYFP, FRET values increased with increasing receptor surface density. Our observations from homo-FRET with transiently transfected cells supports Segaloff and co-workers' co-immunoprecipitation findings from their 2004 publication [61] that hLHR may exist as oligomers prior to agonist treatment and further increase with hCG treatment, since here in their current publication transiently transfected cells using RET are difficult to interpret. In addition, homo-FRET only requires one fluorophore. Therefore, the donor/acceptor ratio does not affect FRET efficiencies. In contrast, hetero-FRET is dependent on the environment of the donor fluorophore because it transfers energy. As we observe in this dissertation, transiently transfected cells do not take up DNA at the same ratio for each cell. Thus, achieving a donor to acceptor of 1:1 is very difficult. Low donor to acceptor ratios are commonly used, so that apparent FRET does not depend on donor concentration. Having more

acceptor fluorophores than donor fluorophores allows for one donor fluorophore to transfer to multiple acceptor fluorophores [105].

Clayton and co-workers [23] performed steady-state homo-FRET experiments on a stable line of CHO cells expressing serotonin 1_A (5-HT_{1A}) receptor. An overall receptor concentration of 91/μm^2 was reported. They concluded that this receptor was pre-aggregated and that, upon treatment with agonist, additional oligomerization occurred.

Clayton et al. [23] treated cells transfected with 5-HT_{1A}-eYFP with the serotonin agonist, 4-(2´-methoxy)-phenyl-1-[2´-(N-2´´-pyridinyl)-*p*-iodobenzamido]ethyl-piperzine (*p*-MPPI) the antagonist, MβCD and CD. Untreated cells transfected with 5-HT_{1A}-eYFP served as the control. Upon serotonin and *p*-MPPI treatment, change in anisotropy upon photobleaching increased from 0.06 for the control to 0.09 for serotonin and decreased to 0.05 for *p*-MPPI antagonist. These results suggested receptor oligomerization upon agonist treatment and suppression of receptor aggregation by antagonist. The Authors plot anisotropy upon photobleaching versus initial fluorescence intensity, which is proportional to surface density, for cells treated with serotonin, *p*-MPPI, MβCD, cytochalasin D (CD) and untreated cells. They observe that anisotropy values for all treatments and untreated cells remained constant, showing that 5-HT_{1A}-eYFP aggregation of receptors is not affected by the various treatments and treating cells with these reagents does not change density.

Clayton et al. [23] also treated cells transfected with 5-HT_{1A}-eYFP with MβCD, which depletes cholesterol and destabilizes lipid rafts, and cytochalasin D which depolymerizes actin filaments of the cytoskeleton. The change in anisotropy upon photobleaching for MβCD was low with a value of 0.03 compared to untreated 5-HT_{1A}-eYFP which had a value of 0.06. These data suggest that MβCD treatment of 5-HT_{1A}-eYFP receptors results in decreased oligomerization and function of low-order oligomers upon MβCD treatment which may be associated with lipid rafts. With CD treatment, change in anisotropy upon photobleaching increased, suggesting that, upon CD treatment, 5-HT_{1A}-eYFP aggregates into high-order oligomers.

These workers [23] show there is constitutive oligomerization of 5-HT_{1A}-eYFP receptors and that the agonist serotonin and the antagonist *p*-MPPI increase and decrease aggregation, respectively. This was observed in our data for hLHR-eYFP transiently transfected into CHO cells. When hLHR was treated with hCG, FRET efficiencies and change in anisotropy upon photobleaching increased compared to untreated cells and upon DG-hCG treatment, FRET efficiencies and change in anisotropy upon photobleaching values decreased. These data show that hCG promotes aggregation and DG-hCG suppresses it. They show that, with a stably transfected cell line of 5-HT_{1A}-eYFP expressing 100,000 receptors, that receptor density does not affect anisotropy values. Conversely, we observe that as hLHR receptor density increased, FRET efficiencies increased as well. Since a stable cell line was used and anisotropy values are independent of concentration, it seems that the constitutive self-association of 5-HT_{1A}-eYFP does not arise from high receptor surface densities. However, we do observe

receptor density-dependent anisotropies and therefore the apparent self-association we observe could be attributable to molecular crowding.

Finally, Clayton and co-workers [23] also showed a difference in anisotropy changes upon photobleaching for MβCD-treated cells as compared with control cells. Anisotropy change upon photobleaching significantly decreased upon MβCD treatment, 5-HT_{1A}-eYFP suggesting the receptor may be in rafts. Therefore, the apparent FRET values reported in their study could also arise from proximity of 5-HT_{1A}-eYFP receptors. They also report that oligomerization of the receptor is not dependent on receptor expression level. They plotted initial anisotropy versus intensity range for 5-HT_{1A}-eYFP receptors and showed the intensity remained constant for all treatments and untreated cells for $1x10^{-4}$ to $4x10^{-4}$ AU. It could well be that receptor aggregation is dependent on receptor expression level, but that a lower expression level is needed to see this dependence.

Hofman and co-workers [114] stably transfected epidermal growth factor receptor fused to monomeric GFP (EGFR-mGFP) in NIH 3T3 cells at 50,000 receptors/cell. EGFR aids in the growth and development of cells. Using limiting anisotropy values determined by time-resolved homo-FRET, they found that there was constitutive oligomerization of EGFR-mGFP. Degrees of polarization of 0.93 for mGFP and 0.89 for EGFR-mGFP were observed, suggesting that 40% of EGFR-mGFP exist as oligomers prior to agonist treatment. For unliganded EGFR-mGFP, degree of polarization was 0.89

and, when liganded with epidermal growth factor (EGF) 0.74, indicating further oligomerization upon agonist treatment.

These workers [114] also examined EGFR lipid raft association with hetero-FRET. Previously they showed, using GM1 labeled with CtxB-Alexa 594 as acceptor and EGFR labeled with Alexa 488 as donor, FRET emission increased compared with the control indicating that EGFR is associated with lipid rafts [115].

Hofman and co-workers [114] showed that EGFR-mGFP is constitutively aggregated on NIH 3T3 cells. Although these authors' results are similar to the data presented here for cells transfected with hLHR, our data showed that high expression levels of hLHR present in transfected CHO cells induce various effects. Such effects include FRET efficiency of 23% for unliganded hLHR and 28% for liganded hLHR. We thus show that hCG promotes aggregating of hLHR, a result similarly to Hofman et al.'s EGFR-mGFP conclusion that EGFR oligomers increase when cells are treated with EGF. In contrast to the data presented in this dissertation, they state that there was no concentration-dependence of EGFR. They examined a stable cell line, thus the observation that EGFR is concentration-dependent is conceivable. We observed an increase in FRET efficiency when receptor density increased for hLHR. This may result from our use of transiently transfected cells. Such cells exhibit broad receptor range for hLHR expression. Since Hofman and co-workers used a stable cell line, it seems possible that the constitutively oligomerization they observe does not arise from molecular crowding, even with EGFR known to be associated with lipid rafts. However, the extent

of possible molecular crowding cannot be determined because EGFR number per cell was not reported. Hofman and co-workers' study of homo-FRET examination of self-association of EGFR nonetheless shows that homo-FRET is a valuable tool that in the study of membrane proteins self-association.

He and co-workers [116] evaluated the homotropic association of Dok 1 (downstream of tyrosine kinases) and Dok 5 proteins on COS 7 cells. Hetero-FRET measurements involving YFP acceptor photobleaching for co-expressed Dok 5-CFP and Dok5-YFP showed substantial FRET between these proteins. In addition, Dok1-CFP and Dok1-YFP showed significantly increased FRET compared to the control sample, namely, cells co-transfected with CFP and YFP not fused to Dok proteins. To determine whether certain domains in Dok5 and Dok1 proteins were needed for signaling, the pleckstrin homology (PH) domain, phosphotyrosine binding domain (PTB), and the carboxyl-terminus (COOH) in Dok 1 and Dok 5 were removed. Dok5-CFP co-expressed with Dok5ΔPH-YFP revealed no FRET, indicating the PH domain is needed for aggregation. In similar experiments involving Dok1, Dok1-CFP co-expressed with Dok1ΔPH-YFP and Dok1ΔPTB-YFP revealed no FRET. These hetero-FRET data showed that the PH and PTB domains were both needed for Dok1 aggregation.

In the above study He and co-workers [116] examined transiently transfected cells. Low FRET values ranging from 1-4% suggest Dok1 and Dok5 are present at low levels. Self-association was observed for Dok1 and Dok5 in addition to association with each other. However, protein number per cell was not reported so it cannot be determined

whether Dok numbers per cell might affect FRET values or extent of receptor aggregation. In our data, we show that FRET between hLHR is density dependent. As hLHR receptor density increased, FRET efficiencies increased as well. Since Dok1 and Dok5 show low FRET values, it is likely that FRET arises from specific association and not from molecular crowding. This drastically differs from our data where we show hLHR-eYFP strongly expressed in transiently transfected CHO cells experiences FRET simply as a consequence of molecular crowding.

Piston and co-workers [117] used steady-state homo-FRET to evaluate if GFP variously attached to MHC class I molecules exhibit different anisotropy values. MHC class I molecules are similar to the MHC class II molecules. Both are important in the generation of biological immune responses. A construct having GFP attached to the cytoplasmic tail of $H2L^d$ MHC class I was termed $H2L^d$GFPin and GFP more rigidly attached to the protein via the N-terminal amino acid sequence was termed $H2L^d$GFPout. These molecules were transiently transfected into COS 7 cells and fluorescence images were collected of COS 7 membrane blebs, bubble-like structures which sometimes protrude from cells and which contains no cytoskeleton components. Fluorescence polarization as a function of β, the angle from the horizontal when a horizontal excitation polarizer is used, was plotted and, MHC class I H2LdGFPin showed uniform fluorescence parallel and perpendicular directions, with respect to exciting light polarization, at different angles to the plasma membrane which is consistent with random orientation of GFP. MHC class I $H2L^d$GFPout showed fluorescence parallel intensities that varied significantly at different angles of β while fluorescence perpendicular

intensities remained consistent with respect to exciting light polarization. These data demonstrated that more rigidly-bound fluorophores would are more suitable for homo-FRET experiments than more flexibly-bound fluorescent moieties. Homo-FRET indicated that, for molecules in the ER, peptide treatment increased FRET for $H2L^dGFPout$ but not for $H2L^dGFPin$. Change in anisotropy values upon photobleaching was measured as percentage changes. The Authors observed changes in anisotropy values upon photobleaching for $H2L^dGFPout$ of 12% unliganded and 3% for murine cytomegalovirus (MCMV)-peptide loaded molecules. For $H2L^dGFPin$, a change in anisotropy upon photobleaching was less than 4% for both unliganded and MCMV-peptide loaded cells. However, they did not analyze the change in anisotropy upon photobleaching for blebs, which revealed, for both the $H2L^dGFPout$ and $H2L^dGFPin$, that mean anisotropies are the same within experimental error. Thus, the two different types of fluorophore attachments actually do not affect the FRET observed in plasma membrane measurements but obviously had an effect on FRET measured from MHC class I molecules in the ER.

In their study Piston et al. [117] may have observed constitutive oligomerization of MHC class I molecules in the membrane blebs but this cannot be firmly established, since they did not report data of the peptide interacting with the MHC class I molecule on blebs. They report mean anisotropy values for MHC class I molecules in the ER of 0.340±0.002 and 0.343±0.002 for unliganded and liganded $H2L^dGFPin$, respectively. Since there is not a significant change in mean anisotropy, there could be constitutive FRET between MHC class I molecules in the ER. We observe apparent constitutive

oligomerization in our data with homo-FRET efficiencies only differing by 5% from untreated to hCG-treated cells transfected with hLHR-eYFP and these data also support increased oligomerization upon hormone treatment. Piston and co-workers do see increased aggregation of H2L^{d}GFPout in the ER. Unfortunately, they do not report receptor numbers or possible raft association of MHC class I molecules. In addition, results would have higher physiological relevance if obtained from examination of the plasma membrane of intact cells live cells rather than cell blebs. This is because membranes on intact have a full complement of intracellular components associated with function of surface molecules like MHC class I.

Gerritsen and co-workers [118] used steady-state and time-resolved homo-FRET to study FK596-binding protein (FKBP-mGFP) fused to monomeric GFP on NIH 3T3 cells, a mouse embryonic fibroblast cell line. Homo-FRET data were taken for FKBP-mGFP and for 2xFKBP-mGFP, a construct containing two FKBP binding domains, with and without a ligand AP20187 (AP) known to induce FKBP aggregation. The steady-state results revealed that AP treatment increased the change in anisotropy upon photobleaching and decreased initial anisotropy. A greater change in anisotropy upon AP treatment and decrease in initial anisotropy was seen for 2xFKBP-mGFP. An increase in change of anisotropy upon agonist treatment along with decreased initial anisotropy values indicates receptor oligomerization.

In Gerritsen et al.'s work [118], time-resolved homo-FRET data showed effects of ligand binding similar to the steady-state data. However, one-photon excitation (OPE)

time-resolved measurements revealed an increased change in anisotropy upon photobleaching of approximately 25%. Two-photon excitation (TPE) time-resolved homo-FRET yielded similar results, but with a dynamic range 40-50% larger than the steady state data. Initial anisotropy values for time-resolved TPE were lower than OPE.

The studies performed by these workers [118] for both steady-state and time-resolved who changes in anisotropy upon photobleaching values are relatively small for unliganded FKBP-mGFP and 2xFKBP-mGFP compared to liganded receptors, suggesting that the protein exists mostly as monomers in untreated cells. Upon AP treatment, change in anisotropy upon photobleaching increases showing oligomerization for both steady-state and time-resolved homo-FRET. We observe this increase in our change in anisotropy upon photobleaching values as well. Change in anisotropy upon photobleaching for unliganded hLHR was 0.081±0.006 and, upon hCG treatment 0.099±0.010. These values are high for unliganded hLHR, suggesting that hLHR-eYFP transiently transfected into CHO cells are extensively aggregated before hormone treatment. Gerritsen et al. state their transfection preparations are not expected to induce cluster formation but do not report the reasons for these expectations or actual protein number per observed cell. As mentioned previously, we do observe a decrease in initial anisotropy as hLHR surface density increases. Although protein number per cell was not reported in Gerritsen et al.'s study, it seems likely that molecular crowding may not be present since steady-state initial anisotropy for unliganded FKBP-mGFP receptors were close to the anisotropy value of a single mGFP fluorophore. These authors' use of OPE

and TPE in both steady-state and time-resolved homo-FRET shows homo-FRET can be accessed in different ways to evaluate self-association of membrane proteins.

Sharma and Mayor [87] report steady-state and time-resolved homo-FRET between GFP fused to GPI-anchored proteins when expressed at local receptor concentrations of 100-2000/μm^2. Transient transfections with GFP GPI-anchored proteins on CHO cells were used for these homo-FRET studies. As we observed ourselves, their transiently transfected GPI-anchored proteins exhibited a range of cell surface densities. They suggest these densities are too low to show significant concentration-induced homo-FRET. However, calculations based on the model shown in this dissertation disagree. Sharma and Mayor report homo-FRET efficiencies between 20-40%. For receptors uniformly distributed on the plasma membrane, with a 4.65 nm Förster distance and present at 2000/μm^2, calculations using Equation 29 suggest the apparent FRET of approximately 14% (see Figure 39). Therefore, their FRET values seem likely to be attributable to protein concentrations above ~500 μm^{-2} and they observed apparent oligomerization for low local protein concentrations of ~100 μm^{-2}. Since Friedrichson and co-workers [119] previously report GPI-anchored proteins are associated with lipid rafts, expressed proteins would be concentrated in these raft compartments and so that high FRET values could arise from local concentration of GPI-anchored proteins into lipid rafts occupying only a small fraction of the cell surface.

Scarlata and co-workers [120] used steady-state polarization anisotropy to study FITC-conjugated melittin (F-melittin), a tetrameric toxin from bee venom. FITC is fused

to an each melittin monomer in the tetramer. Two samples were evaluated, namely a 1:24 mixture F-melittin to unconjugated melittin and pure F-melittin. Anisotropy upon photobleaching was plotted as a function of percent methanol, since methanol induces dissociation of tetrameric melittin. Methanol percentages ranged from 0 to 60%. As the methanol percentage increased, anisotropy upon photobleaching values decreased for the 1:24 mixture due to the melittin tetramer dissociating into monomers. Pure F-melittin anisotropy upon photobleaching values are significantly lower than those exhibited by the 1:24 mixture and such anisotropy upon photobleaching values increase with percent methanol until 30% methanol is reached. Above 30% methanol, anisotropy upon photobleaching values for pure F-melittin approach anisotropy values of the 1:24 mixture, suggesting the tetramer dissociates at methanol concentrations able 30%. These various results demonstrate the self-association of melittin.

The Authors used sodium chloride to induce melittin aggregation. F-melittin and 1:24 melittin mixture were examined at increasing sodium chloride concentrations ranging from 0-1.5 M. The anisotropy upon photobleaching for the 1:24 mixture increased from 0.084 to 0.148 with increasing sodium chloride concentration from 0 to 1.5 M. Since the 1:24 mixture does not exhibit homotransfer, this increase in anisotropy upon photobleaching results from ~15% bulk viscosity increase. Pure F-melittin initial anisotropy is slightly lower than that of the 1:24 mixture at 0 M NaCl. This is because conjugating FITC to melittin removes a positive charge, thus reducing unfavorable electrostatic interaction between melittin molecular. The NaCl reduces such repulsions between positive charges; therefore a reduction of a positive charge in F-melittin will

allow F-melittin to aggregate at lower ionic strength. To demonstrate homo-FRET aggregation in a plasma membrane, studies were done using large unilamellar vesicles (LUVs) which are made from 1-palmitoyl-oleoyl-*sn*-glycero-3-phosphorylcholine (POPC) lipids. Anisotropy upon photobleaching of POPC LUVs containing melittin was plotted versus lipid-melittin ratios for F-melittin, 1:10 and 1:15 F-melittin to melittin mixtures. These experiments demonstrated that pure F-melittin remained self-associated for POPC:peptide ratios ranging from 2500 to 0. However, both of the mixtures of F-melittin with unconjugated melittin did not aggregate over a 2000:1 POPC to peptide ratios. The 1:15 F-melittin to melittin mixture exhibited the highest anisotropy values because it is the least likely to contain fluorescent melittin moieties in close enough proximity to transfer energy. These studies show that melittin does self-associate in lipid bilayers but studies with live cells would give more information on melittin's mechanism of action; however melittin's toxicity precludes its use in cellular studies.

In their study, Scarlata et al. showed that the increase in anisotropy upon photobleaching for pure F-melittin as increasing methanol concentrations cause dissociation shows the size of melittin aggregates. In our work we observe higher initial anisotropy values at low receptor densities, as shown in Figures 28-30. This suggests that smaller oligomers have elevated anisotropy values since they have fewer LHR neighbors to which they can transfer energy. The high anisotropy upon photobleaching values exhibited in the 1:15 F-melittin to melittin mixture compared to the 1:10 mixture and pure F-melittin show that F-melittin to melittin ratios do affect self-association. We

observe this also in our results when FRET efficiency versus hLHR receptor density was plotted. As hLHR receptor density increased, FRET efficiency also increased.

Jovin and co-workers [121] used His-tagged venus fluorescence protein (VFP) expressed in *E. coli* cells to study steady-state homo-FRET. They observed that steady-state anisotropy increased as VFP concentration in *E. coli* cells decreased, which is also observed in the data presented here (Figure 24a). Figure 24a-b represents data for a CHO cell transiently transfected with hLHR-eYFP where average initial intensity and anisotropy upon photobleaching versus time was plotted. In this graph, as fluorophores are irreversibly bleached over time, anisotropy upon photobleaching increases because density of fluorophores decreases and, in the limit of complete photobleaching, the last individual fluorophore has no possibility of transferring its excitation energy to another molecule. Also, time-resolved homo-FRET, as described previously in this dissertation was used to image fluorescence anisotropy of epidermal growth factor (erbB1) receptor fused to eGFP and stably expressed in CHO and A431 cells [122]. A plot of anisotropy as a function of fractional fluorescence intensity remaining as photobleaching proceeds was created, showing that anisotropy increased as fractional intensity decreased for erbB1-eGFP on CHO cells. This supports the trend demonstrated for Figure 24b, where anisotropy upon photobleaching was plotted versus fractional intensity. In this graph, anisotropy upon photobleaching increases as fractional intensity decreases. A431 cells have endogenous erbB1 receptors as well erbB1-eGFP introduced by transfection. The combination of erbB1-eGFP and non-fluorescent erbB1 will result in low energy transfer because erbB1-eGFP may not be in proximity to another erbB1-eGFP. When time-

resolved anisotropy versus fractional fluorescence intensity was plotted for A431 cells, anisotropy upon photobleaching remained constant. Their data, in conjunction with the data presented in this dissertation, demonstrate that homo-FRET can be used to evaluate receptor interactions. When anisotropy is plotted as a function of fractional intensity, anisotropy increases and receptor interaction are being observed.

Conclusion and future directions

In summary, this study demonstrates that CHO cells transiently transfected with hLHR-eYFP exhibit spontaneous FRET on untreated cells, as well as on cells exposed to hCG and DG-hCG treatments. Substantial FRET efficiencies were observed for hCG and DG-hCG treated cells as well for untreated cells. Hormone treatment affects hLHR association. Upon hCG treatment, FRET efficiencies and change in anisotropy upon photobleaching increased compared to untreated cells, showing that hCG promotes oligomerization. For DG-hCG treated cells, FRET efficiencies and change in anisotropy upon photobleaching decreased, showing DG-hCG suppresses oligomerization. Secondly, hLHR expression levels affect self-association. FRET efficiencies increased as hLHR surface density increased for hCG and DG-hCG treated cells as well as for untreated cells suggesting substantial FRET arises simply from receptor proximity. Also, a decrease in anisotropy upon photobleaching values as hLHR surface density increased further supports this notion.

CHO cells transiently transfected with hLHR-eYFP have a broad distribution of receptor numbers per cell. In this distribution a substantial fraction of cells exhibit high receptor numbers compared to levels in cells naturally expressing LHR. We estimate that our measurements were typically performed on cells expressing ~118,000 receptors or more per cell. A substantial amount of apparent FRET may arise from molecular crowding, especially if the receptors are concentrated by location in lipid rafts, as has been demonstrated previously for hLHR. It seems possible that, in studies of transiently transfected cells, much of the observed FRET/BRET may arise from high densities of receptors on the surface, i.e. molecular crowding. Hence receptor number per cell should always be reported so that possible effects of molecular crowding can be assessed. However, this observation does not rule out the possibility that hLHR may also form dimers or low-order oligomers in the ER which are then trafficked to the plasma membrane. Either LHR monomers or such oligomers upon hCG treatment may then undergo further oligomerization as demonstrated by our data. Therefore, our results agree with previous data from Segaloff et al. [61] and Roess et al. [106] that hLHR aggregates to some extent upon hCG treatment.

Finally, homo-FRET can be used as a general tool to evaluate self-association of other biological systems, such as was shown here using MHC class II molecules. For normal, inactive and partially active MHC class II molecules, constitutive dimerization was observed for control cells and for cells subjected to MβCD, crosslinking and enhanced cAMP activity.

This study shows that, to accurately assess possible receptor aggregation in plasma membranes using biophysical techniques such as FRET and BRET, it is important to take specific factors into consideration. The first factor is protein number per cell, more particularly, the number of receptors per unit area of the cell surface. High protein surface concentrations can give rise to apparent FRET and BRET by reason of simple proximity, i.e. molecular crowding. This can be misinterpreted as arising from specific association. In particular, transiently transfected cells exhibit a wide range of receptor expression levels, and FRET and BRET measurements tend to focus on the most fluorescent, i.e. most highly expressing, cells in the population. It is important to measure, at least approximately, receptor number in cells studied for comparison with number of receptors occurring naturally receptors on cells of physiological interest. A second factor is lipid raft association. If proteins are in lipid rafts, local protein concentrations can be significantly increased. Thus molecular crowding may give rise to even higher extents of apparent association which are not relevant to receptors occurring naturally on cells.

Future experimentation should involve treating CHO cells expressing hLHR-eYFP with MβCD to disrupt lipid rafts by cholesterol depletion. This would reduce local receptor concentration, thereby lowering FRET if lipid rafts can contribute to effects induced by molecular crowding. Additionally, another useful experiment will be to examine Cyanine 5 (Cy5) labeled hLHR on cells expressing CFP-Epac-YFP probe, where Epac is an abbreviation for Exchange Protein directly Activated by CAMP. This experiment allows evaluation of the possibility of continuous cell activation and cAMP

signaling, simply as a consequence of high receptor densities. When cAMP is not bound to Epac, CFP and YFP are in proximity and CFP excitation causes energy transfer and fluorescence emission from YFP. After Epac binds cAMP, the Epac probe unfolds so that CFP and YFP are not in proximity and only CFP fluorescence emission will be observed. This experiment would be executed using flow cytometry to monitor CFP and YFP fluorescence intensities to assess cell activation while Cy5-hLHR intensities is monitored simultaneously to assess receptor surface density.

It is still unclear the extent to which LHRs expressed at endogenous levels maybe constitutively aggregated and how much ligand binding may cause them to further aggregate. Therefore, another useful experiment would be to obtain a stable cell line exhibiting physiologically-relevant receptor levels of 20,000 to 40,000 receptors per cell. These cells could be examined using homo-FRET before and after hCG and DG-hCG binding. In addition, fluorescent GM1, a marker for lipid rafts, could be used in hetero-FRET experiments to determine raft *in vivo* association of LHR with lipid rafts.

References

1. Stocco C, Telleria C, Gibori G: The molecular control of corpus luteum formation, function, and regression. *Endocr Rev* 2007, 28(1):117-149.
2. Dufau ML: The luteinizing hormone receptor. *Annual Review of Physiology* 1998, 60:461-496.
3. Knobil E, Neill J: Encyclopedia of Reproduction, vol. 2; 1998.
4. Jaffe R, Lee P, Midgley AJ: Serum gonadotropins before, at the inception of, and following human pregnancy. *J Clin Endocrinol Metab* 1969, 29:1281-1283.
5. Fredericks ZL, Pitcher JA, Lefkowitz RJ: Identification of the G-protein coupled receptor kinase phosphorylation sites in the human β_2-adrenergic receptor. *J Biol Chem* 1996, 271:13796-13803.
6. Lefkowitz R: Seven transmembrane receptors - A brief personal retrospective. *Biochimica et Biophysica Acta* 2007, 1768:748-755.
7. McFarland K, Sprengel R, Phillips H, Kohler M, Rosemblit N, Nikolics K, Segaloff D, Seeburg P: Lutropin-choriogonadotropin receptor: An unusual member of the G protein-coupled receptor family. *Science* 1989, 245:494-499.
8. Jia X-C, Oikawa M, Bo M, Tanaka T, Ny T, Boime I, Hsueh AJW: Expression of human luteinizing hormone (LH) receptor: Interaction with LH and chorionic gonadotropin from human but not equine, rat, and ovine species. *Mol Endo* 1991, 5:759-768.
9. Segaloff DL, Ascoli M: The lutropin/choriogonadotropin receptor...4 years later. *Endocr Rev* 1993, 14:324-347.

10. Sanchez-Yague J, Rodriquez MC, Segaloff DL, Ascoli M: Truncation of the cytoplasmic tail of the lutropin/choriogonadotropin receptor prevents agonist-induced uncoupling. *J Biol Chem* 1992, 267:7217-7220.

11. Ascoli M, Fanelli F, Segaloff D: The lutropin/choriogonadotropin receptor, a 2002 perspective. *Endocr Rev* 2002, 23(2):141-174.

12. Wu H, Lustbader JW, Liu Y, Canfield RE, Hendrickson WA: Structure of human chorionic-gonodotropin at 2.6-angtrom resolution from MAD analysis of the selenomethionyl protein. *Structure* 1994, 2(6):545-558.

13. Lapthorn AJ, Harris DC, Littlejohn A, Lustbader JW, Canfield RE, Machin KJ, Morgan FJ, Isaacs NW: Crystal structure of human chorionic gonadotropin. *Nature* 1994, 369(6480):455-461.

14. Lapthorn AJ, Harris DC, Littlejohn A, Lustbader JW, Canfield RE, Machin KJ, Morgan FJ, Isaacs NW: Crystal structure of human chorionic gonadotropin. *Nature* 1994, 369:455-461.

15. Manjunath P, Sairam M: Biochemical, biological, and immunological properties of chemically deglycosylated human choriogonadotropin. *J Biol Chem* 1982, 257(12):7109-7115.

16. Sairam M, Bhargavi G: A role for glycosylation of the α subunit in transduction of biological signal in glycoprotein hormones. *Science* 1985, 229:65-67.

17. Manjunath P, Sairam MR: Properties of chemically deglycoslated human chorionic-gonadotropin. *Federation Proceedings* 1981, 40(6):1854-1854.

18. Roess DA, Jewell MA, Philpott CJ, Barisas BG: The rotational diffusion of LH receptors differs when receptors are occupied by hCG versus LH and is increased by Cytochalasin D. *Biochimica et Biophysica Acta* 1997, 1357:98-106.

19. Hunzicker-Dunn M, Gurevich V, Casanova J, Mukherjee S: ARF6: a newly appreciated player in G protein-coupled receptor desensitization. *FEBS Letters* 2002, 521:3-8.

20. Wu SM, Leschek EW, Rennert OM, Chan WY: Luteinizing hormone receptor mutations in disorders of sexual development and cancer. *Pediatr Pathol Mol Med* 2000, 19(1):21-40.

21. Barron AM, Verdile G, Taddei K, Bates KA, Martins RN: Effect of Chronic hCG Administration on Alzheimer's-Related Cognition and A beta Accumulation in PS1KI Mice. *Endocrinology* 2010, 151(11):5380-5388.

22. Li YY, Hou TJ, Goddard WA: Computational Modeling of Structure-Function of G Protein-Coupled Receptors with Applications for Drug Design. *Curr Med Chem* 2010, 17(12):1167-1180.

23. Ganguly S, Clayton AHA, Chattopadhyay A: Organization of Higher-Order Oligomers of the Serotonini(1A) Receptor Explored Utilizing Homo-FRET in Live Cells. *Biophys J* 2011, 100(2):361-368.

24. Wise A, Gearing K, Rees S: Target validation of G-protein coupled receptors. *Drug Discov Today* 2002, 7(4):235-246.

25. Weiss L: Some Cell Interactions. *Cancer and Metastasis Reviews* 2000, 19(3):235-255.

26. Singer SJ, Nicolson GL: The fluid mosaic model of the structure of cell membranes. Cell membranes are viewed as two-dimensional solutions of oriented globular proteins and lipids. *Science* 1972, 175:720-731.

27. Kusumi A, Suzuki K: Toward understanding the dynamics of membrane-raft-based molecular interactions. *Biochimica et Biophysica Acta* 2005, 1746:234-251.

28. Kusumi A, Ike H, Nakada C, Murase K, Fujiwara T: Single-molecule tracking of membrane molecules: plasma membrane compartmentalization and dynamic assembly of raft-philic signaling molecules. *Seminars in Immunology* 2005, 17:3-21.

29. Lommerse PHM, Spaink HP, Schmidt T: In vivo plasma membrane organization: results of biophysical approaches. *Biochim Biophys Acta-Biomembr* 2004, 1664(2):119-131.

30. Frye LD, Edidin M: The rapid intermixing of cell surface antigens after formation of mouse-human heterokaryons. *J Cell Sci* 1970, 7:319-335.

31. Marrack P, Endres R, Shimonkevitz R, Zlotnik A, Dialynas D, Fitch F, Kappler J: The major histocompatibility complex-restricted antigen receptor on T cells. II. Role of the L3T4 product. *J Exp Med* 1983, 158:1077-1091.

32. Loor F: Lectin-induced lymphocyte agglutination. An active cellular process? *Exp Cell Res* 1973, 82:415-425.

33. Poo M-M, Cone RA: Lateral diffusion of rhodopsin in the photoreceptor membrane. *Nature* 1974, 247:438-441.

34. Peters R, Peters J, Tews KH, Bahr W: A microfluorimetric study of translational diffusion in erythrocyte membranes. *Biochimica et Biophysica Acta* 1974, 367:282-294.

35. Axelrod D, Koppel DE, Schlessinger J, Elson E, Webb WW: Mobility measurement by analysis of fluorescence photobleaching recovery kinetics. *Biophys J* 1976, 16:1055-1069.

36. Jacobson K, Wu E, Poste G: Measurement of the translational mobility of con-canavalin A in glycerol-saline solutions and on the cell surface by fluorescence recovery after photobleaching. *Biochimica et Biophysica Acta* 1976, 433:215-222.

37. Leuther MD, Peacock JS, Barisas BG: Photobleaching recovery studies of membrane events accompanying lymphocyte stimulation. *Biophys J* 1979, 25:168a.

38. Barisas BG: Criticality of beam alignment in fluorescence photobleaching recovery experiments. *Biophys J* 1980, 29(3):545-548.

39. Schwille P, Korlach J, Webb W: Fluorescence correlation spectroscopy with single-molecule sensitivity on cell and model membranes. *Cytometry* 1999, 36:176-182.

40. Levi V, Gratton E: Exploring dynamics in living cells by tracking single particles. *Cell Biochem Biophys* 2007, 48(1):1-15.

41. Feder TJ, BrustMascher I, Slattery JP, Baird B, Webb WW: Constrained diffusion or immobile fraction on cell surfaces: A new interpretation. *Biophys J* 1996, 70(6):2767-2773.

42. Saxton M: Single-particle tracking: the distribution of diffusion coefficients. *Biophys J* 1997, 72:1744-1753.

43. Gratton E, Jameson D, Hall R: Mutifrequency phase and modulation fluorometry. *Annu Rev Biophys Bioeng* 1984, 13:105-124.

44. Lidke DS, Wilson BS: Caught in the act: quantifying protein behaviour in living cells. *Trends Cell Biol* 2009, 19(11):566-574.

45. Toomre D, Bewersdorf J: A New Wave of Cellular Imaging. In: *Annu Rev Cell Dev Biol.* vol. 26. Palo Alto: Annual Reviews; 2010: 285-314.

46. Ralston GB: Effects of crowding in protein solutions *J Chem Educ* 1990, 67(10):857-860.

47. Minton AP: Influence of excluded volume upon macromolecular structure and associations in 'crowded' media. *Curr Opin Biotechnol* 1997, 8(1):65-69.

48. Kooijman S: Quantitative aspects of metabolic organization: a discussion of concepts. *Philos Trans R Soc Lond Ser B-Biol Sci* 2001, 356(1407):331-349.

49. Ellis RJ: Macromolecular crowding: obvious but underappreciated. *Trends BiochemSci* 2001, 26(10):597-604.

50. Ross PD, Minton AP: Analysis of non-ideal behavior in concentrated hemoglobin solutions. *J Mol Biol* 1977, 112(3):437-452.

51. Minton AP: Molecular crowding: Analysis of effects of high concentrations of inert cosolutes on biochemical equilibria and rates in terms of volume exclusion. In: *Energetics of Biological Macromolecules, Pt B.* vol. 295. San Diego: Academic Press Inc; 1998: 127-149.

52. Minton AP: Confinment as a determinant of macromolecular structure and reactivity. *Biophys J* 1992, 63(4):1090-1100.

53. Minton AP: Confinement as a determinant of macromolecular structure and reactivity .2. Effects of weakily attractive interactions between confined macrosolutes and confining structures. *Biophys J* 1995, 68(4):1311-1322.

54. Minton AP: The effect of volume occupancy upon the thermodynamic activity of proteins-Some biochemical consequences. *Mol Cell Biochem* 1983, 55(2):119-140.

55. Zimmerman SB: Macromolucar crowding effects on macromolecular interactions-Some implication for genome structure and function. *Biochimica et Biophysica Acta* 1993, 1216(2):175-185.

56. Saini SS, Klion AD, Holland SM, Hamilton RG, Bochner BS, MacGlashan DW: The relationship between serum IgE and surface levels of Fc epsilon R on human leukocytes in various diseases: Correlation of expression with Fc epsilon RI on basophils but not on monocytes or eosinophils. *J Allergy Clin Immunol* 2000, 106(3):514-520.

57. Hirakawa T, Galet C, Ascoli M: MA-10 cells transfected with the human lutropin/choriogonadotropin receptor (hLHR): A novel experimental paradigm to study the functional properties of the hLHR. *Endocrinology* 2002, 143(3):1026-1035.

58. Lei Y, G.M. Hagen, S.V.L. Smith, G. Barisas, and D.A. Roess: Constitutively-active human LH receptors are self-associated and located in rafts. *Molecular and Cellular Endocrinology* 2007, 260-262:65-72.

59. Smith SML, Lei Y, Liu JJ, Cahill ME, Hagen GM, Barisas BG, Roess DA: Luteinizing hormone receptors translocate to plasma membrane microdomains after binding of human chorionic gonadotropin. *Endocrinology* 2006, 147(4):1789-1795.

60. Horvat RD, Barisas BG, Roess DA: Luteinizing hormone receptors are self-associated in slowly diffusing complexes during receptor desensitization. *Mol Endo* 2001, 15(4):534-542.

61. Tao Y-X, Johnson N, Segaloff D: Constitutive and agonist-dependent self-association of the cell surface human lutropin receptor. *J Biol Chem* 2004, 279(7):5904-5914.

62. Niswender G, Schwall R, Fitz T, Farin C, Sawyer H: Regulation of luteal function in domestic ruminant: New concepts. *Recent Progress in Hormone Research* 1985, 41:101-151.

63. Roess DA, Rahman NA, Kenny N, Barisas BG: Lateral and rotational dynamics of LH receptors on rat luteal cells. *Biochimica et Biophysica Acta* 1992, 1137:309-316.

64. Philpot CJ, Rahman NA, Kenny N, Barisas BG, Roess DA: Rotational dynamics of luteinizing hormone receptors on bovine and ovine luteal cell plasma membranes. *Biol Reprod* 1995, 53(3):647-652.

65. Roess DA, Brady CJ, Barisas BG: Biological function of the LH receptor is associated with slow receptor rotational diffusion. *Biochimica et Biophysica Acta* 2000, 1464(2):242-250.

66. Roess DA, Horvat RD, Munnelly H, Barisas BG: Luteinizing hormone receptors are self-associated in the plasma membrane. *Endocrinology* 2000, 141(12):4518-4523.

67. Guan R, Feng X, Wu X, Zhang M, Zhang X, Hebert T, Segaloff D: Bioluminescence resonance energy transfer studies reveal constitutive dimerization of the human lutropin receptor and a lack of correlation between receptor activation and the propensity for dimerization. *J Biol Chem* 2009, 284(12):7483-7494.

68. Perrin F: Polarisation de la Lumiere de Fluorescence. Vie Moyenne des Molecules dan L'etat Excite. *J Phys* 1926, 12:390-401.

69. Förster VT: Zwischenmolekulare energiewanderung und fluoreszenz. *Annalen der Physik* 1948, 6:54-75.

70. Weber G: Polarization of the fluorescence of macromolecules. I. Theory and experimental method. *Biochem* 1951, 51:145-167.

71. Jameson DM, Mocz G: Fluorescence Polarization/Anisotropy Approaches to Study Protein-Ligand Interactions. In., vol. 305; 2005: 301-322.

72. Stryer L: Fluorescence energy transfer as a spectroscopic ruler. *Ann Rev Biochem* 1978, 47:819-846.

73. Bucher H, Drexhage KH, Fleck M, Kuhn H, Mobius D, Schafer FP, Sonderma.J, Sperling W, Tillmann P, Wiegand J: Controlled transfer of excitation energy through thin layers. *Molecular Crystals* 1967, 2(3):199-&.

74. Styer L, Haugland RP: Energy Transfer: A Spectroscopic Ruler. *Proceedings of the National Academy of Science USA* 1967, 58(2):719-726.

75. Spencer RD, Toledo FB, Williams BT, Yoss NL: Design, construtcion, and 2 applications for an automated flow-cell polarization flurometer with digital read out-enzyme-inhibitor (antitrypsin) assay and antigen-antibody (insulin-insulin antiserum) assay. *Clin Chem* 1973, 19(8):838-844.

76. Krishna M, Ingole B: Evolving trends in biosciences: multi-purpose proteins - GFP and GFP-like proteins. *Curr Sci* 2009, 97(7):1022-1032.

77. Pfleger KDG, Eidne KA: Illuminating insights into protein-protein interactions using bioluminescence resonance energy transfer (BRET). *Nat Methods* 2006, 3(3):165-174.

78. Jameson DM, Ross JA: Fluorescence Polarization/Anisotropy in Diagnostics and Imaging. *Chem Rev* 2010, 110(5):2685-2708.

79. Rao M, Mayor S: Use of Forster's resonance energy transfer microscopy to study lipid rafts. *Biochim Biophys Acta-Mol Cell Res* 2005, 1746(3):221-233.

80. Patel H, Murray F, Insel P: G-protein-coupled receptor-signaling components in membrane raft and caveolae microdomains. *Handbook of Experimental Pharmacology* 2008, 186:167-184.

81. Simons K, Toomore D: Lipid rafts and signal transduction. *Nature Reveiws, Molecular Cell Biology* 2000, 1:31-39.

82. Brown RE: Sphingolipid organization in biomembranes: what physical studies of model membranes reveal. *J Cell Sci* 1998, 111:1-9.

83. Brown DA: Structure and function of sphingolipid- and cholesterol- rich membrane rafts. *J Biol Chem* 2000, 275(23):17221-17224.

84. Lucero HA, Robbins PW: Lipid rafts-protein association and the regulation of protein activity. *Arch Biochem Biophys* 2004, 426(2):208-224.

85. Saslowsky D, Lawrence J, Ren X, Brown D, Henderson R, Edwardson J: Placental alkaline phosphatase is efficiently targeted to rafts in supported lipid bilayers. *J Biol Chem* 2002, 277(30):26966-26970.

86. Simons K, Ikonen E: Functional rafts in cell membranes. *Nature* 1997, 387:569-572.

87. Sharma P, Varma R, Sarasij RC, Ira, Gousset K, Krishnamoorthy G, Rao M, Mayor S: Nanoscale organization of multiple GPI-anchored proteins in living cell membranes. *Cell* 2004, 116(4):577-589.

88. Jin L, Millard AC, Wuskell JP, Dong XM, Wu DQ, Clark HA, Loew LM: Characterization and application of a new optical probe for membrane lipid domains. *Biophys J* 2006, 90(7):2563-2575.

89. Song JM, Hagen G, Smith SML, Roess DA, Pecht I, Barisas BG: Interactions of the mast cell function-associated antigen with the type I Fc epsilon receptor. *Mol Immunol* 2002, 38(16-18):1315-1321.

90. Wanant S, Quon MJ: Insulin receptor binding kinetics: Modeling and simulation studies. *J Theor Biol* 2000, 205(3):355-364.

91. Wolf PR, Ploegh HL: How MHC class II molecules acquire peptide cargo: Biosynthesis and trafficking through the endocytic pathway. *Annu Rev Cell Dev Biol* 1995, 11:267-306.

92. Munnelly HM, Brady CJ, Wade WF, Roess DA, Barisas BG: Lateral and rotational dynamics of I-A^k molecules expressing cytoplasmic truncations. *International Immunology* 2000, 12(9):1319-1328.

93. Cresswell P: Invariant chain structure and MHC class II function. *Cell* 1996, 84(4):505-507.

94. Brown AM, Wright KL, Ting JPY: Human major histocompatibility complex class-II-associated invariant chain gene promoter-Funtional analysis and in vivo protein-DNA interactions of constitutive and IFN-gamma induced expression *J Biol Chem* 1993, 268(35):26328-26333.

95. Brown JH, Jardetzky TS, Stern LJ, Gorga JC, Strominger JL, Wiley DC: Human class II MHC molecule HLA-DR1 X-ray structure determined from 3 crystal forms *Acta Crystallogr Sect D-Biol Crystallogr* 1995, 51:946-961.

96. Springer TA, Robb RJ, Terhorst C, Strominger JL: Subunit and disulfide structure of monomeric and dimeric forms of detergent soluble HLA antigens. *J Biol Chem* 1977, 252(13):4694-4700.

97. Hayball JD, Lake RA: The immune function of MHC class II molecules mutated in the putative superdimer interface. *Mol Cell Biochem* 2005, 273(1-2):1-9.

98. Nydam T, Wade TK, Yadati S, Gabriel JL, Barisas BG, Wade WF: Mutations in MHC class II dimer of dimers contact residues: effects on antigen presentation. *International Immunology* 1998, 10(8):1237-1249.

99. Barisas BG, Wade WF, Jovin TM, Arndt-Jovin D, Roess DA: Dynamics of molecules involved in antigen presentation: effects of fixation. *Mol Immunol* 1999, 36(11-12):701-708.

100. Lehninger AL: Lehninger principles of biochemistry. New York: W.H. Freeman; 2005.

101. Berger AC, Roche PA: MHC class II transport at a glance. *J Cell Sci* 2009, 122(1):1-4.

102. Fallahi-Sichani M, Linderman JJ: Lipid Raft-Mediated Regulation of G-Protein Coupled Receptor Signaling by Ligands which Influence Receptor Dimerization: A Computational Study. *PLoS One* 2009, 4(8).

103. Pike LJ: The challenge of lipid rafts. *J Lipid Res* 2009, 50:S323-S328.

104. Patterson GH, Piston DW, Barisas BG: Förster distances between green fluorescent protein pairs. *Analytical Biochemistry* 2000, 284:438-440.

105. Vogel SS, Thaler C, Koushik S: Fanciful FRET. *Science's STKE* 2006, 2006(331):re2.

106. Smith S, Lei Y, Liu J, Cahill M, Hagen G, Barisas B, Roess D: Luteinizing hormone receptors translocate to plasma membrane microdomains after binding of human chorionic gonadotropin. *Endocrinology* 2006, 147(4):1789-1795.

107. Gaus K, Gratton E, Kable EPW, Jones AS, Gelissen I, Kritharides L, Jessup W: Visualizing lipid structure and raft domains in living cells with two-photon microscopy. *Proc Natl Acad Sci U S A* 2003, 100(26):15554-15559.

108. Roess DA, Smith SML: Self-Association and Raft Localization of Functional Luteinizing Hormone Receptors. *Biol Reprod* 2003, 69(6):1765-1770.

109. Bader AN, Hoetzl S, Hofman EG, Voortman J, Henegouwen P, van Meer G, Gerritsen HC: Homo-FRET Imaging as a Tool to Quantify Protein and Lipid Clustering. *ChemPhysChem* 2011, 12(3):475-483.

110. Roess DA, Rahman NA, Kenny N, Barisas BG: Molecular dynamics of luteinizing hormone receptors on rat luteal cells. *Biochimica et Biophysica Acta* 1992, 1137:309-316.

111. Philpot C, Rahman N, Kenny N, Barisas B, Roess D: Rotational dynamics of luteinizing hormone receptors on bovine and ovine luteal cell plasma membranes. *Biol Reprod* 1995, 53(3):647-652.

112. Horvat RD, Nelson S, Clay CM, Barisas BG, Roess DA: Intrinsically fluorescent luteinizing hormone receptor demonstrates hormone-driven aggregation. *Biochem Biophys Res Commun* 1999, 256:382-385.

113. Roess DA, Smith SML: Self-association and raft localization of functional Luteinizing Hormone receptors. *Biol Reprod* 2003, 69(6):1765-1770.

114. Hofman EG, Bader AN, Voortman J, van den Heuvel D, Sigismund S, verkleij AJ, Gerritsen HC, Henegouwen vBe: Ligand-induced EGF receptor oligomerizatin is kinase-dependent and enhances internalization. *J Biol Chem* 2010, 285(50):39481-39489.

115. Hofman EG, Ruonala MO, Bader AN, van den Heuvel D, Voortman J, Roovers RC, Verkleij AJ, Gerritsen HC, Henegouwen P: EGF induces coalescence of different lipid rafts. *J Cell Sci* 2008, 121(15):2519-2528.

116. Zhang F, Fu G, Wang C, Cao L, Yang H, Wang G, Chen Y, He C: Dectect of Homo- or Hetero-association of Doks by fluorescence resoncance enegy transfer in living cells. *Molecular Imaging and Biology* 2009, 11:188-194.

117. Rocheleau JV, M. Edidin, and D. W. Piston: Intrasequence GFP in Class I MHC Molecules, a Rigid Probe for Fluorescence Anisotropy Measurements of the Membrane Environment. *Biophys J* 2003, 84(6):4078-4086.

118. Bader AN, Hofman EG, Voortman J, Henegouwen P, Gerritsen HC: Homo-FRET Imaging Enables Quantification of Protein Cluster Sizes with Subcellular Resolution. *Biophys J* 2009, 97(9):2613-2622.

119. Friedrichson T, Kurzchalia TV: Microdomains of GPI-anchored proteins in living cells revealed by crosslinking. *Nature* 1998, 394(6695):802-805.

120. Runnels LW, Scarlata SF: Theory and application of fluorescence homotransfer to melittin oligomerization. *Biophys J* 1995, 69(4):1569-1583.

121. Lidke D, Nagy P, Barisas B, Heintzmann R, Post J, Kidke K, Clayton A, Arndt-Jovin D, Jovin T: Imaging molecular interactions in cells by dynamic and static fluorescence anisotropy (rFLIM and emFRET). *Biochemical Society Transactions* 2003, 31:1020-1027.

122. Lidke DS, Nagy P, Barisas BG, Heintzmann R, Post JN, Lidke KA, Clayton AHA, Arndt-Jovin DJ, Jovin TM: Imaging molecular interactions in cells by dynamic and static fluorescence anisotropy (rFLIM and emFRET). *Biochemical Society Transactions* 2003, 31:1020-1027.

LIST OF ABBREVIATIONS

5-HT_{1A}:	Serotonin 1_A receptor
AC:	adenyl cyclase
AP:	AP20187 ligand
APD:	Avalanche photodiode
ARF6:	ADP-ribosylation factor, isotype 6
ARNO:	ADP-ribosylation factor nucleotide-binding site opener
Asn:	asparagine
ATP:	adenosine triphosphate
ADP:	adenosine diphosphate
Au:	arbitrary units
B:	BRET signal
B_{50}:	half max BRET signal
BRET:	bioluminescence resonance energy transfer
BSA:	bovine serum albumin
cAMP:	cyclic adenosine monophosphate
CD:	cytochalasin D
CFP:	cyan fluorescent protein
CHO:	chinese hamster ovary
CL:	corpus luteum
COOH:	carboxylic terminal
CtxB:	cholera toxin subunit B

Cy5: indodicarbo-cyanine

Cys: cysteine

D: diffusion coefficient

Da: dalton

Dansyl: 1-dimethylanimonaphthalene-5-sulfonyl chloride

Db-cAMP: dibutyl-cyclic adenosine monophosphate

DG-hCG: deglycosylated-human chorionic gonadotropin

DiI: 1,1'-Diotadecyl-3,3,'3' – tetramethylindocarbocyanine iodide

DMEM: dulbecco's modified minimum essential medium

Dok: downstream of tyrosine kinases

DRM: detergent-resistant membrane

DsRed: ref fluorophore coral protein

E. coli: *Escherichia coli*

E: percent energy transfer efficiency

eBFP: enhanced blue fluorescent protein

eCFP: enhanced cyan fluorescent protein

EDTA: ethylenediaminetetraacetic acid

EGF: epidermal growth factor

eGFP: enhanced green fluorescent protein

EGFR: epidermal growth factor receptor

E_h: homo-FRET percent energy transfer

emFRET: energy migration fluorescence resonance energy transfer

Epac: exchange protein activated by cAMP

ER:	endoplasmic reticulum
erbB1:	an epidermal growth factor receptor
eYFP:	enhanced yellow fluorescent protein
F:	fluorescence signal
FBS:	fetal bovine serum
FCS:	fluorescence correlation spectroscopy
FCεRI:	Type I FCε receptor
FITC:	fluorescein isothiocyanate
FKBP:	FK596-binding protein
FLAG:	epitope tag
FLIM:	fluorescence lifetime imaging microscopy
F-melittin:	fluorescein isothiocyanate conjugated to melittin
FMPP:	familial male-limited precocious puberty
FPR:	fluorescence photobleaching recovery
FRAP:	fluorescence recovery after photobleaching
FRET:	Förster resonance energy transfer
F-SConA:	fluorescein- succinyl concanavalin A
G(τ):	time autocorrelation function of a signal
G:	g-factor
GDP:	guanosine diphosphate
GFP:	green fluorescent protein
Gly:	glycine
GM1:	membrane ganglioside

GPCR:	G protein-coupled receptor
GPI:	glycosylphosphatidylinositol
Gs:	stimulatory G protein
GTP:	guanosine triphosphate
hCG:	human chorionic gonadotropin
HEK:	human embryonic kidney
HEL:	hen egg lysozyme
hetero-FRET:	heterotransfer fluorescence resonance energy transfer
hLHR:	human luteinizing hormone receptor
homo-FRET:	homotransfer fluorescence resonance energy transfer
IgG:	immunoglobulin
Ii:	invariant chain
J:	spectral overlap
LH:	luteinizing hormone
LHR:	luteinizing hormone receptor
LUV:	large unilamellar vesicle
M:	mean square displacement
mAb:	monoclonal antibody
MCMV:	murine cytomegalovirus
MESF:	molecules of equivalent soluble fluorophores
mGFP:	monomeric green fluorescent protein
MHC:	Major Histocompatibility Complex
MIIC:	MHC class II containing compartments

MSD: mean square displacement

MβCD: methyl-beta cyclodextrin

OPE: one photon excitation

PALM: photoactivated localization microscopy

PBS: phosphate buffered saline

P_{FRET}: probability of Förster resonance energy transfer

PH: pleckstrin homology

p-MPPI: 4-(2´-methoxy)-phenyl-1-[2´-(N-2´´-pyridinyl)-*p*-iodobenzamido]ethyl-piperzine

PMT: photomultiplier tube

P_{no} (r): probability of no Förster resonance energy transfer

POPC: 1-palmitoyl-oleyol-*sn*-glycero-3-phosphorylcholine

PTB: phosphotyrosine binding domain

r: anisotropy

r_0: Förster distance

RET: resonance energy transfer

rLHR: rat luteinizing hormone receptor

RNA: ribonucleic acid

S ConA: succinyl concanavalin A

Ser: serine

Ser: serine

SPT: single particle tracking

STED: stimulated emission depletion microscopy

STORM: stochastic optical reconstruction microscopy

Thr:	threonine
TM:	transmembrane
TMR:	tetramethyl rhodamine
TPA:	time-resolved phosphorescence anisotropy
TPE:	tow photon excitation
TRITC:	tetramethylrhodamine isothiocyanate
Tyr:	tyrosine
VFP:	visible fluorescent protein or venus fluorescent protein
Wt:	wild type
YFP:	yellow fluorescent protein
β2-AR:	beta 2 adrenergic receptor
κ:	orientation factor between two transition dipoles

APPENDIX I

PREFACE

This section includes other work I have done at Colorado State University while working towards my degree of Doctor of Philosophy.

In fall, 2006, I was diagnosed with an uncommon phyllodes tumor in my left breast and on March 19th 2007 underwent a simple mastectomy with breast reconstruction. This appendix a case report of my surgery with a brief review of phyllodes tumors, which I wrote and recently published. I was the originating author of initial and revised manuscript versions and corresponding author for the publication.

Crenshaw SA, Roller MD, Chapman JK: *World Journal of Surgical Oncology* 2011, 9:34-38.

Shirley A. Crenshaw
Department of Chemistry
Colorado State University
Fort Collins, CO 80523
Spring, 2012

IMMEDIATE BREAST RECONSTRUCTION WITH SALINE IMPLANT AND ALLODERM, FOLLING REVMOVAL OF A PHYLLODES TUMOR

Background

Phyllodes tumors are uncommon tumors of the breast that exhibit aggressive growth. While surgical management of the tumor has been reported, a single surgical approach with immediate breast reconstruction using AlloDerm has not been reported.

Case presentation

A 22-year-old woman presented with a 4 cm mass in the left breast upon initial examination. Although the initial needle biopsy report indicated a fibroadenoma, the final pathologic report revealed a 6.5 cm x 6.4 cm x 6.4 cm benign phyllodes tumor *ex vivo*. Treatment was a simple nipple-sparing mastectomy coupled with immediate breast reconstruction. After the mastectomy, a subpectoral pocket was created for a saline implant and AlloDerm was stitched to the pectoralis and serratus muscle in the lower-pole of the breast.

Conclusions

Saline implant with AlloDerm can be used for immediate breast reconstruction post-mastectomy for treatment of a phyllodes tumor.

Background

Cystosarcoma phyllodes was first described in 1838 by Johannes Müller but was not found to be malignant until 1943 by Cooper and Ackerman [1]. It is now commonly called phyllodes tumor. It is less than 1% of breast tumors and exhibits unpredictable behaviour.

Reports in literature have been focused on surgical approaches to the tumor removal. Although patient assessment prior to tumor removal often includes plans for immediate breast reconstruction, these approaches are rarely reported unless the tumor is classified as giant or is in an adolescent female [2-5]. Usual tumor treatment is wide local excision and simple mastectomy [6-8]. However, there have been few reports on breast reconstruction with phyllodes tumors, especially within the last 10 years. Because of the fast growth rate of these tumors, a greater than a 1 cm negative margin is preferred with tumor removal and a mastectomy may have to be performed to prevent local reoccurrence. Breast reconstruction usually consists of a transverse rectus abdominis musculocutaneous (TRAM) flap or a latissimus dorsi (LD) musculocutaneous flap as in other breast cancers.

Here we report a single surgery that includes reconstruction of the breast immediately post-mastectomy using a saline implant and AlloDerm. AlloDerm is becoming increasingly popular for immediate breast reconstruction. It is a viable option for athletic or thin women for whom TRAM or LD is not possible. A submuscular pocket

can be created for a breast implant and AlloDerm is used to give lower-pole fullness. It helps fill the breast flap when subcutaneous tissue is limited and supports the breast implant which can have issues such as rippling or bottoming out [9, 10].

Case presentation

The patient was a 22-year-old African American female who presented with a left breast mass. The mass had been present for at least 3 months. The left breast was larger and leaked a clear fluid. Upon initial examination, the patient's primary care provider observed a 4 cm mass. The patient also experienced pain down the left arm which was reported about a week after the initial exam. Her aunt on her father's side had been treated for breast cancer at 39. She had no past medical or surgical history, did not use tobacco, and menarche occurred at 11 years of age.

Ultrasound of the left breast (Figure 43) revealed a 9 cm x 9 cm x 4.5 cm hypoechoic mass centered at the 12-1 o'clock area. The anterior of the mass appeared to be within 1 cm of the skin and the posterior was on the pectoral muscle. The echotexture varied from hypoechoic to isoechoic and there are small cystic areas within the mass. There were no other masses identified in the left breast or the left axilla. The mass was deemed suspicious for malignancy and the assessment was Bi-RADS 4b. The patient was sent for surgical consultation.

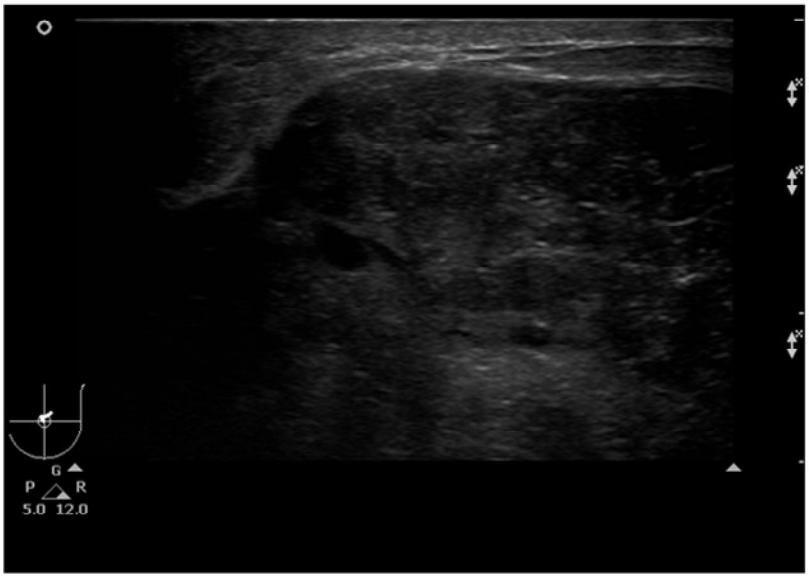

Figure 43: Ultrasound of benign phyllodes tumor in left breast.

Upon surgical consultation a core needle biopsy was performed with a 22-gauge needle; four biopsies were obtained. The biopsies were consistent with a fibroadenoma, indicating a benign tumor, which was consistent with the presentation of most cystosarcomas in core needle biopsies [11, 12].

The patient underwent a simple mastectomy with immediate breast reconstruction. Because the tumor volume was approximately two thirds of the breast and lumpectomy would result in poor cosmetic outcome, simple mastectomy with nipple-areola complex (NAC) preservation was performed on the patient. Standard breast reconstruction usually consists of a transverse rectus abdominis musculocutaneous flap or a latissimus dorsi musculocutaneous flap. However, the patient did not have adequate fatty tissue at the abdomen for the TRAM procedure and the patient did not want the large scar across the abdomen that would result. The plastic surgeon thought LD was the better choice because it would provide a "living" breast but this still required a small implant. The patient opted for a saline implant with AlloDerm to the mastectomy site and a mastopexy (breast lift) or mastopexy and implant to the other breast for symmetry. Because breast reconstruction was coupled with mastectomy using AlloDerm, there was no need for a TRAM or LD surgery which reduced scarring and the patient's overall recovery time.

The simple mastectomy consisted of an incision along the mammary crease. Dissection of the breast was carried out by cutting down the anterior pectoral fascia and dissecting to approximately 1 cm from the clavicle. Medial dissection was carried out to

the left lateral border of the sternum and lateral dissection was carried over to the anterior border of the latissimus dorsi muscle. A bovie electrocautery was used to create a superior flap of the entire left breast.

Next, breast reconstruction was performed. At the level of the inframammary fold, the pectoralis muscle was divided from 4 to 8 o'clock and a subpectoral/subserratus pocket was made using an electrocautery. At the mastectomy site, the superior pole of the breast flap was thicker than the inferior pole. Therefore, the superior breast tissue was laterally divided and sutured under the skin and to the pectoralis muscle with 3-0 Monocryl. This smoothed out the contour of the superior pole. AlloDerm, used to give more lateral fill, was sutured to the inframammary fold and to the part of the pectoralis muscle with 3-0 polydioxanone. The saline implant was then inserted into the pocket. The flap was advanced down, sutured into place, and the implant was filled. A drain was inserted and the incision was closed with Monocryl and Dermabond. For symmetry, the other breast underwent vertical mastopexy and positioned by making the superior border of the areola at the same level as the other breast.

Grossly, the excised encapsulated mass measured 6.5 cm x 6.4 cm x 6.4 cm. The surface was tan with a whorled appearance. Pathologic findings were consistent with a benign phyllodes tumor displaying large leaf-like projections surrounded by uniform stroma (Figure 44a and 44b) and black-inked margins of resection were negative (Figure 45).

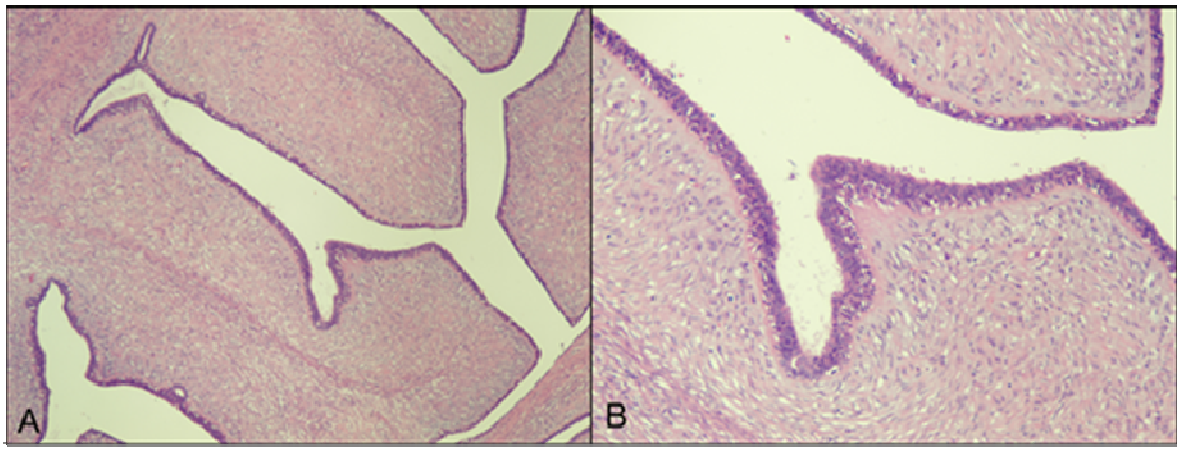

Figure 44 a. Image of leaf-like cystic ducts projected into the stroma. b. Image of one cystic duct.

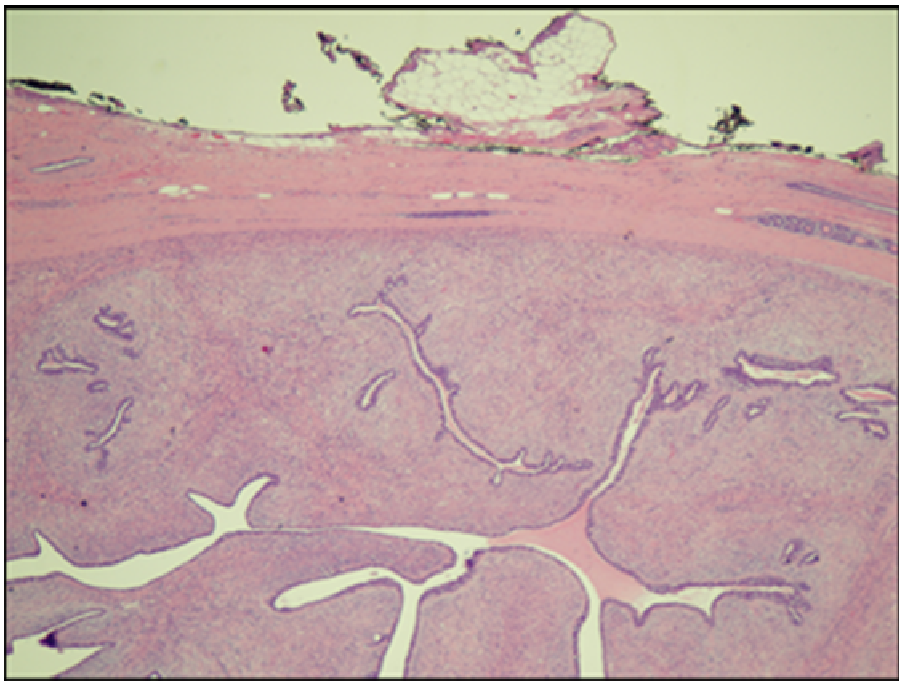

Figure 45: Negative margin of resection for the benign phyllodes tumor.

There were no postoperative complications and hospital stay was 24 hrs. The patient is currently 41 months post-surgery and has not had local reoccurrence. The patient is very pleased with the cosmetic outcome (Figure 46) and feels that immediate reconstruction was helpful in reducing emotional distress from the diagnosis and surgery.

Discussion

Phyllodes tumor is a disease of the epithelial and stroma tissue in the breast. It is classified as benign, borderline, and malignant. Malignant tumors have high stroma cellularity and tend to be permeative whereas benign tumors have low stroma cellularity and are circumscribed [6, 7, 13, 14]. Borderline tumors cannot be distinguished between the two because of the uncertainty of their behavior. These tumors can be encapsulated and their size typically ranges from 1-45 cm [6]. These tumors, when discovered, are usually large from their aggressive growth rate and at beginning stages, cause virtually no pain or other symptoms [15]. Larger tumors can result in nipple discharge, deformity of the skin, pain from the tumor weight, or pain from the impact on nerves [8, 15]. There is no correlation between size and tumor malignancy [7, 16].

Treatment for the disease usually involves wide local excision with negative margins greater than 1 cm [6-8]. If there is poor tumor to breast size, simple mastectomy is recommended. There have been a few cases reported of benign tumors metastizing but this is very rare [7]. These tumors tend not to metastasize to the axillary lymph nodes but more commonly to bone, lungs, and liver [6-8]. Adjuvant radiotherapy and chemotherapy

Figure 46: (a) Preoperative view of phyllodes tumor in left breast. (b) Postoperative view after 4 years with nipple-sparing mastectomy.*

*(Not shown to protect patient's privacy. See publication in *World Journal of Surgical Oncology*.)

generally are not used because the benefit of these therapies is unclear [6, 7, 17]. However, if the margins are less than 1 cm and there is chest wall invasion, adjuvant radiotherapy should be strongly considered [6].

As discussed in this report, breast reconstruction can be performed immediately after tumor removal. Although immediate breast reconstruction is oncologically safe to perform after mastectomy [9], Mortenson and co-workers found wound healing complications increased from 8.3% to 22.2% [18]. In three breast reconstruction groups, the tissue expander/implant, TRAM, and LD group, the site complications were 11.5%, 33%, and 83% within their own group, respectively.

In breast reconstruction, the NAC is preserved, if possible, for the best cosmetic outcome. It is still controversial to preserve the NAC when the tumor is cancerous and centrally located because it is unclear if the NAC is involved with breast cancer [19] .If removed, the NAC can be reconstructed. Common techniques to reconstruct the NAC are skin graft and tattoo but it is difficult to obtain nipple symmetry and reconstructed nipples often have poor nipple projection, color match, shape, and texture [19].

There are four main incisions for nipple-sparing mastectomy. The superior or inferior periareolar with lateral extension, transareolar with perinipple and lateral-medial extension, transareolar and transnipple incision with medial and lateral extension, and mammary crease that is inferior or lateral. The superior or inferior periareolar with lateral

extension allows good exposure for tumor removal but may compromise blood supply to the periphery of the flap and areola [19, 20]. The transareolar with perinipple and lateral-medial extension also provides good exposure and reduces the risk of ischemia to the lower portion of the areola. However, care must be taken not to divide the perinipple artery from the breast parenchyma causing perinipple scaring resulting in downward nipple projection [19, 20]. The transareolar and transnipple incision with medial and lateral extension provides good exposure to the lactiferous ducts for dissection and good vascularity to the areola and nipple, but the apical portion of the nipple may still suffer from ischemia or necrosis [20]. The mammary crease approach, inferior, was used here. The scar is the least visible and the skin flap vascularization is supported by superior and medial vessels [19, 20]. Vascularization of the nipple and areolar are not disturbed with this incision [20]. This incision is best for smaller breast with low ptosis as it may be difficult to reach parasternal and subclavicular areas of the breast for tumor removal. All incisions have equal risk of necrosis but women under 45 years of age had a higher rate of NAC viability [21].

Since immediate breast reconstruction is being used with increasing frequency, more surgical approaches are needed for fast recovery. AlloDerm is an acelluar dermal matrix from human cadaver skin. The skin has no cellular components and, for this reason, rejection is not an issue [9]. The use of AlloDerm in breast reconstruction has many advantages. It can be used off the shelf which reduces operation time [9]. If there is not enough subcutaneous tissue to fill a skin flap, AlloDerm can be used to fill out the inferior pole of the breast. AlloDerm also helps visually to reduce rippling, stark

contours, and bottoming out seen with larger implants [9, 10]. It also shortens recovery time. Hospital stay for AlloDerm/implant breast reconstruction was found to be an average of 48 hours [22]. It is safe to use and provides another option for immediate breast reconstruction.

Conclusions

Management of phyllodes tumors has many challenges which need to be addressed on a case by case basis. In this case, a simple mastectomy was the best option for a young patient with a comparatively large tumor mass. Although LD with an implant was thought to be the best choice for breast reconstruction, the patient opted for just a saline implant with AlloDerm and mastopexy for symmetry. The cosmetic outcome was good. Therefore implant reconstruction with AlloDerm should also be considered along with LD and TRAM if the patient wants minimal scarring and reduced recovery time.

Consent

Written informed consent was obtained from the patient for publication of this case report and accompanying images. A copy of the written consent is available for review by the Editor-in-Chief of this journal.

Competing interests

The authors declare they have no competing interests.

Authors' contributions

SAC prepared the manuscript.

MDR provided patient medical records and carried out the mastectomy.

JKC carried out the breast reconstruction.

All authors read and approved the final manuscript.

Author's information

SAC is a Ph.D. candidate in the Department of Chemistry at Colorado State University (CSU).

Acknowledgements

We thank WINS at CSU for donating funds for this publication, Dr. Chirstopher Staszak, M.D. for pathologic diagnosis, Dr. Tracy Florant, M.D. for radiology assessment, and Dr. Deborah Roess for discussions and suggestions for this report.

References

1. Cole-Beuglet C SR, Kurtz AB, Meyer JF, Kopans DB, Godlberg BB: Ultrasound, x-ray mammography, and histopathology of cystosarcomas phyllodes. *Radiology* 1983, 146:481-486.
2. Singh G SR: Immediate breast reconstruction for phyllodes tumors. *The Breast* 2008, 17:296-301.
3. Orenstein A TH: Cystosarcoma phylloides treated by excision and immediate reconstruction with silicon implant. *Ann Plast Surg* 1987, 18:520-523.
4. Mendel MA MD DRM, Vogt C MD, Reagan JW MD: Cystoscarcoma phyllodes: treatment by subcutaneous mastectomy with immediate prosthetic implantation. *Am J Surg* 1972, 23:718-721.
5. Lai Y-L WC-J, Noordhoof MS: Breast reconstruction following excision of phylloides tumor. *Ann Plast Surg* 1999, 43:132-136.
6. Fajdić J GN, Hrgović Z, Kristek J, Horvat V, Kaufmann M: Phyllodes tumors of the breast-diagnostic and therapeutic dilemmas. *Onkologie* 2007, 30:113-118.
7. Chaney AW PA, McNeese MD, Zagers GK, *et al*: Primary treatment of cystosarcomas phyllodes of the breast. *Cancer* 2000, 89:1502-1511.
8. Liang MI RR, Patterson CC, McKelvey MT, Gordillo G, Nuovo GJ, Carson WE: Giant breast tumors: Surgical management of phyllodes tumors, potential for reconstructive surgery and a review of literature. *World j Surg Onc* 2008, 6:117-124.
9. Breuing KH WS: Immediate bilateral breast reconstruction with implants and inferolateral AlloDerm slings. *Ann Plast Surg* 2005, 55:232-239.

10. Haddock N LJ: Breast reconstruction with implants, tissue expanders and AlloDerm: Predicting volume and maximizing the skin envelope in skin sparing mastectomies. *The Breast Journal* 2010, 16(1):14-19.

11. Veneti S MS: Bengin phyllodes tumor vs fibroadenoma: FNA cytological differentiation. *Cytopathology* 2001, 12:321-328.

12. El Hag IA MD PhD AAM, Kollur SM MD, Attallah A MD, Mohamed AAE MD, Al-Hussaini H MD: Cytological clues in distinction between phyllodes tumor and fibroadenoma. . *Cancer Cytopathol* 2010, 118:33-40.

13. Taira N TD, Aogi K, Ohsumi S, Takashima S, Nishimura R, Teramoto N: Phyllodes tumor of the breast: Stromal overgrowth and histological classification are useful prognosis-predictive factors for local recurrence in patients with a positive surgical margin. *Jpn J Clin Onocl* 2007, 37:730-736.

14. Tan PH MD JT, Chuah KL, Lee HY, Tan Y, Hilmy M, et al: Phyllodes tumors of the breast: the role of pathologic parameters. *Am J Clin Pathol* 2005, 123:529-540.

15. Treves N SD: Cystosarcoma phyllodes of the breast: A malignant and a benign tumor. *Cancer* 1951, 4:1286-1332.

16. Salvadori B CF, Del Bo R, Delledonne V, Grassi M, Rovini D, *et al*: Surgical treatment of phyllodes tumors of the breast. *Cancer* 1989, 63:2532-2536.

17. Mangi AA SB, Gadd MS, Tanabe KK, Ott MJ, Souba WW: Surgical management of phyllodes tumors. *Arch Surg* 1999, 134:487-493.

18. Mortenson MM SP, Khatri VP, Stevenson TR, Whetzel TP, Sommerhaug EJ, Goodnight JE, Bold RJ: Immediate breast reconstruction after mastectomy

increases wound complications. However, initiation of adjuvant chemotherapy is not delayed. *Arch Surg* 2004, 139:988-991.

19. Chung AP SV: Nipple-sparing mastectomy: Where are we now? *Sugical Oncology* 2008, 17:261-266.

20. Sacchini V PJ, Barros A, Luini A, Pluchinotta A, et al: Nipple-sparing mastectomy for breast cancer and risk reduction: Oncologic or technical problem? *J Am Coll Surg* 2006, 203:704-714.

21. Komorowski AL ZV, Regolo L, Carolei A, Wysocki WM, Costa A: Necrotic complications after nipple- and areola-sparing mastectomy. *World J Surg* 2006, 30:1410-1413.

22. Salzberg CA: Nonexpansive immediate breast reconstruction using human acellular tissue matrix graft (AlloDerm). *Ann Plast Surg* 2006, 57(1):1-5.